Timed Track Seeding for the Future Circular Collider

Dissertation

zur Erlangung des akademischen Grades

Doctor of Philosophy

eingereicht an der

Fakultät für Mathematik, Informatik und Physik der Universität Innsbruck

universität innsbruck

von

MSc. Valentin Völkl

valentin.volkl@cern.ch

Betreuer der Doktorarbeit:

Ao. Univ.-Prof. Mag. Dr. Emmerich Kneringer
(Institut für Astro- und Teilchenphysik)

Adj. Assoc. Prof. Dr. Benedikt Hegner
(CERN / Stony Brook University)

Innsbruck, 24. Dezember 2020

« العلم قفل و مفتاحه المسألة. »

Knowledge is a lock; and questions are its key.

Arabic saying.

Abstract

Particle accelerators and detectors have been the principal tools to investigate nature at the smallest scale for more than 50 years. The Large Hadron Collider (LHC) at the European Organization for Nuclear Research (CERN) in Geneva is scheduled to end its operation after the high-luminosity upgrade program HL-LHC concludes around 2040. An effort to create experiments that can succeed the LHC in pushing the high-energy frontier resulted in the launch of the Future Circular Collider design study in 2014. This design study explores the opportunities a 100 km circumference tunnel in the Geneva area would offer. Such a tunnel could be used for another hadron collider, called FCC-hh, reaching a maximum center-of-mass collision energy of $\sqrt{s} = 100\,\text{TeV}$. This increase, which offers great discovery potential for new phyics, is possible due to the increased tunnel circumference and a research and development program that will result in 16 T magnets. Complimentary uses for the tunnel include an electron-positron collider (FCC-ee) and an electron-proton collider (FCC-eh), that can probe new physics via precision measurements.

FCC-hh reaches the statistics required for many of the searches for new physics at the cost of an increase in simultaneous collisions per bunch crossing (pile-up), which will average at about 1000, a five-fold increase over HL-LHC. This means an overall increased demand for computing resources and efficent reconstruction techniques, but poses particular problems for the processes of event reconstruction that scale unfavorably with pile-up. Track seeding, i.e. the problem of identifying track candidates from a subset of the track detector measurements, is a combinatorial problem that exhibits the worst scaling. This thesis studies the performance of current approaches to track seeding as applied to simulated FCC-hh data. It is shown that while track seeding as done at LHC experiments is not feasible for FCC-hh, the inclusion of timing information can reduce the combinatorics to a level that is comparable to HL-LHC.

Zusammenfassung

Teilchenbeschleuniger und Detektoren ermöglichen seit mehr als 50 Jahren Naturbeobachtungen auf kleinsten Längensskalen. Der Large Hadron Collider (LHC) der Europäischen Organisation für Kernforschung (CERN) in Genf beendet seine Operation nach derzeitigem Plan um 2040, nach der Laufzeit des HL-LHC upgrades. Mehrere Nachfolgerprjekte für den LHC wurden vorgeschlagen, die die bisherigen Beobachtungen vervollständigen und nach neuer Physik suchen könnten, darunter der Future Circular Collider (FCC). Die FCC Designstudie erforscht die Möglichkeiten, die ein neuer Tunnel von 100km Durchmesser für Teilchenbeschleuniger schaffen könnte. Damit kann einerseits ein weiterer Hadron-Beschleuniger (FCC-hh) beherbergt werden, der eine maximale Kollisionsenergie von 100 TeV erreichen würde. Diese Steigerung, die grosses Potential für die Entdeckung neuer Physik birgt, wird durch den grösseren Tunnelumfang und die Entwicklung neuer Dipolmagnete, die bis zu 16T Feldstärke erreichen können, ermöglicht. Andererseits kann der Tunnel auch für einen Elektron-Positron Beschleuniger (FCC-ee) oder einen Elektron-Proton Beschleuniger (FCC-eh) genutzt werden, die das Physikprogramm des Hadron-Beschleuniger komlementieren würden.

FCC-hh erreicht die Luminosität, die zur Suche nach neuen Prozessen notwendig ist, auf Kosten eines Anstiegs an gleichzeitigen Teilchenkollisionen (pile-up), die im Durchschnitt auf über 1000 anwachsen, ein fünffacher Anstieg im Vergleich zum HL-LHC.Dies bedeutet einen hohen Anspruch an Computing-Ressourcen und erfordert effiziente Rekonstruktions-Techniken, stellt aber insbesondere die Prozesse der Rekonstruktion, die ungünstig mit dem pile-up skalieren, vor Probleme. Track Seeding, i.e. die Identifikation von Spur-Kandidaten aus einem Subset der Messungen des Spurdetektors, ist ein kombinatorisches Problem, das am schlechtesten mit zunehmendem pile-up skaliert. Diese Dissertation beschäftigt sich mit der Leistungsfähigkeit von derzeitigen Algorithmen zum Track Seeding, und dem Potential, das Zeitmessungen mit schnellen Spurdetektoren haben, um diese zu verbessern. Sie zeigt, dass während Track Seeding wie am LHC nicht am FCC-hh technisch durchführbar ist, die Berücksichtigung der Zeitinformation die Kombinatorik auf einen Level reduzieren kann, der mit dem HL-LHC vergleichbar ist.

Contents

List of Figures

Chapter 1.

The Standard Model of Particle Physics

1.1. Introduction

The Standard Model of particle physics is a description of nature at the most fundamental level. It is the result of numerous scientific contributions (see [1] and references therein). By the second half of the 20th century it was already almost fully formulated, but only as recently as 2012 one of its last missing pieces was confirmed experimentally (by the successful search for the Higgs boson [2]).

The Standard Model describes the universe in terms of 17 particles and four interactions. The 17 particles are distinguished by several properties: First, their mass influences the kinematics as well as production and decay. They are most commonly categorized based on their spin, an intrinsic quantum number. The twelve particles carrying half-integer spin constitute the fermions. The remaining five particles, which all have integer spin, are bosons. The fermions can be split further, into leptons and quarks with three generations each, as shown in Fig. 1.1. Each generation consists of a charged lepton and a corresponding neutrino, and two quarks with electric charges +2/3 and -1/3 (in units of the elementary charge). The particles in each generation are successively more massive (except for the neutrinos, which were originally assumed massless and for which we experimentally know only upper mass bounds and mass differences squared). The leptons of second and third generation are al-

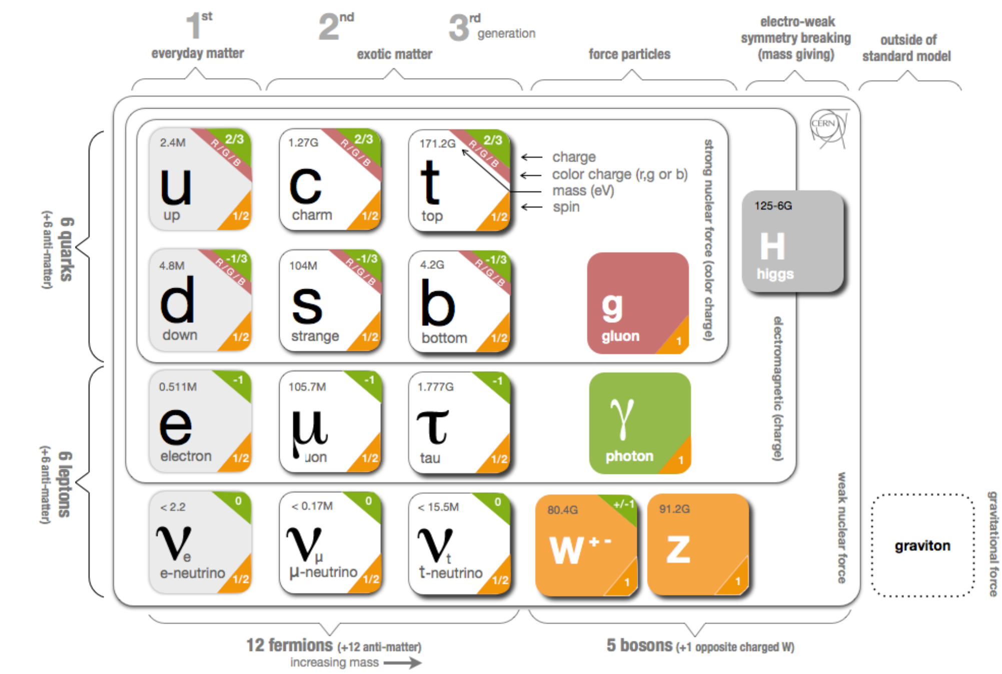

Figure 1.1. Diagram showing a classification of the standard model constituents. Source: [3].

most completely irrelevant to any matter encountered in everyday life. They are only observable in experiments involving high energy particles – one reason why the terms "particle physics" and "high energy physics" have become almost synonymous. For each particle in the Standard Model, there exists an anti-particle with mirrored charge-like quantum numbers (if a charge is zero, like for the photon, it is its own anti-particle).

1.2. Interactions

The bosons mediate interactions between the fermions. The strong interaction describes the dynamics between quarks and gluons and is responsible for nuclear forces. The photon and W- and Z-bosons mediate the electro-weak interactions, and are thus responsible for all electromagnetic phenomena as well as β-decay.

The scope of the Standard Model does not include gravity. As far as interactions between particles are concerned, however, gravitational interaction is several orders of magnitude weaker than the other interactions described here.

1.3. Beyond the Standard Model

No experimental results from accelerators so far directly contradict predictions by the Standard Model. Nevertheless, several different considerations make it clear that it cannot yet be a complete description of the universe at all energy scales. Astrophysical measurements indicate that a large fraction of the matter in the universe interacts in ways not yet observed by particle physicists [4]. The asymmetry of matter and anti-matter in the observable universe raises issues with baryogenesis, the formation of matter during the early universe [5]. Furthermore, some theorists take the need to fine-tune some free parameters of the Standard Model as a hint that it has limited applicability to high energy regimes [6].

Chapter 2.

The Future Circular Collider Study

2.1. Introduction

It is hard to overstate the significance of particle accelerators to high-energy physics. accelerators underwent during the last decades. In the middle of the 20th century it was reasonable and common to write that

> "... most of our present knowledge concerning the properties of high-energy particles was obtained through the study of cosmic-ray phenomena, and, for a long time to come, cosmic rays will probably retain their monopoly over the energy region beyond 10 [GeV]" [7].

50 years later, the energy reach of dedicated particle colliders has surpassed 10 TeV. While this is still unlikely to reach the scales of the most energetic recorded cosmic rays, accelerators enable precision studies of easily repeatable collisions in a controlled environment. This has led to many discoveries at colliders, from the W- and Z-bosons to the structure of the proton.

The latest of these discoveries concerns the Higgs boson, for which experimental evidence was found in 2012 at the Large Hadron Collider (LHC) at the European Organization for Nuclear Research (CERN) in Geneva. This was the last particle predicted by the Standard Model.

2.1.1. European Strategy for Particle Physics

The LHC will cease operations after the upgrade to the High-Luminosity (HL) LHC which will allow it to collect an order of magnitude more data than planned until 2030. The exploitation of the full LHC potential is one part of CERN's mission, but it is also tasked with the development of a successor project, as formulated in the European Strategy for Particle Physics :

> "CERN should undertake design studies for accelerator projects in a global context, with emphasis on proton-proton and electron-positron high-energy frontier machines. These design studies should be coupled to a vigorous accelerator R&D program, including high-field magnets and high-gradient accelerating structures, in collaboration with national institutes, laboratories and universities worldwide." [8]

The result of this effort is a Conceptual Design Report (CDR), published in four volumes [9, 10, 11, 12], describing the potential of colliders making use of large tunnel infrastructure.

2.1.2. Accelerator Infrastructure

The tunnel infrastructure is, due to its costly and permanent nature, one of the most important choices for a collider experiment. An underground installation shields the environment from operational radiation and the detectors from cosmic ray backgrounds, and it allows to build a large installation in a densely populated area.

Fig. 2.1 shows the proposed layout for the tunnel that would host the Future Circular Collider. The layout maximises the circumference under the constraint of minimizing geologically problematic terrain. The tunnel also needs to pass the existing accelerators at CERN in close proximity in order to use them for injection transfers.

Avoiding the limestone of the Jura mountains and the pre-alps, the proposed layout reaches a circumference of approximately 100 km. This layout includes a passage of the tunnel under the lake of Geneva – a novel feature of this kind of installation, but deemed feasible.

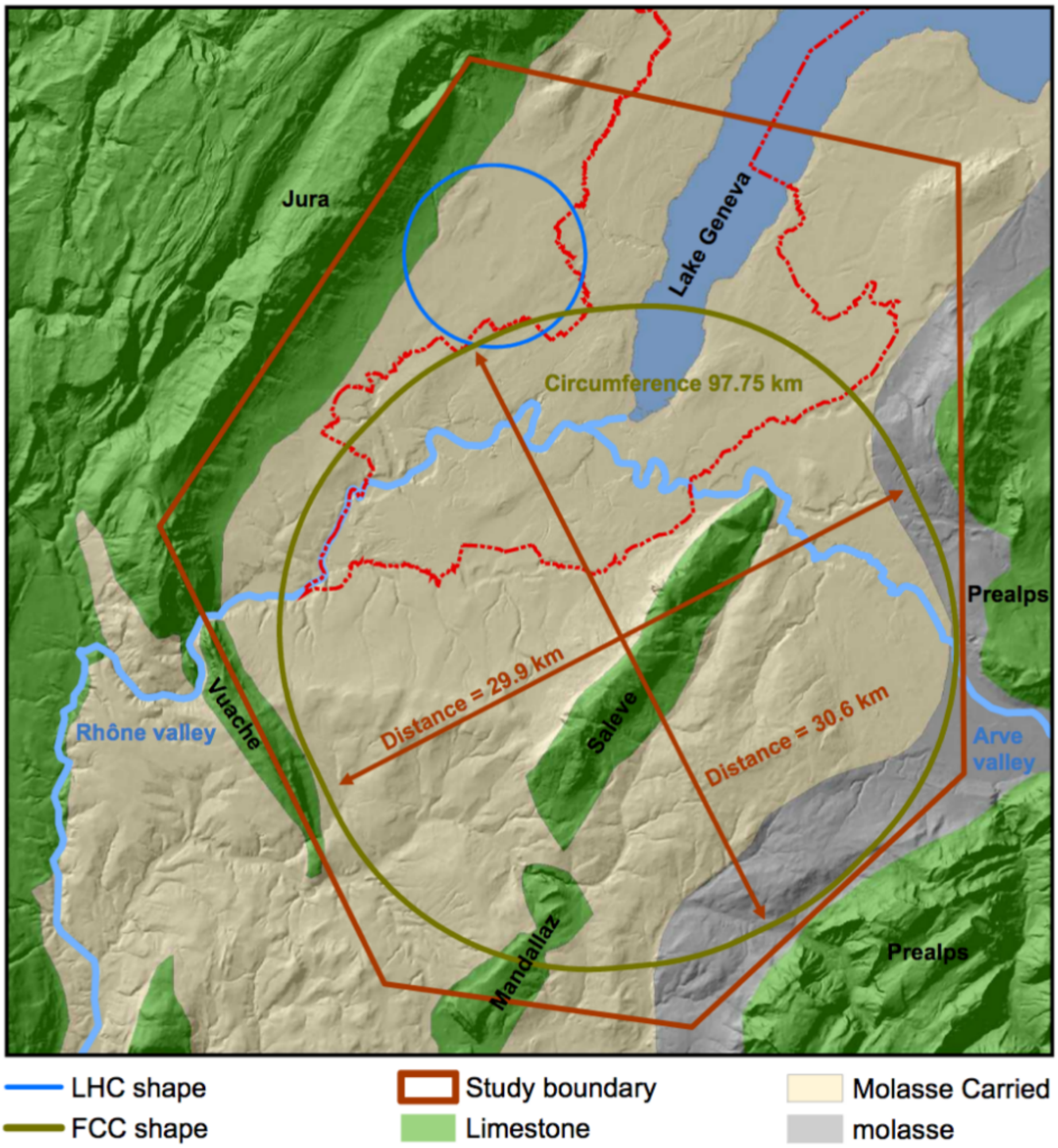

Figure 2.1. Proposed layout for a tunnel of 100 km circumference hosting FCC-ee/FCC-hh in the Geneva region. Source: [13].

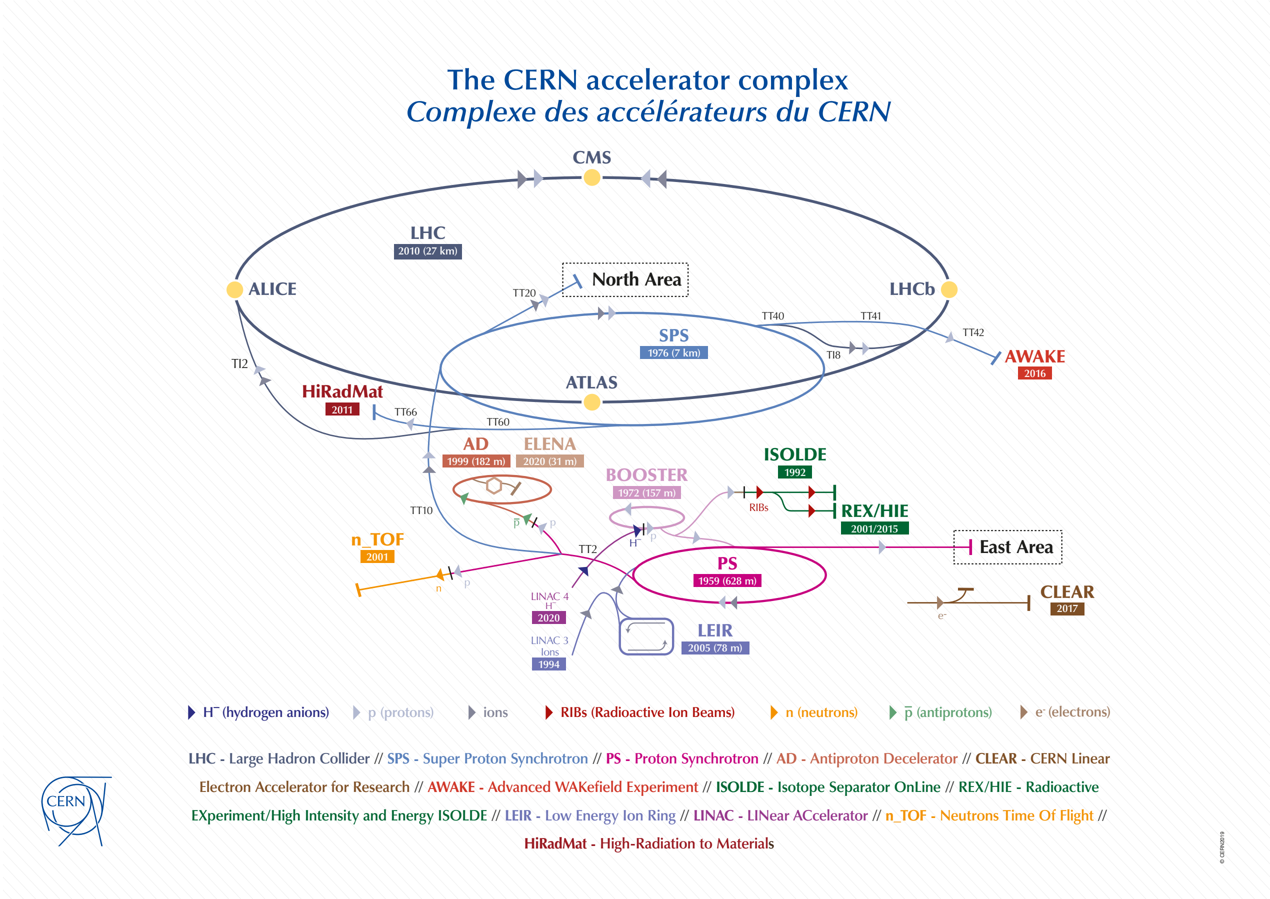

Figure 2.2. The CERN accelerator complex

2.1.3. Injection and Pre-Collider Acceleration Complex

The CERN accelerator complex (shown in Fig. 2.2) can be used as an injection chain for FCC-hh.

However, to reach the baseline injection energy of 3.3 TeV, one stage, the so-called High Energy Booster (HEB), must be added [10]. The LHC tunnel is one option for this last injector ring, but outfitting the SPS with superconducting magnets or housing the HEB alongside FCC-hh in the 100 km tunnel have also been proposed [14].

2.1.4. Collision Energy

Circular particle accelerators at the high-energy frontier are limited by the bending power of the dipole magnets used to keep the beam on its trajectory. The increase in the collider circumference by a factor of 3.6 with respect to the LHC (27.5 km) means that the peak center of mass collision energy can increase by roughly the same factor. Together with a research and development program aimed at increasing the maximum field strength of the dipole magnets from 8 T at the LHC to 16 T, the FCC-hh is expected to reach 100 TeV.

From a historical perspective, the beam energy available at colliders has grown exponentially, gaining roughly a factor of ten every seven years for most of the twentieth century. However even FCC-hh actually does not keep pace with this historical development as shown in Fig. 2.3, a timeline of available beam energies first compiled by M. Livingston.

2.2. Overview of Proposed Future High-Energy-Frontier Colliders

Besides the different accelerator options of the Future Circular Collider, other plans for linear as well as circular colliders at different sites are being considered by the High-Energy Physics community.

In this section the proposed accelerators and their different objectives and methodologies are summarised.

2.2.1. FCC-ee

FCC-ee is a circular electron positron collider with a direct energy reach of up to 350 GeV. The clean event signatures allow for precision measurements that can probe new physics at higher energy scales than those directly accessible in the experiment. FCC-ee will produce more than 1.3×10^{11} Z $/\!\!\rightarrow \tau\tau$ events, allowing for precision studies of τ properties [16]. The design presented in the CDR assumes two interaction points for experiments, with ongoing studies on an option with four interaction points.

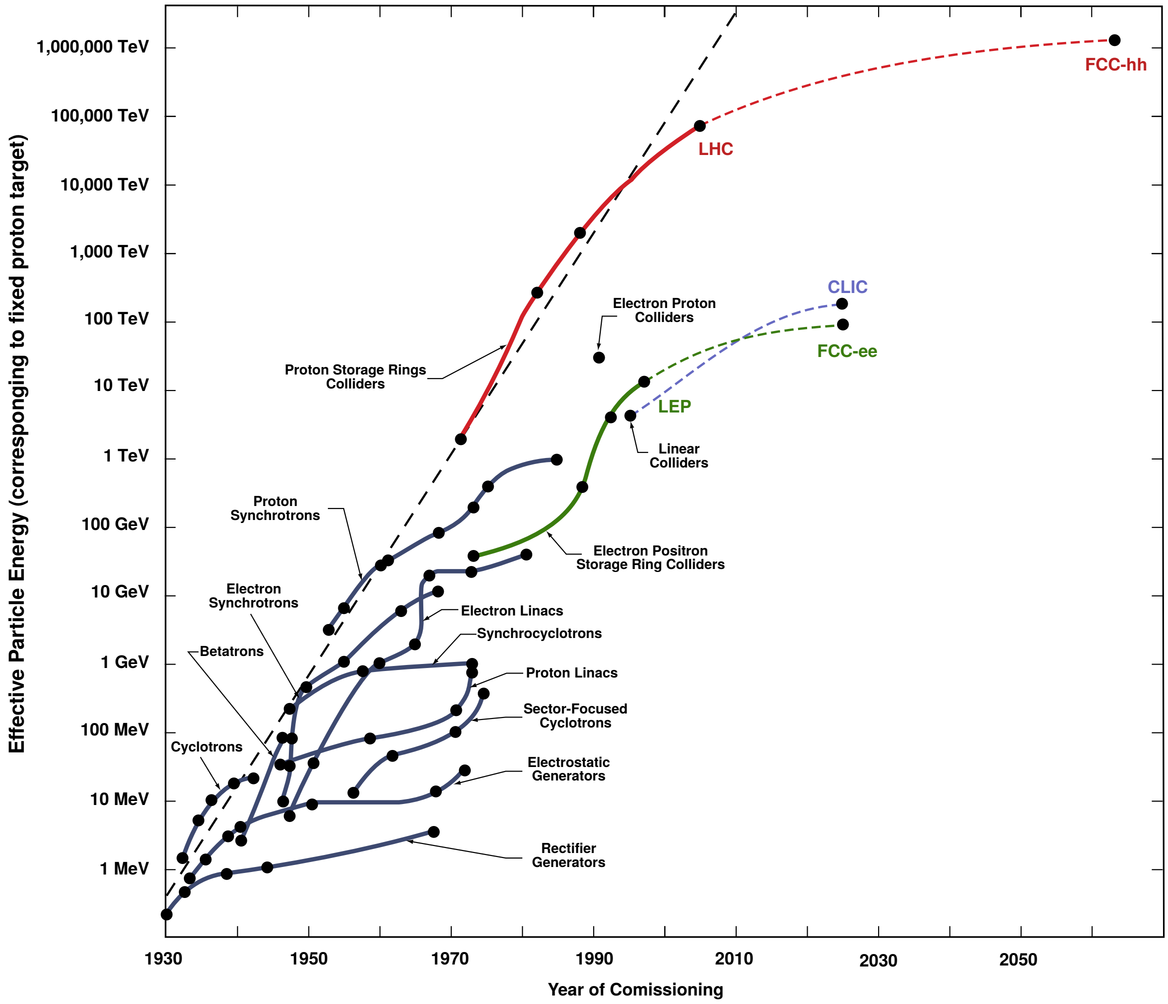

Figure 2.3. "Livingston Chart" – a plot of the development of effective beam energies at particle accelerators over time. This graph does not account for luminosity and other collider parameters that are significant to the physics goals of experiments. Adapted from [15] to include the FCC and CLIC designs.

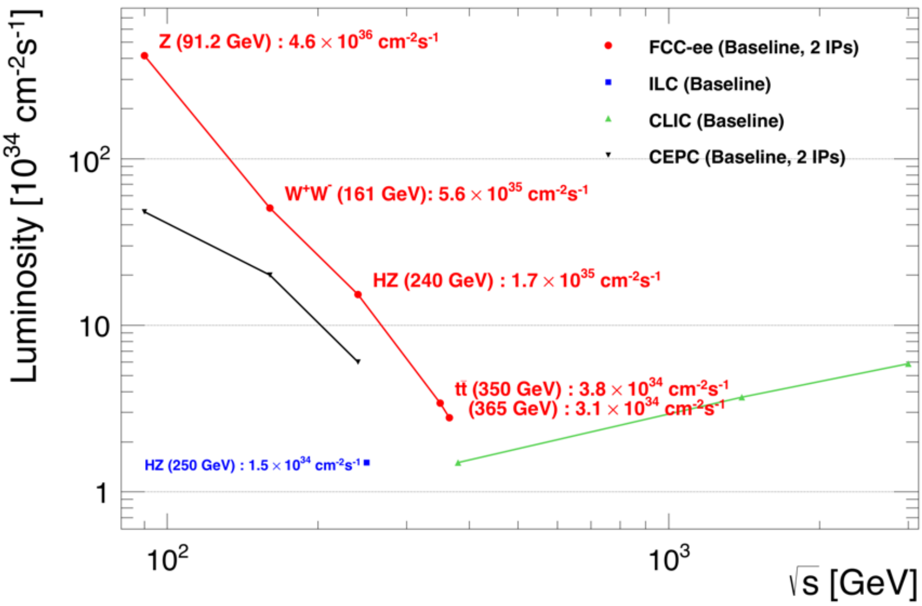

Figure 2.4. Performance of planned lepton colliders in terms of luminosity and center-of-mass collision energy. Source: [9].

Compared to hadron colliders such a machine has considerably lower event complexity and thus detectors at FCC-ee have less stringent technical requirements on radiation hardness, for example.

The detectors need, on the other hand, to be optimised for precision measurements. Low mass tracking detectors are thus a very imporant part of the overall concept. The detector concepts for FCC-ee thus include different technologies such as drift chambers [17]. The requirements are furthermore very similar to detectors at CLIC (see following sections), which have been adapted in a CLIC-like detector concept (CLD) [18].

2.2.2. FCC-eh

Concepts for a hadron-electron collider at CERN were already proposed as a possible use of the LHC tunnel [19]. The proposed Large Hadron-electron Collider (LHeC) would collide a 60 GeV electron beam from an energy recovery linear accelerator with 7 TeV protons accelerated by the LHC. Electron-proton collisions at this energy scale allow for more precise measurements of the proton structure. Compared to previous e-p experiments such as HERA [20] the luminosity would be at least a factor of 100 greater. LHeC can thus reduce systematic uncertainties for measurements at proton colliders, but also investigate quark-gluon dynamics as well as lepton-parton bound states. Even better performance can be achieved by FCC-eh, which could use a 50 TeV proton beam from FCC-hh for collisions with the same electron beam as LHeC. This experiment could run concurrently with proton-proton collisions at the FCC-hh.

2.2.3. Compact Linear Collider (CLIC)

CLIC is a linear alternative to the circular high-energy frontier experiments described here. Without the need to bend the beam on a circular trajectory and the resulting losses due to synchroton radiation, CLIC can reach a maximum center-of-mass energy of 3 TeV in electron-positron collisions with a tunnel of 50 km length, with lower-energy stages at reduced length. The improved energy reach of linear colliders comes at the cost of reduced luminosity (compare Fig. 2.4). Having started already in 1985, the CLIC study is more advanced compared to the FCC studies and already had time to prototype many of the novel technologies in its design, needed for example for the high acceleration gradients of up to 100 MeV/m [21].

Fig. 2.5 shows the three different tunnel extensions that would house the three stages of CLIC.

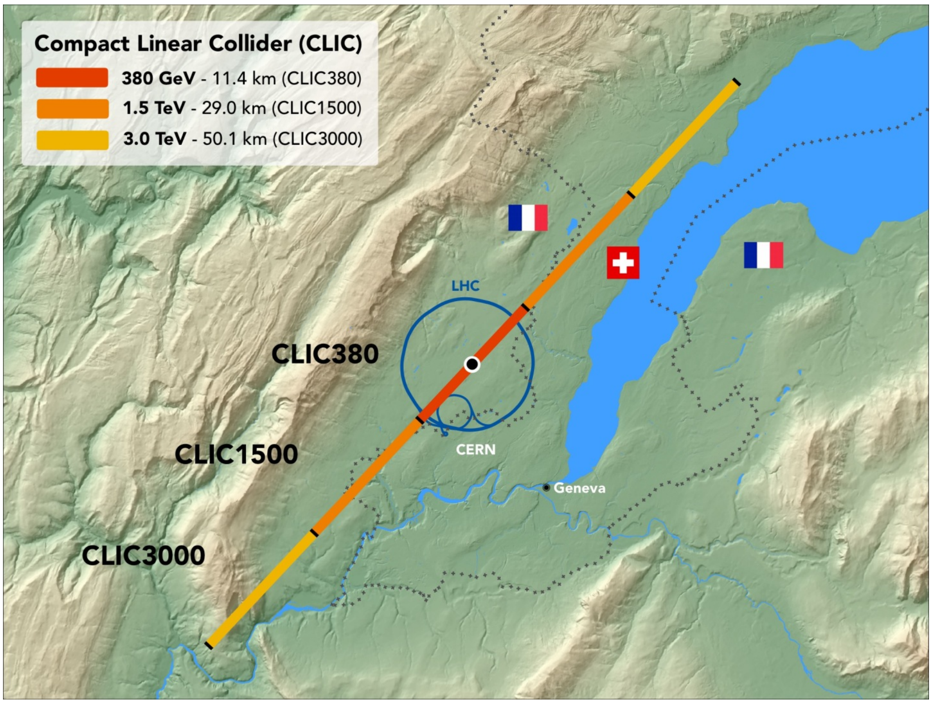

Figure 2.5. Proposed layout of the three stages of the Compact Linear Collider in the Geneva area. Source: [22].

2.2.4. International Linear Collider (ILC)

The International Linear Collider [23] is a proposed linear electron-positron collider to be hosted in Japan. The ILC could act as a Higgs factory at a center-of-mass collision energy of $\sqrt{s} = 250\,\text{GeV}$ with possible upgrade steps up to $1\,\text{TeV}$. In many regards the ILC design is similar to CLIC, but uses superconducting cavities for acceleration.

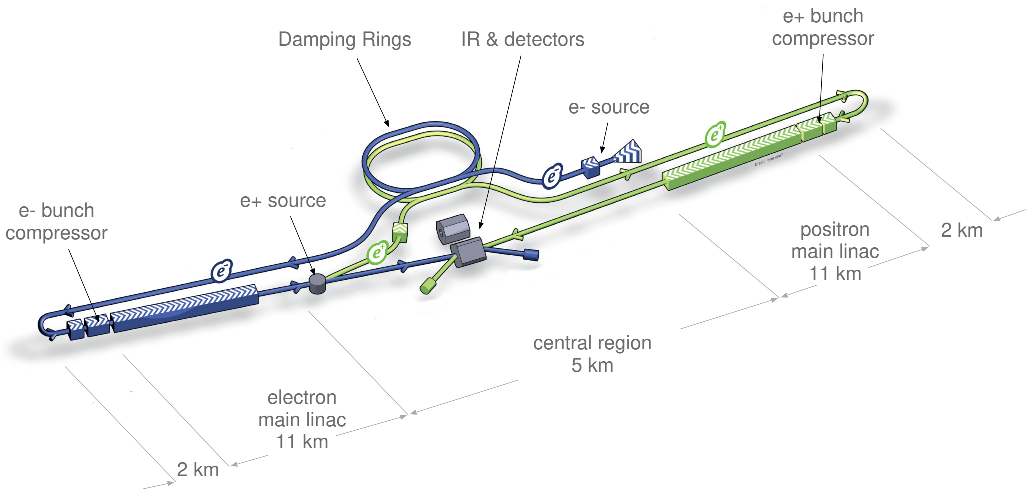

Figure 2.6. Schematic layout of the ILC accelerator and its subsytems. Source: [23]

2.2.5. Circular Electron-Positron Collider (CEPC)

CEPC is an alternative to FCC-ee, based in China. It is designed to operate at the Z invariant mass, do a W- threshold scan and operate as a Higgs factory at 240 GeV [24]. Similar to the Future Circular Colliders, a hadron collider (Super proton-proton Collider, SppC) could use the tunnel infrastructure after the runtime of the CEPC.

2.3. The FCC-hh Detector Concept

This section summarizes the overall FCC-hh detector concept as presented in the FCC-hh Conceptual Design Report [11].

2.3.1. Interaction Points

The layout of the interaction points of the FCC-hh accelerator shown in Fig. 2.7 foresees two high-luminosity experiments and two additional experiments at reduced luminosities. Nevertheless, this thesis and the conceptual design report only study a single concept that is expected to serve as a "proof-of-principle" and baseline to identify directions for future research and development, as well as to demonstrate the feasibility of such a detector.

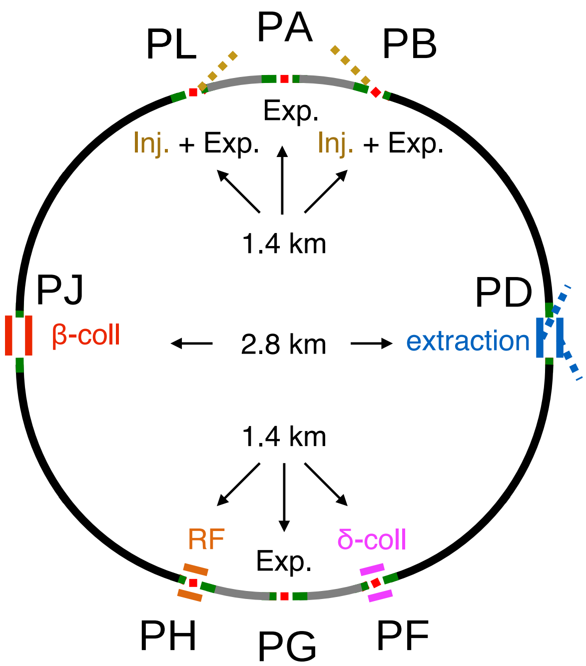

Figure 2.7. Schema of FCC-hh interaction points. Two interaction points (PA, PG) can accomodate high-luminosity experiments, two additional experiments could be at PL and PB. PJ, PD, PH and PF are needed for beam collimation, acceleration, and extraction. Source: [11].

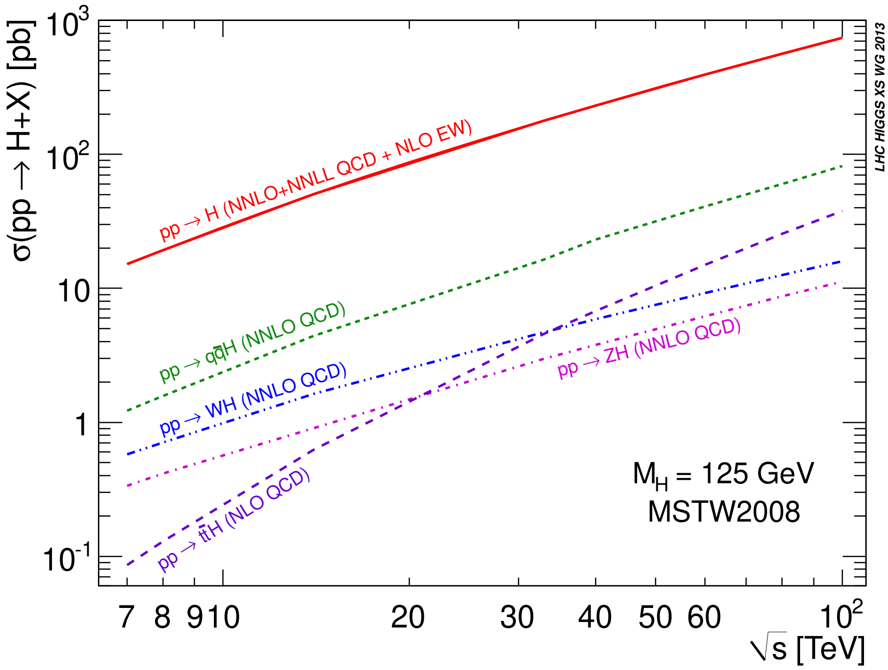

Figure 2.8. Cross sections for Higgs Production from 7 to 100 TeV. Source: [25].

2.3.2. Physics: Motivation and Detector Requirements

At the time of writing, no clear direction for physics beyond the Standard Model has emerged from the operation of the LHC. With 50 TeV proton beams FCC-hh has the greatest direct discovery reach of all future collider projects currently under consideration. Moreover, thanks to the integrated luminosity of 30 ab^{-1} to be collected over the whole period of data taking, it lends itself to the measurements of the Higgs boson, its couplings and other standard model parameters. The Higgs program of FCC-hh is supported by the fact that Higgs production cross sections rise disproportionately when increasing the collision energy from 14 TeV to 100 TeV. Monte Carlo calculations show that for example the cross section of Higgs production in association with a top quark pair increases by a factor of ~ 60 when going from LHC to FCC-hh energies (see Ref. [25] and Fig. 2.8). This is an interesting final state as the two b-jets constitute a good triggering setup. The total cross section for proton-proton collision on the other hand only increases from 73.1 ± 7.7 mb to 105.1 ± 2.0 mb, an increase of only 45% [9].

The LHC experiments are a natural baseline for detectors at a 100 TeV collider.

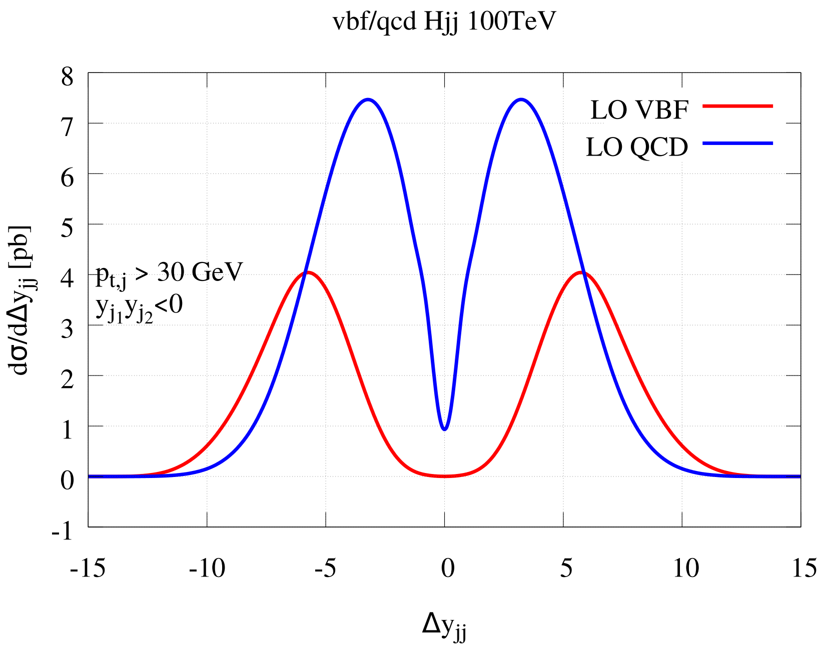

Figure 2.9. Jet rapidity difference of Higgs (H_{jj}) production in Vector Boson Fusion and QCD. Source: [26].

The mentioned studies have, however, identified some areas with novel and more stringent detector requirements. Studies of the potential for QCD, top quark and flavour physics and precision electroweak measurements, as well as searches for dark matter and dark sectors, massive neutrinos, flavour anomalies and other phenomena beyond the Standard Model can be found in Ref. [9].

A very fundamental change for the overall detector design is the detector coverage: Fig. 2.9 shows that the directions of the most forward jets produced in Vector Boson Fusion (VBF) differ, on average, by more than 6 rapidity units. Together with other physics objects that are boosted more to the forward region of the detector, these calculations led to the requirement of extending the detector coverage to $\eta = 6$ (for the definition of η and y, see the next chapter).

Many of the Higgs measurements as well as searches for physics beyond the Standard Model depend on the capabilities to reconstruct and tag heavy and light flavour jets. Searches for heavy resonances like $Z' \to t\bar{t}$ and $Z' \to b\bar{b}$ require tagging high-p_T jets up to energies of several TeV [27].

Figure 2.10. Computer rendering of the FCC-hh baseline detector model. Source: [11].

2.3.3. Detector Subsystems

The baseline FCC-hh detector (see Fig. 2.10), as documented in the conceptual design report, is in many ways similar to current LHC general-purpose detectors like ATLAS and CMS. Its overall dimensions are about 50 meters in length and 20 meters in height. Except for small features, it is rotationally symmetric under rotations around the beam axis.

Fig. 2.11 shows the layout of the detector and its subsystems in the longitudinal plane. In the central region ($|\eta| < 2.5$) the tracker extends to a radius of 1.7 m. The Electromagnetic CALorimeter (ECAL) and the Hadronic CALorimeter (HCAL) fill the space up to the central solenoid magnet. The overall calorimeter thickness is more than 10.5 nuclear interaction, to ensure containment of high energy showers [28].

A central muon detector is located outside of the central magnet. In the forward region, the detector consists of endcap trackers and calorimeters, and a forward detector with its own magnet to provide additional coverage up to $|\eta| < 6$. Three track detector layers between the central and forward tracker help to improve the extrapolation of forward tracks.

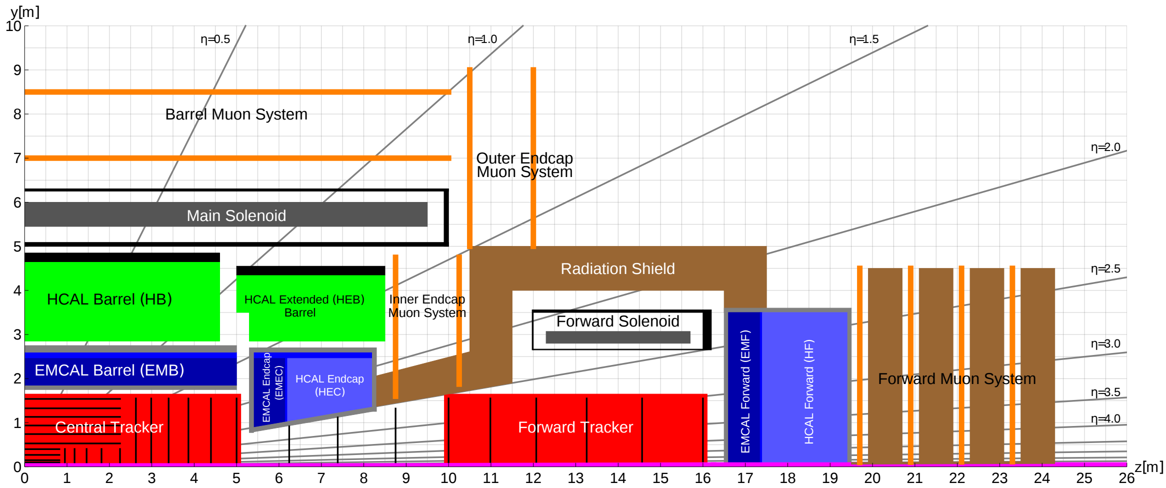

Figure 2.11. Longitudinal layout of the FCC-hh baseline detector model, indicating the different detector subsystems. Source: [11].

2.3.4. Radiation Environment

The radiation levels during operation are the result of the beam parameters and the material distribution in the cavern. Especially the calorimeters are activated by the high particle rates of FCC-hh, as can be seen in Fig. 2.12, and shielding must be put in place to protect electronics and allow for maintenance.

2.3.5. Magnet System

The magnet system (shown in Fig. 2.13) is discussed in the description of the tracker design in Chapter 5. For economical reasons, no return yoke or shielding is foreseen; the magnetic field in the experimental cavern is thus higher than at LHC experiments, but a service cavern for sensitive equipment is anyway foreseen.

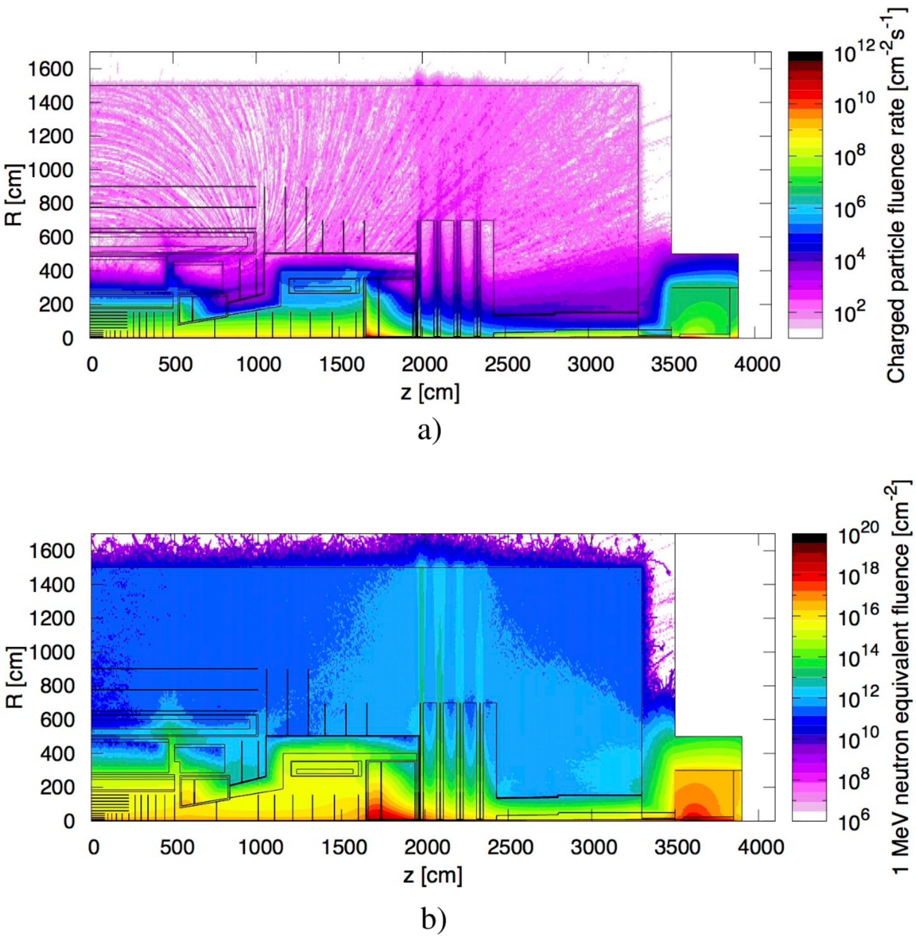

Figure 2.12. Simulated radiation environment for the FCC-hh detector. Fig. a) shows the charged particle rate for the peak luminosity of 30×10^{34} cm^{-2} s^{-1}. Fig. b) shows the 1 MeV neutron equivalent flux for the full integrated luminosity of 30 ab^{-1}. Source: [11].

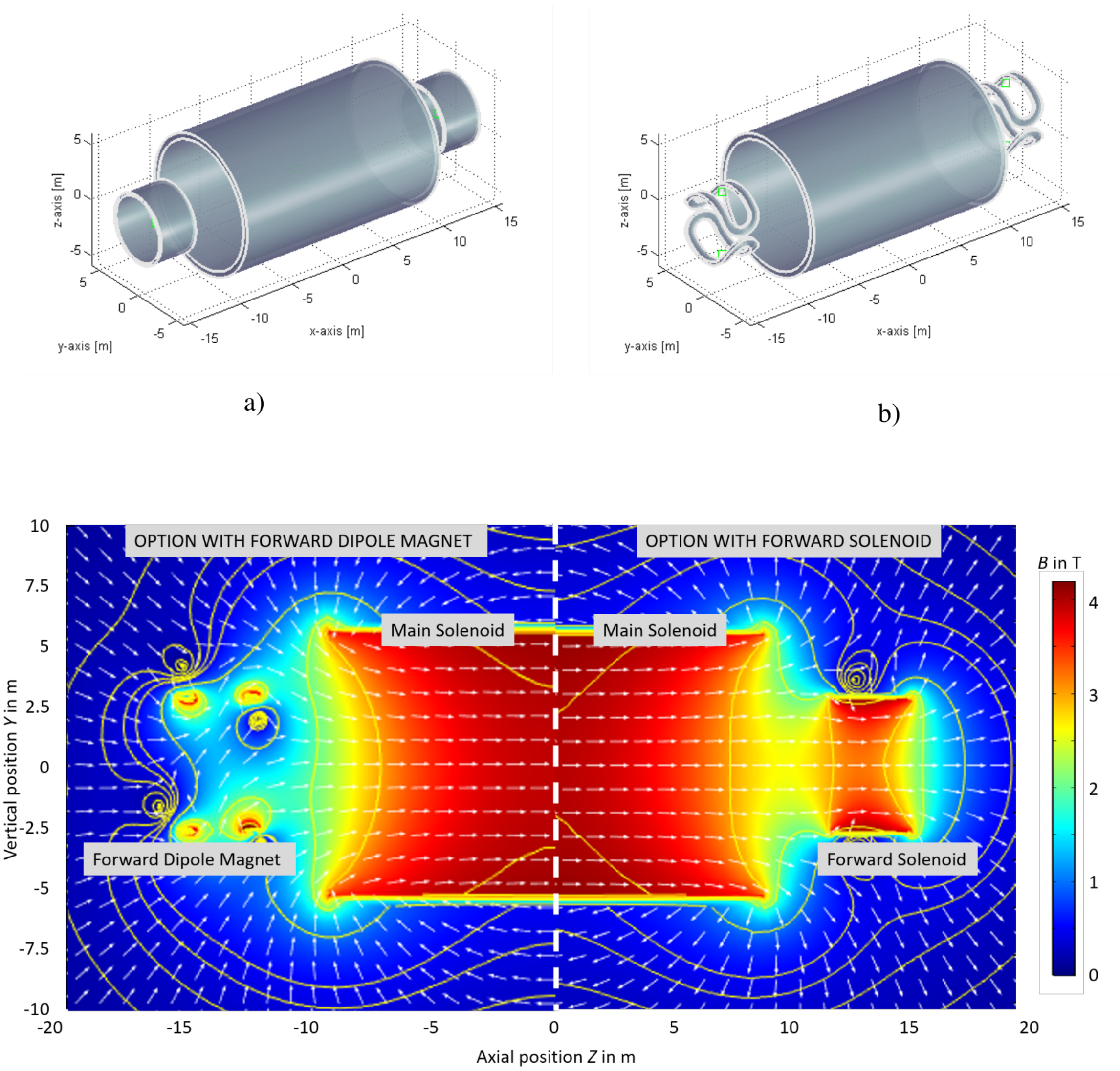

Figure 2.13. Magnet system designs and simulated field maps for the FCC-hh detector. Source: [11].

Chapter 3.

FCC-hh Collision Parameters

3.1. Introduction

This chapter presents more detailed information on FCC-hh as motivation and reference for the FCC-hh detector design that is presented in this thesis. As shown in later chapters, the high luminosity is one of the central design challenges for detector performance and thus the focus of this work. A more complete picture of the novel accelerator design technologies and physics studies that shape FCC-hh can be found in the corresponding conceptual design report volume [11].

3.2. Machine Parameters

The defining feature of FCC-hh is the center-of-mass collision energy of 100 TeV, made possible by a combination of the increased tunnel circumference and high-field dipole magnets with a foreseen field strength of 16 T. The beam will consist of 10400 bunches, each bunch consisting of 1×10^{11} protons. The bunch spacing of 25 ns and corresponding collision frequency of 40 MHz are identical to the LHC parameters.

3.2.1. Simultaneous Collisions: *Pile-up*

The actual number of proton-proton collisions during each bunch crossing is random, following a Poisson distribution determined by the beam parameters. All proton interactions beside the one giving rise to the signal – the process of interest, usually a

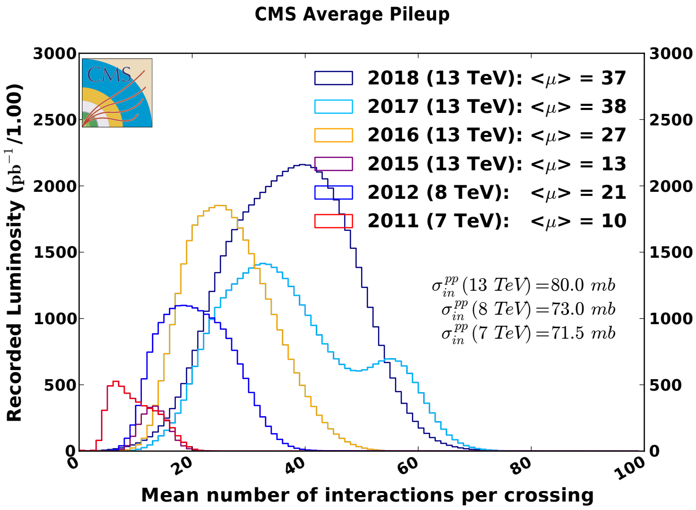

Figure 3.1. Distribution of the number of simultaneous proton-proton collisions during events recorded by CMS. Source: [30].

hard scatter event – are referred to as *pile-up* and their properties are described in the next section. At the LHC, the mean number of pile-up was below 21 for most of Run 1 and Run 2, before increasing up to 60 for the upcoming Run 3 (see Fig. 3.1). For the High-Luminosity upgrade after Run 3, the average pile-up is estimated to increase to 128, with a fraction of about a third of the events even with mean pile-up 140 [29].

The mean of the pile-up distribution μ is approximately ~ 1000 at the FCC-hh for beams at peak luminosity. This number does not represent an upper or lower limit for pile-up – some bunch crossing will produce more or less pile-up events according to the variance of the Poisson distribution. Furthermore, the peak pile-up rates only apply for some fraction of data taking. The number of protons in the beam decreases with time due to losses in collisions ("burn-off"). Dumping a beam and injecting a new one takes several hours, and the peak luminosity curve is the result of optimization studies as shown in Fig. 3.2.

The beam properties also determine the size and shape of the *luminous region*, the volume in which collisions will occur. The detailed kinematics of the bunch crossing and the use of *crab cavities* to compensate the crossing angle are described in Ref. [31]. For detector simulations, the luminous region can be well approximated by a 4-dimensional Gaussian distribution centered at the origin, with standard deviations

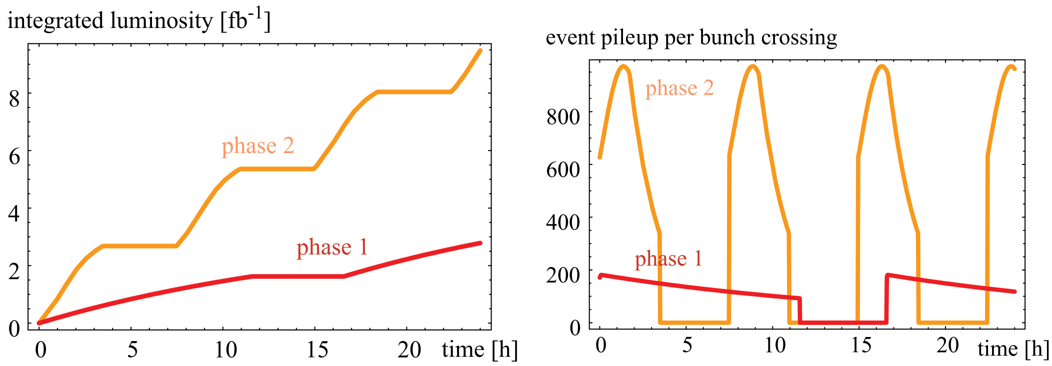

Figure 3.2. Optimized luminosity and pile-up rates at FCC-hh over the course of 24 hours of data taking. Source: [32].

$\sigma_x = \sigma_y = 50$ microns, $\sigma_z = 40$ mm and $\sigma_t = 180$ ps. The following chapters will investigate how the time spread of pile-up collision vertices can be used to mitigate their effect on track reconstruction. The time and spatial dimensions of this distribution are assumed to be uncorrelated.

A consequence of the short bunch spacing of 25 ns is that collision products have barely left the detector by the time the next bunch collides. Some detector subsystems such as the liquid argon calorimeter have sensitivity windows that are larger than the 25 ns bunch interval and can thus be influenced by previous events. This type of pile-up is referred to as out-of-time pile-up as opposed to the in-time pile-up from the same bunch crossing previously discussed. The techniques to mitigate out-of-time pile-up are mostly the same as for in-time pile-up. For track reconstruction studies as presented in this thesis, however, out-of-time pile-up is of limited importance.

3.3. Pile-up Events

The cross sections for many interesting processes are exceedingly small (see Fig. 3.3). The associated events thus need to be selected from a large number of collisions using a “trigger”, a system that can identify the interesting events from the limited detector information available in the short time between collisions.

The properties of pile-up collisions are, in contrast, determined by the processes with the biggest cross section. These processes include both elastic scattering, i.e. energy

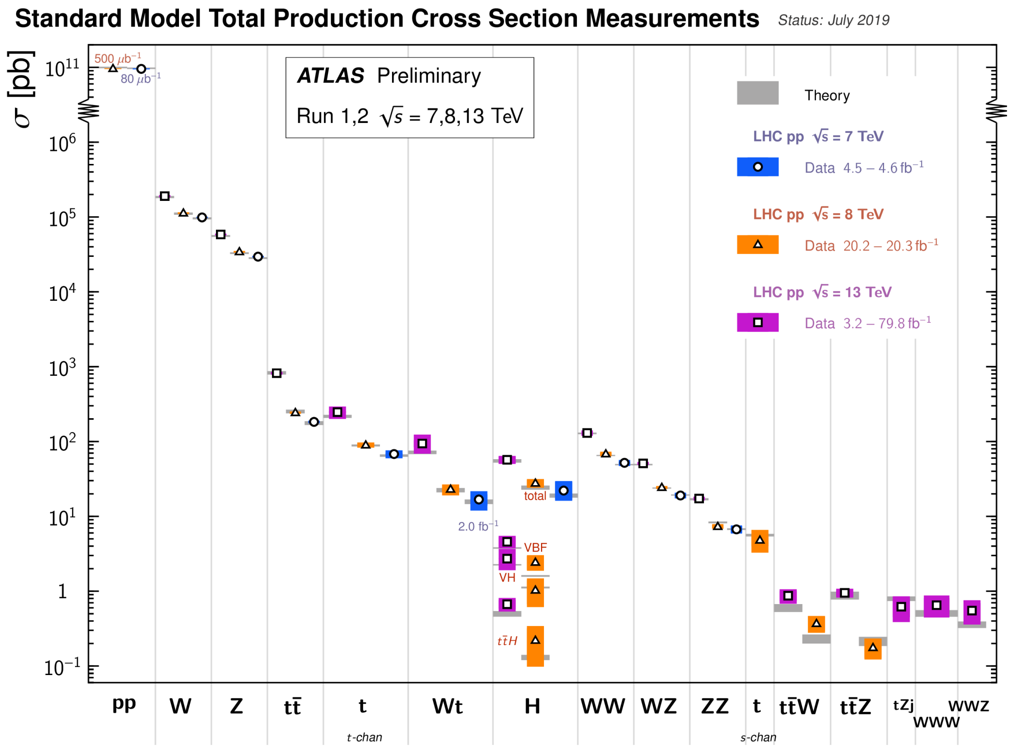

Figure 3.3. Total production cross section measurements by ATLAS, compared to theory predictions. Source: [34].

transfer between the protons without a change in the particle content of the event, as well as inelastic scattering. The most common inelastic proton-proton collisions can be further subdivided into single or double diffraction (one or both of the protons enter an excited state and subsequently break apart, producing particles predominantly in the forward direction), and non-diffractive processes. Non-diffractive processes are dominated by soft, i.e. low transverse momentum quantum chromodynamics (QCD).

For technical reasons (such as the finite detector acceptance) it is difficult to record a truly random, unbiased sample of collisions at colliders. The bias associated with selecting events can however be minimized. A selection that tries to come as close as possible to an unbiased sample is referred to as a minimum bias selection. By convention, diffractive processes are not counted as minimum bias events, which thus are dominated by non-diffractive QCD processes [33].

A comprehensive study of the properties of minimum bias events at FCC-hh and a

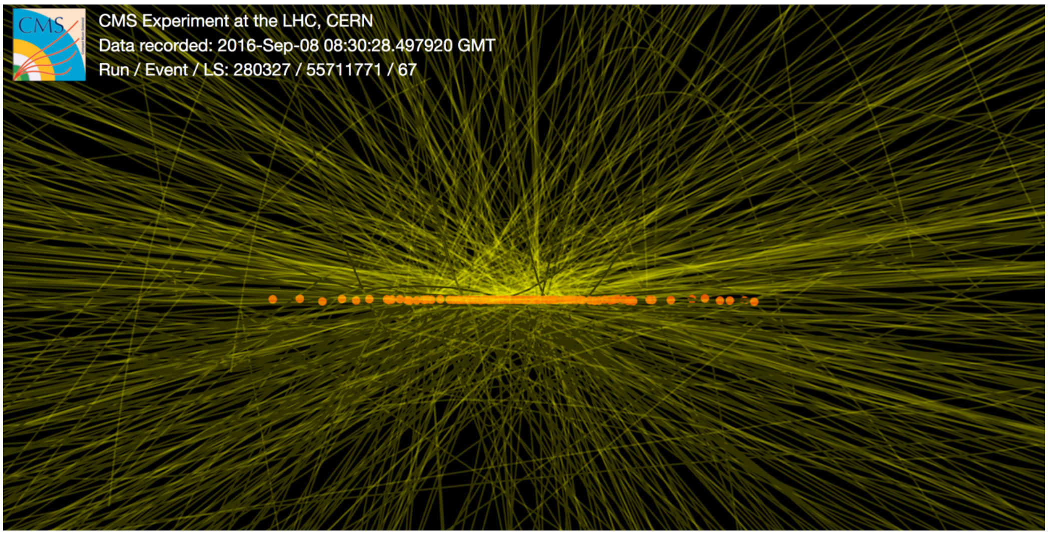

Figure 3.4. Visualization of a collision event with 86 reconstructed vertices recorded in 2016 by CMS. Source: [38].

comparison of different event generators can be found in Ref. [35].

The minimum bias events in pile-up should be distinguished from the Underlying Event (UE), which refers to the low-p_t remainder of a hard scatter event [36].

3.3.1. Charged Particle Multiplicity

On average, minimum bias proton-proton collisions at 100 TeV are predicted to yield 150 ± 20 charged particles. This allows to give a first estimation of around 1.5×10^5 charged tracks at a 1000 pile-up event, not accounting for material interactions in the detector. This is comparable to a single central lead-ion collision at the LHC [37], which however operates at a significantly reduced interaction rate and only has one track vertex to reconstruct.

Line plots of trajectories of charged particles around the interaction region have been used to visualize the pile-up density (see for example Fig. 3.4).

In FCC-hh conditions even these visualization techniques fail to capture the track density. Alternative visualization techniques have been proposed [39, 40].

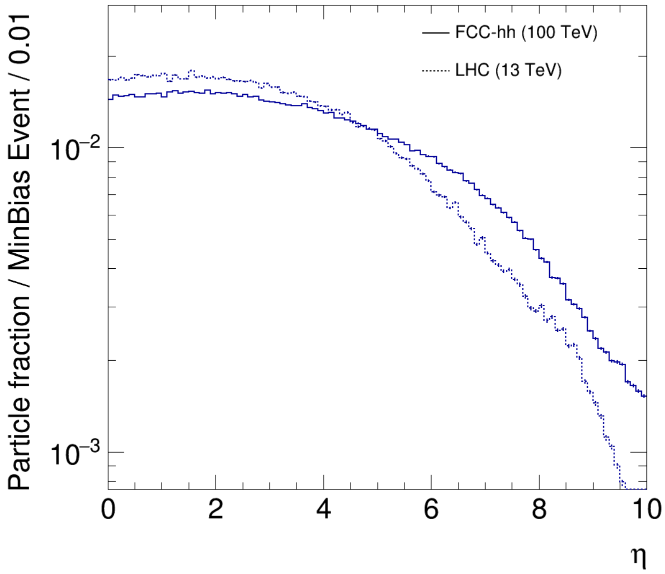

Figure 3.5. Distribution of charged particle pseudorapidities in minimum bias events at 13 and 100 TeV.

3.3.2. Momentum Distribution

For the purposes of track reconstruction, the transverse and longitudinal distributions of charged particle momenta are of interest. Fig. 3.5 and Fig. 3.6 show FCC simulations of the momentum spectra of charged particles in minimum bias events at 100 and 13 TeV. Pythia 8 was used to generate non-diffractive soft QCD processes at the given center-of-mass energies. The overall agreement shows that minimum bias events at FCC will not be substantially different, compared to the LHC. There is, however, a slight, but clear tendency towards tracks that are directed more in the forward direction and possess higher transverse momenta.

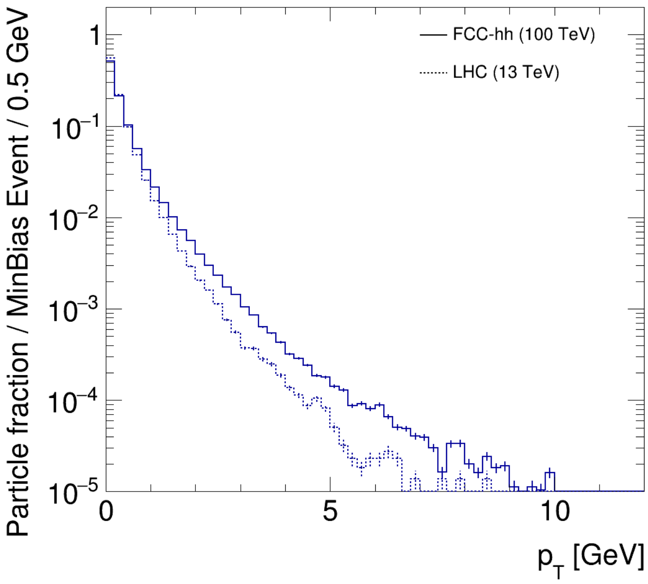

Figure 3.6. Distribution of transverse momenta of charged particles in minimum bias events at 13 and 100 TeV.

3.3.3. Vertex Distribution

The location and timing of the pile-up vertices is the result of the geometry and dynamics of the bunch crossing. For the purposes of this work, the distributions of the vertices along the coordinate axes x, y, z, and t are taken to be uncorrelated normal distributions, as shown in Fig. 3.7.

The longitudinal and time coordinates are certainly somewhat correlated, as protons are expected to collide while the bunches overlap. The tails of the time distribution are limited to the areas where bunches still overlap at that given time, which is typically closer to collision center.

The average distance between two pile-up vertices is a crucial parameter for track reconstruction, due to the possibility of misreconstructing close vertices as a single vertex.

Fig. 3.8 shows the distribution of longitudinal separation of pile-up vertices along the beam line. The most likely value of the distance between two neighboring vertices is more than one magnitude smaller at FCC-hh compared to configurations corresponding to HL-LHC [42]. Fig. 3.7 hints at one possible pile-up mitigation strategy that is described in this work. If the timing resolution of the detector can be made

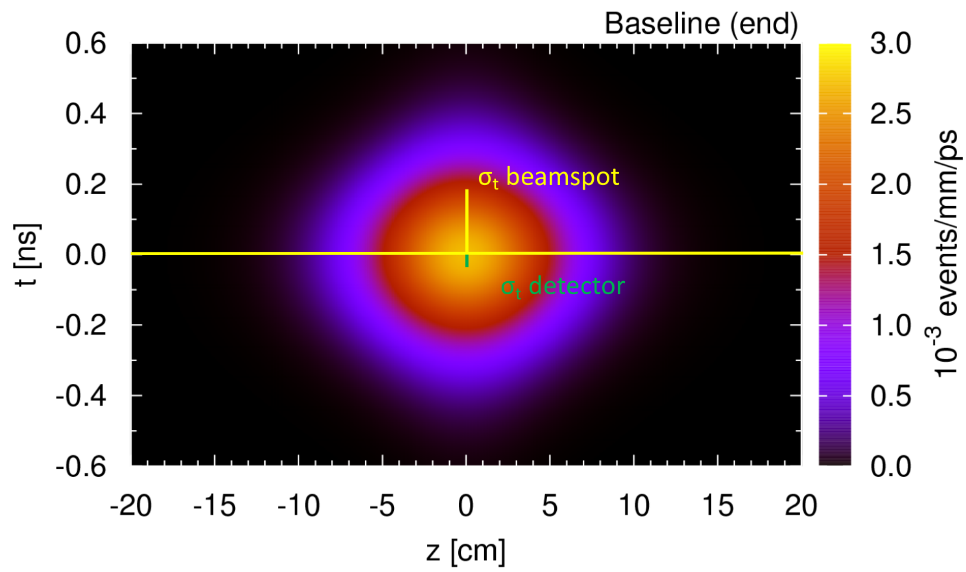

Figure 3.7. Distribution of pile-up vertices in the t-z plane. The expected time resolution of the tracker is indicated in green, in order to illustrate the potential to discriminate vertices. Source: [41].

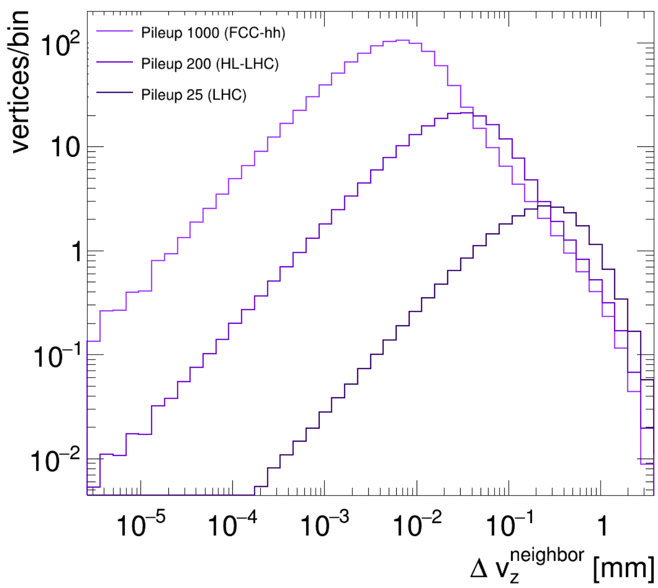

Figure 3.8. Distributions of the longitudinal separations of pile-up vertices. For comparison, the configurations corresponding to LHC and HL-LHC baseline luminosities are shown also.

substantially better than the time spread of pile-up vertices, the time information can be used to discriminate between them.

Chapter 4.

Review of Track Detection and Reconstruction

4.1. Introduction

Tracking detectors have been instrumental for particle physics since the early beginnings. This chapter briefly summarizes the experimental techniques that have become standard in collider experiments to provide context and lay the groundwork for the studies of the FCC-hh detector in the following chapters. Every experiment uses slightly different definitions and notations to describe particle tracks. Consistent notations for the FCC detector geometry and the track model that are used throughout the rest of the text are also introduced.

4.2. Definitions and Conventions

Particle detectors are built around the interaction points of the collider. As discussed in Ch. 2, the interaction points themselves are not point-like, but a region in space, determined by the geometry of the beams. To describe the detector and its measurement spatially, it is therefore natural to use a coordinate system with its origin in the center of the luminous region. Here, a cartesian coordinate system with the following conventions is used:

The positive x-axis extends from the origin in direction of the center of the circle

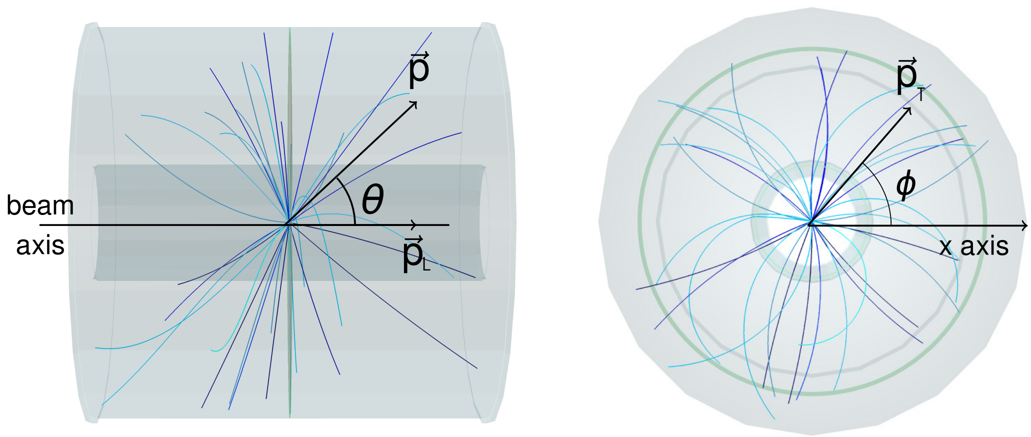

Figure 4.1. Convention for coordinate systems and transverse/longitudinal momentum in FCC studies. Source: [43]

defined by the beam (see Fig. 4.1). A tangent to the beam line at the origin defines the z-direction. The y-axis runs orthogonal to x and z, with the upward direction with respect to the gravitational field of the earth declared positive. The sign convention for z is finally chosen so that the positive directions satisfy the right hand rule.

Whenever convenient, standard polar coordinates r and ϕ are used in the transverse x-y plane. In the longitudinal plane, the polar angle θ and especially in the context of hadron colliders, the pseudo-rapidity

$$\eta = -\ln\left[\tan\left(\frac{\theta}{2}\right)\right]$$

are used as well. The preference for η is due to the particle production in hadron collisions, which is more uniform in intervals of constant width in η than in intervals of constant width in θ.

The FCC data model for tracking closely follows conventions used in the ATLAS experiment [44]. Tracks are described in terms of the geometrical properties of an ideal helix. Definitions of the individual parameters are given in the table below. Where this approximation is not sufficient, a set of track parameters can be taken to describe a curve constructed piece-wise from helix segments.

parameter	description
d_0 [cm]	transverse impact parameter distance of closest approach to beam line
z_0 [cm]	longitudinal impact parameter, z-value at the point of closest approach to the beam line
ϕ_0 [rad]	polar direction of the track at the point of closest approach
$\cot\theta$	inverse slope of the track in the $(r$ - $z)$ plane
q/p_T [GeV^{-1}]	charge over transverse momentum

The curvature ρ is connected to the transverse momentum p_T, charge q and (assumed homogeneous) magnetic field strength B via

$$\rho[\text{cm}] = \frac{p_T[\text{GeV}]}{0.003 \cdot q[e] \cdot B[\text{T}]} \tag{4.1}$$

A direct conversion between particle three-momenta and track parameters is again possible only in an (approximately) homogeneous field and is explicitly:

$$p_x = \frac{1}{|q/p_T|} \cdot \cos\phi_0$$
$$p_y = \frac{1}{|q/p_T|} \cdot \sin\phi_0$$
$$p_z = \frac{1}{\cot\theta} \cdot \frac{1}{|q/p_T|}$$

For primary vertices the vertex parameters can be directly read off the track parameter definition. For the case of secondary vertices the event data model implementation specifies a reference surface and local coordinates to that surface.

4.3. Semiconductor Detector Working Principles

Although a multitude of different semiconductor detectors for particle radiation exist [45], the basic principle is always the creation of mobile charge carriers by ionization from a passing charged particle (see Fig. 4.2).

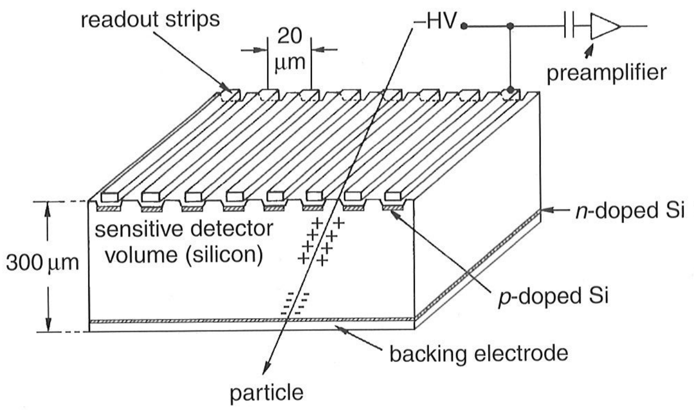

Figure 4.2. Illustration of the working principle of a silicon detector. Source: [45].

Silicon and other semiconductors used for particle detectors have some advantages over detection of radiation via ionization in gases. The band gap in silicon is small compared to the energy needed to ionize gases, thus many charge carriers are created. The sensor can be finely segmented, allowing for a very precise position measurement. They can be collected and amplified with readouts on the same module. A common configuration of sensor and readout electronics is shown in Fig. 4.3.

In software simulations of the tracker detector, such as GEANT4, only the energy deposit resulting from the particle interaction with the detector material is calculated. The digital response of the silicon detector to the passing particles needs to be simulated as well. This process, digitization, is very technology-dependent and in FCC simulation a generic, geometric approximation to this process is used.

4.3.1. Silicon Timing Detectors

Besides precise measurements of the position and deposited energy of the passing particle, silicon detectors can measure time precisely, provided an accurate clock signal is distributed. Several factors limit the possible time resolution of a silicon detector [46]. There are fundamental fluctuations in the signal amplitude which imply that a threshold voltage is reached at different times. This can be due to the shapes of the signal for varying amplitudes (*time walk*) or due to noise on the signal itself (*jitter*). In general, a thin detector is therefore advantageous for timing applications.

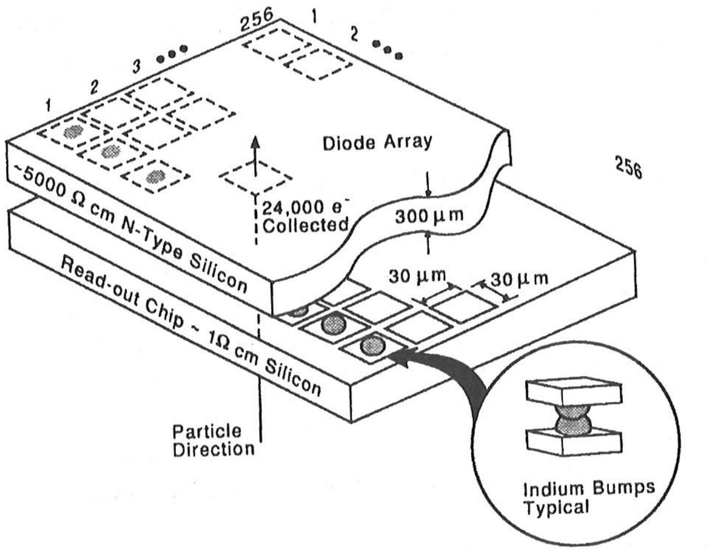

Figure 4.3. Illustration of a silicon pixel detector with bump-bonded readout. Source: [45].

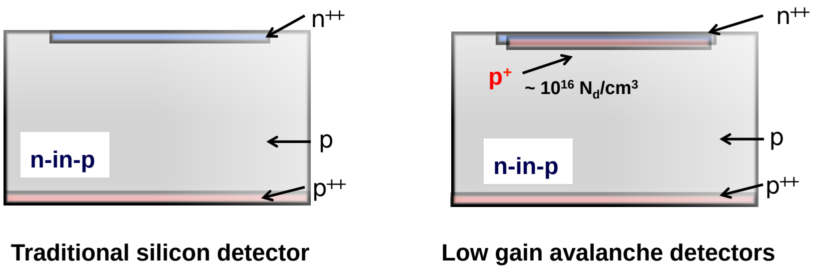

Figure 4.4. Illustration of low gain avalanche diodes for tracking. Source: [47].

Thin sensors, however, have large capacitances and require high gains for a sufficient signal, which in turns introduces noise that degrades the timing resolution.

Low Gain Avalanche Diodes

Low gain avalanche diodes (LGADs) [47, 48] have already shown in prototypes to have timing capabilities close to those assumed for timing studies at FCC-hh. They are considered to be used in upgrades for CMS and ATLAS [49, 50]. Characteristic for LGADs is a thin multiplication layer close to the junction. as shown in Fig. 4.4.

The timing resolution of LGADs is markedly worse for particles that do not traverse the amplification region around the junction. This issue, termed "LGAD fill factor

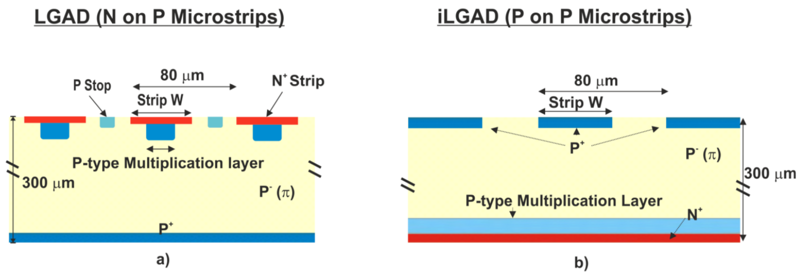

Figure 4.5. Comparison of LGADs and iLGADs. Source: [48].

problem" in the literature, leads to the study of an alternative, inverted configuration that is described in the next section.

Inverse Low Gain Avalanche Diodes

Inverse low gain avalanche diodes (iLGADs) are a variant of LGAD that promise to overcome the fill factor problem. In iLGADs, the multiplication layer is non-segmented and located at the p^+ side.

4.4. Review of Track Reconstruction Strategies

The task of offline track reconstruction is to estimate particle trajectories based on a set of measurements. The measurements of the track detector are assumed to be already in the form of partial or complete spatial information on where the interaction took place and any additional information, such as charge distributions or timing. The step of generating this information from the ionization charges collected during the interaction of the particle with the detector, in itself a reconstruction problem, is not considered here. While complex in its technical details, offline track reconstruction mostly consists of these few steps: Tracks need to be modelled, parameterized and evaluated at different points in the detector. Measurements are associated to a possible trajectory in a pattern recognition step. If this association only uses a subset of the track measurements this is known as *track seeding*. Based on a set of measurements, the parameters of the tracks are estimated in a *track fitting* step.

In the most common approach these steps are not independent and sequential. Rather an iterative procedure starting from a track seed and using estimates of the track parameters obtained by a Kalman Filter to carry out pattern recognition is used. The use of Kalman Filters in track reconstruction is thoroughly documented in the literature [51]. For reference, the relevant equations are reproduced in the notation used for FCC in the following.

In Pb-Pb collisions the ALICE experiment [52] is already faced with track densities comparable to those at FCC-hh. However, since the collision rate is significantly reduced, ALICE can use detectors like time projection chambers that would not be feasible for the planned luminosity of the FCC-hh.

4.4.1. Conformal Transforms

Some of the simplest approaches to track reconstruction belong to the family of conformal transforms. Here the hit coordinates are transformed such that the track parameters are easy to read off or calculate from the transformed coordinates. An example is the Hough transform, which is described in Ref. [17, 53] in context of track reconstruction for FCC-ee. Here transformed coordinates (u, v) are defined from (ρ, ϕ) via:

$$\rho = u \cdot \cos\phi + v \cdot \sin\phi$$

A set of points on a straight line in the (u, v) matches to a set of curves in the (ρ, ϕ) plane that intersect at a point that can be interpreted as the intercept and slope of the original line. The intersection can be easily obtained by finding the maximum of a 2D histogram, but care must be taken to choose a binning that is small enough to yield sufficient resolution, but coarse enough to group all the points from the intersection in one bin.

In order to use the Hough transform for the measurement of particle momenta, an additional conformal transformation is needed to convert circular particle trajectories into straight lines. If x, y are hit coordinates in the transverse plane, this can be achieved by calculating new coordinates u, v such that

$$u = \frac{x}{x^2 + y^2}, \quad v = \frac{y}{x^2 + y^2}$$

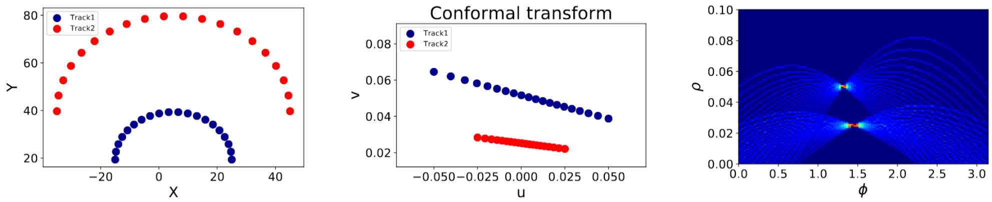

(a) (b) (c)

Figure 4.6. Example of the Hough transform of a set of hits along circular tracks. Source: [17].

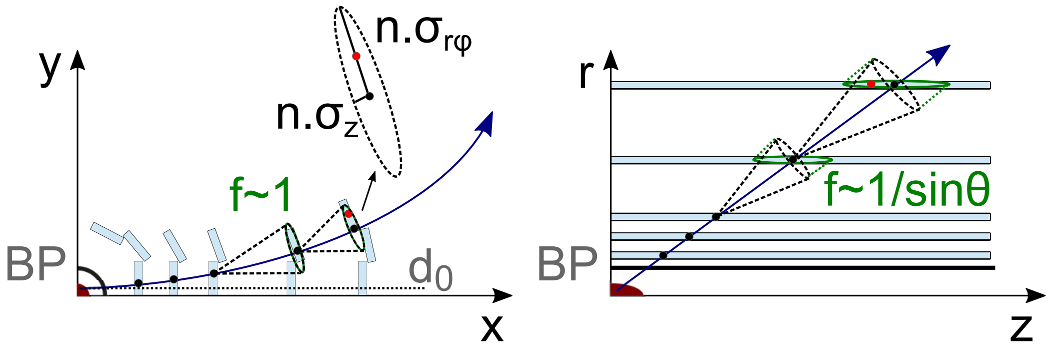

Figure 4.7. Geometric effects on the error propagation of track parameters.

After a Hough transform of (u, v), the parameter ρ can finally be interpreted as the curvature of the trajectory (and is thus indirectly proportional to the transverse momentum of the particle).

Besides its simplicity, Hough transform based reconstruction methods have the advantage that their computational complexity is linear in the number of track hits (assuming the maxima can be efficiently found). The method is limited, however, in that noise, background hits and material interactions can interfere with the identification of the maximum. It is thus best suited to the reconstruction of events with very clean tracks such as at an electron-positron collider like FCC-ee.

4.4.2. Track Extrapolation and Error Propagation

An important step in track reconstruction is the extrapolation of a track to a certain point in the detector geometry.

4.4.3. Kalman Filter

System Equation

The state vector $\mathbf{p}_k = [x_0, v]$ at surface k describes the trajectory of a particle localized in the detector. The deterministic function $\mathbf{f}_k$ (which has a linear approximation $\mathbf{F}_k$ that describes how the track parameter would change from one surface to another can be implemented. Additionally, future track parameters are affected by process noise δ_k. Usually only a subset of the track parameters is affected by process noise. This is expressed by multiplying the matrix representation of process noise with a projection matrix $\mathbf{P}_k$. The covariance matrix of δ_k is denoted $\mathbf{Q}_k$. Thus the state at surface k is given by the deterministic prediction from an earlier state and the additional process noise:

$$\mathbf{p}_k = \mathbf{f}_k\left(\mathbf{p}_{k-1}\right) + \mathbf{P}_k\delta_k$$

Measurement Equation

The deterministic function $\mathbf{h}_k$ with linear expansion $\mathbf{H}_k$ maps the track parameters $\mathbf{p}_k$ to measurable quantities (for example coordinates on a tracking module surface). The measurements $\mathbf{m}_k$ are then given by:

$$\mathbf{m}_k = \mathbf{h}_k\left(\mathbf{p}_k\right) + \epsilon_k$$

.

Prediction Equation

The essential part of the Kalman filter is the calculation of new track parameters weighted on both the prediction of the track model and previous $k-1$ measurements and the new measurement.

$$\mathbf{p}_{k|k} = \left[\mathbf{C}^{-1}_{k|k-1}\mathbf{p}_{k|k-1} + \mathbf{H}^T_k\mathbf{W}_k\mathbf{m}_k\right]$$

The updated covariance matrix $\mathbf{C}_{k|k}$ reads:

$$\mathbf{C}_{k|k} = \left[\mathbf{C}_{k|k-1}^{-1} + \mathbf{H}_k^T \mathbf{W}_k \mathbf{H}_k\right]^{-1}$$

Finally, the same weighted update can be done in a "smoothing" step to propagate the measurement information back to the first measurement.

Chapter 5.

FCC-hh Track Detector Design

This chapter describes the reference design for a track detector at FCC-hh. This concept is included in the conceptual design report and part of a complete detector concept, compatible in dimension and performance with the other subsystems.

The proposed detectors are not completely novel concepts but adaptations of the existing track detectors at LHC experiments, thus drawing on their experience. As research and development into particle detector technologies are ongoing, some technical details of the concept are expected to change until their final determination in the technical design report. The presented proposal is a proof of principle that is projected to meet the physics requirements and identifies the areas where current technology is not yet sufficient.

5.1. Introduction

Tracking detectors are optimized to achieve several, sometimes conflicting, goals, and an acceptable trade-off needs to be found for the final design. For example, pattern recognition capabilities increase with the number of detector layers, whereas the momentum resolution might decrease due to the material-induced scattering. The following sections discuss the most important design considerations.

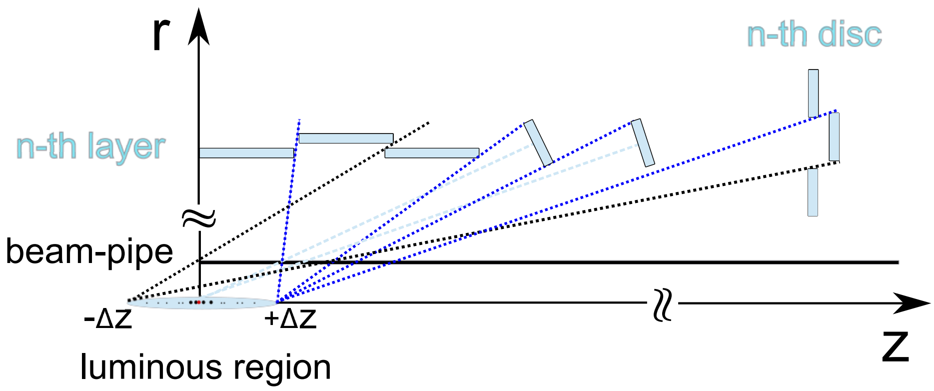

Figure 5.1. Geometric constraints for the hermeticity of a track detector. The modules must overlay enough to cover tracks from both extremes of the luminous region up to the maximum forward angle.

5.1.1. Hermeticity

As a general-purpose detector, the tracker should provide complete information on the event, measuring as many collision products as possible. Since the overall detector has to be assembled from smaller modules for practical reasons, the individual modules of the detector need to be positioned so that the chances of particles slipping through holes are minimized. The coverage in the forward region is of course always incomplete due to the beam pipe, but can be improved with detector elements close to the beam pipe at longer distances from the interaction point. The layout thus depends on the geometry of the beam spot and luminous region, as shown in Fig. 5.1.

5.1.2. Pattern Recognition Capabilities

Silicon detectors sample the particle trajectory at a limited number of points and rely on reconstruction software to give the final measurement result. The layout should therefore be well suited for the reconstruction algorithm employed, otherwise it might impose prohibitive requirements on computing power, or degrade the performance due to falsely reconstructed particles. Multiple layers close to the interaction region can for example effectively reduce the combinatorics of connecting hits to track candidates, but are counterproductive for the measurement of momentum resolution at high momenta.

5.1.3. Stability and Radiation Hardness.

As the operation time of the proposed machine is at least ten years, the detector should be optimized for stability and allow for maintenance works. The layout has to allow for a mechanical support structure to keep the detector modules in place. Although mis-alignment can be corrected for in reconstruction algorithms, movement of the modules during a run will contribute to measurement errors. Likewise, the electronics and sensor material must withstand the radiation levels of normal collider operation for the time period of operation.

5.1.4. Momentum Resolution

The lever-arm for the measurement of highly energetic particles should be as large as possible, while the magnetic field should allow for low-momentum particles to reach the inner detector. The material of the detector itself will interact with primary particles, scattering them. Therefore the detector should be as light as possible as not to perturb the measurement.

5.2. Magnetic Field

The baseline magnet concept for the FCC-hh is a solenoid, providing an approximately constant magnetic field of 4 T field strength in the central barrel volume. Fig. 5.2 shows a field map with the spatial variations of the field in the r-z plane. Two smaller solenoids create a magnetic field in the forward regions.

Earlier iterations of the design foresaw a magnetic field of 6 T, which was changed for the current design together with reduction of the detector dimensions for economic reasons.

Another version with dipole magnets providing the field in the forward regions has been studied, and curves pertaining to this magnet configuration are shown in some of the resolution plots in this chapter.

The non-uniformity of the magnetic field degrades the transverse momentum resolution in the forward region by approximately 10% according to analytical calculations [11].

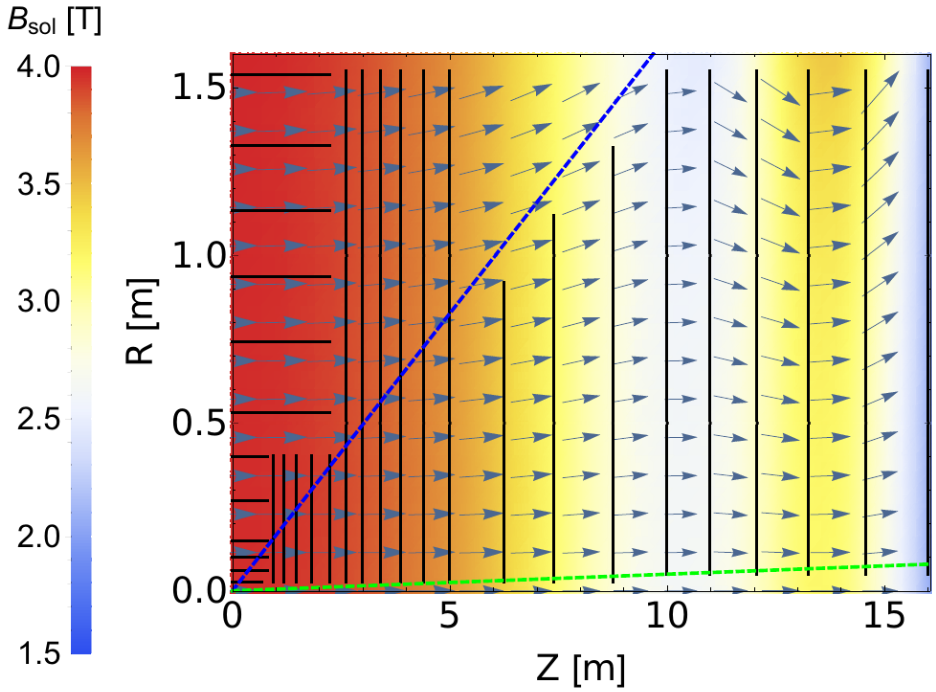

Figure 5.2. Magnetic field map in the r-z plane of the FCC-hh solenoid magnet concept. Source: [54].

5.3. Analytical Calculation of Tracker Resolutions using Glucksterns's Formulas

The tracker momentum resolution along η can be approximated by the square sum of two contributions: from detector spatial resolution that dominates at large p_{T} values, and multiple Coulomb scattering in the detector material that dominates at low p_{T} values. Both tracking limits, further denoted as 'Res' and 'MS', respectively, can be analytically assessed by the generalized Gluckstern formulae [55, 56] as:

$$\left.\frac{\delta p_{\mathrm{T}}}{p_{\mathrm{T}}}\right|_{\mathrm{Res}} = \frac{\sigma_{r\varphi}|p_T|}{0.3BL^2}\sqrt{\frac{720N^3}{(N-1)(N+1)(N+2)(N+3)}} \tag{5.1}$$

$$\left.\frac{\delta p_{\mathrm{T}}}{p_{\mathrm{T}}}\right|_{\mathrm{MS}} = \frac{13.6\,\mathrm{MeV/c}}{0.3\beta BL}\frac{N}{\sqrt{(N+1)(N-1)}}\sqrt{\frac{x_{\mathrm{tot}}}{X_0}\cosh\eta}\left[1+0.038\ln\frac{x_{\mathrm{tot}}/(N+1)}{X_0}\cosh\eta\right], \tag{5.2}$$

where p_T, $\sigma_{r\varphi}$, B, L, β and x_tot/X_0 represent the transverse momentum in [GeV/c], sensor spatial resolution in r-φ in [m], magnetic field in [T], full tracker lever-arm in [m], relativistic $\beta = v/c$ factor and total detector material budget in radiation lengths, respectively. The formulae are derived for a scenario with a constant magnetic field, and N equal and equidistantly positioned tracking layers.

5.4. Layout

Tracking detectors measure particle properties via the geometry of the particle trajectory. For any given type of individual detector capable of particle position measurements, the optimal spatial layout needs to be determined. The current FCC-hh tracker design is conservative with regards to the capabilities of the detector. The modeling and parametric simulation tool **tkLayout** [57] was used to find a design that fits the constraints imposed by the other detector subsystems and meets the performance requirements.

5.4.1. Tilted / Non-Tilted Layout

Until the end of Run-2, the large, hermetic, multi-purpose experiments at the LHC used track detectors in a "barrel/endcap" configuration. Detector modules are arranged with their sensitive areas either perpendicular (endcaps) or parallel (barrels) to the beam line.

For the upgrades undertaken during the Phase II shutdown, both experiments plan to incline certain detector modules at different angles, blurring the traditional distinction between barrel and endcap. The tilt will reduce the number of collision products that will traverse the detectors at shallow angles, and therefore the potential for scattering and interactions that degrade the momentum measurement. The drawback of the tilted configuration is the increased complexity of the mechanical support structures. While mis-alignments can be corrected to some degree during offline reconstruction, any instabilities during the run will degrade tracker performance.

The conceptual design report finally includes both a tilted (version v4.01) and a non-tilted (version v3.03) variation of the proposed layout, see Fig. 5.5.

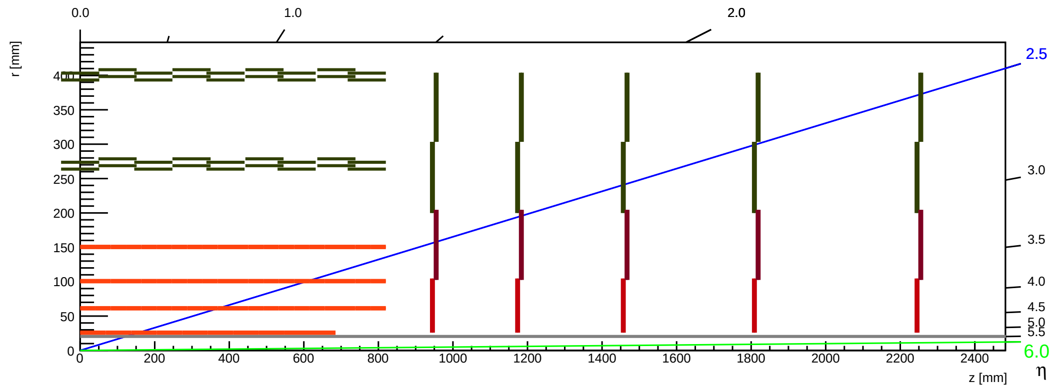

Figure 5.3. Layout of the inner tracker in the r-z plane for the non-tilted (v3.03) configuration

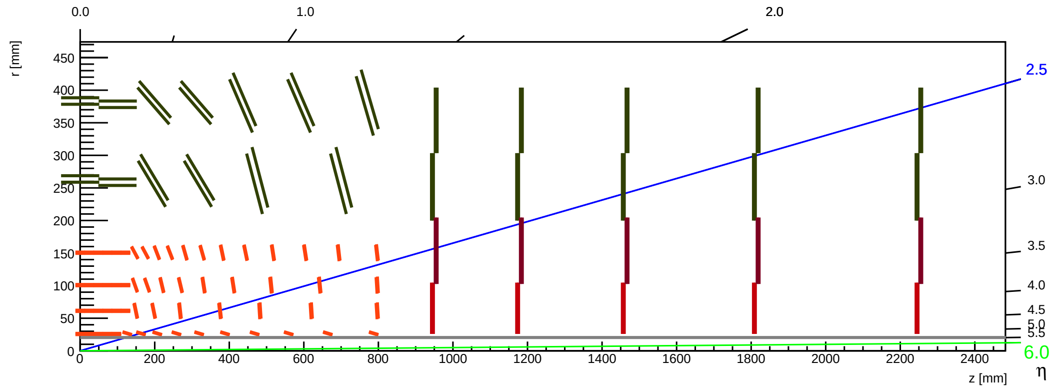

Figure 5.4. Layout of the inner tracker in the r-z plane for the tilted (v4.01) configuration.)

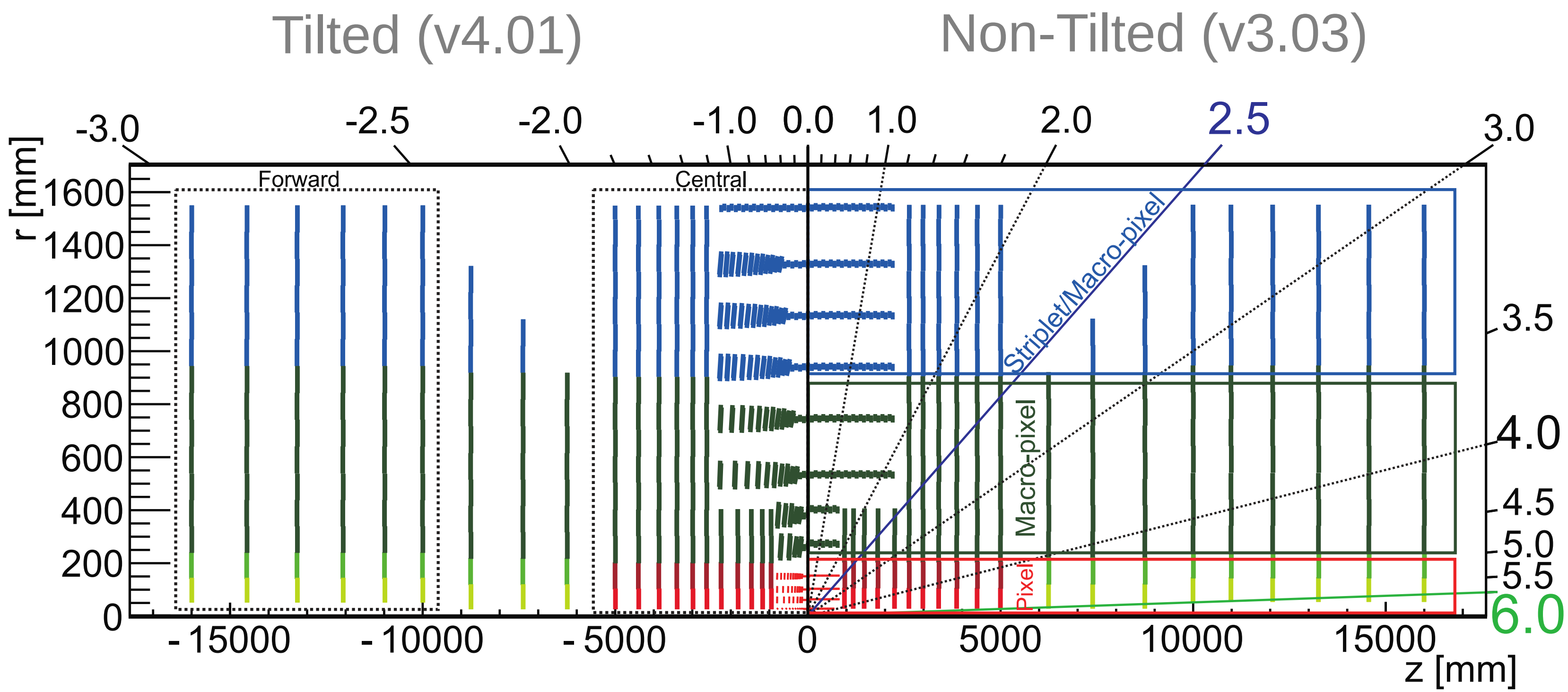

Figure 5.5. Detector Layout of the proposed FCC-hh trackers in the r-z plane. The tilted layout (v4.01) is pictured on the left, the non-tilted layout (v3.03) on the right.

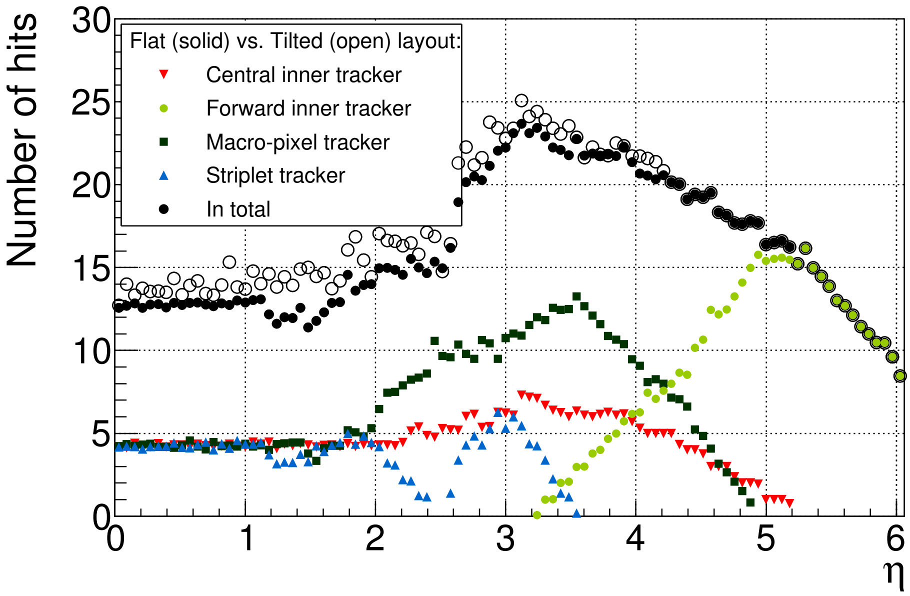

Figure 5.6. Number of hits per track in the different subsystems of the FCC-hh tracker for ideal, straight particle trajectories as a function of pseudorapidity η.

Depending on the layout, a given (charged) particle trajectory will yield a different number of measurements in the tracker. For pattern recognition and track fitting, a certain number of hits is required. As shown in Fig. 5.6, the choice of layout does not impact this metric in a significant way, and a minimum of 12 hits is expected up to $\eta = 5$.

5.4.2. Material Budget

Maximizing the number of detector layers taking measurements is ultimately defeating its own purpose, as the added material will interact with the particle, by multiple scattering, creation of delta rays, or even nuclear interactions. The particle trajectory can be changed to such a degree that the properties of the particle as it was leaving the collision can no longer be inferred from new measurements. In this sense, the detector design operates on a "material budget", measured in radiation and nuclear interaction lengths. The most important factor in this are the materials used in the construction of the detector modules themselves. Fig. 5.8 gives an overview of the thicknesses assumed in the different subdetector regions. Lightweight carbon-fibre

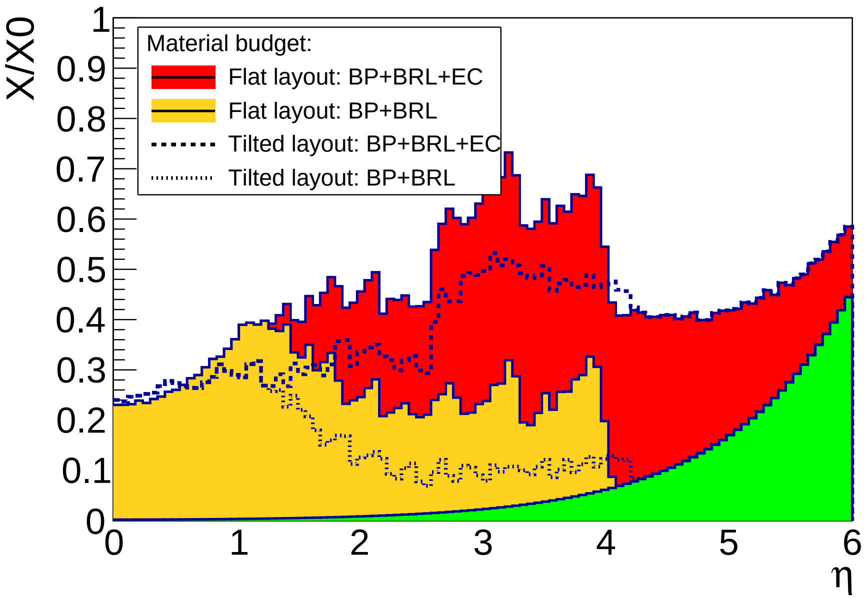

Figure 5.7. Material Budget of the flat and tilted FCC-hh tracker layouts. Each bin represents the amount of material traversed by straight, ideal particle trajectories in the given pseudo-rapidity range. The filled histograms correspond to the flat layout, with red showing the total of beam pipe (BP), barrel (BRL) and endcap (EC) trackers. The beam pipe material (shown in green) is the same for both layouts.

structures can be used in the mechanical construction of the detector. The choice of material is especially important in the inner detector, as scattering in this region will have an outsized influence on measurements at larger radii. The beampipe, which constitutes the material closest to the collision point, is designed to be constructed from Beryllium, despite its high cost, due to its light weight.

The layout can also reduce the material budget for forward tracks and is the main argument for using a tilted layout. Fig. 5.7 shows that the total material does decrease in the inclined configuration, especially in the mid-forward region between $1 < |\eta| < 4$.

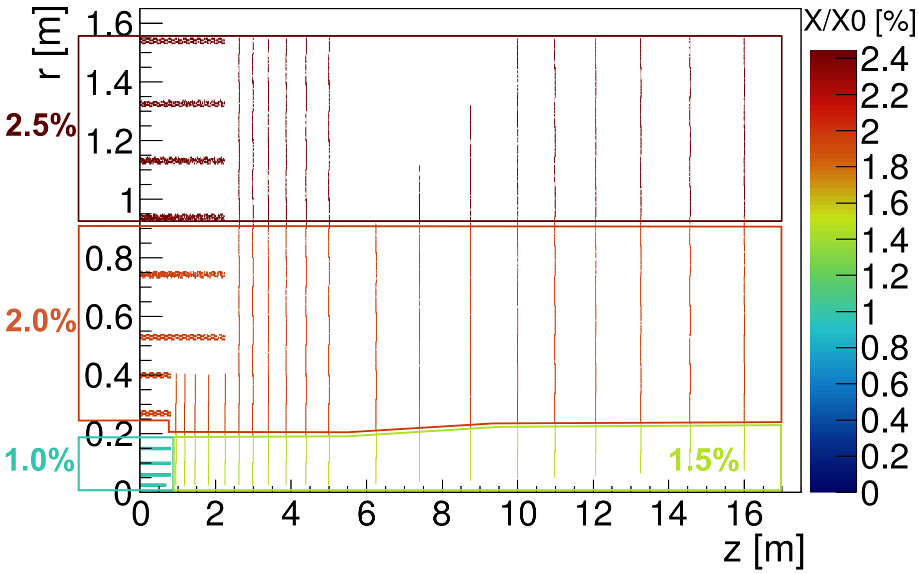

Figure 5.8. Map of the material per module in the transverse plane. Boxes indicate the regions in which each of the four different detector module types (with radiation lengths 1.0, 1.5, 2.0 and 2.5 % X_0) are used.

5.4.3. Trajectories of Low Momentum Tracks

The solenoidal magnetic field in the central detector volume forces charged particles on a helical trajectory parallel to the beam line. Charged particles below a certain transverse momentum threshold present a special case for tracking, as the magnetic field curves back the trajectory before they reach the barrel calorimeter. Without the absorbing calorimeter material in its path, the particle may traverse the light tracker material for many turns of the helix before it undergoes a destructive interaction or exits the detector volume, either entering the forward calorimeter or passing through non-instrumented regions outside of the detector acceptance.

In the case of FCC-hh, the momentum threshold for this kind of trajectories is approximately 1 GeV, as dictated by the magnetic field strength of 4 T and the tracker volume radius of 1600 mm, as shown in Fig. 5.9.

In principle (disregarding material interactions), these looping particles produce many hits and their momenta could be measured with a higher resolution than the one of particles that do not complete more than one turn of their trajectory. However this information is not of great experimental interest, as physics processes of interest

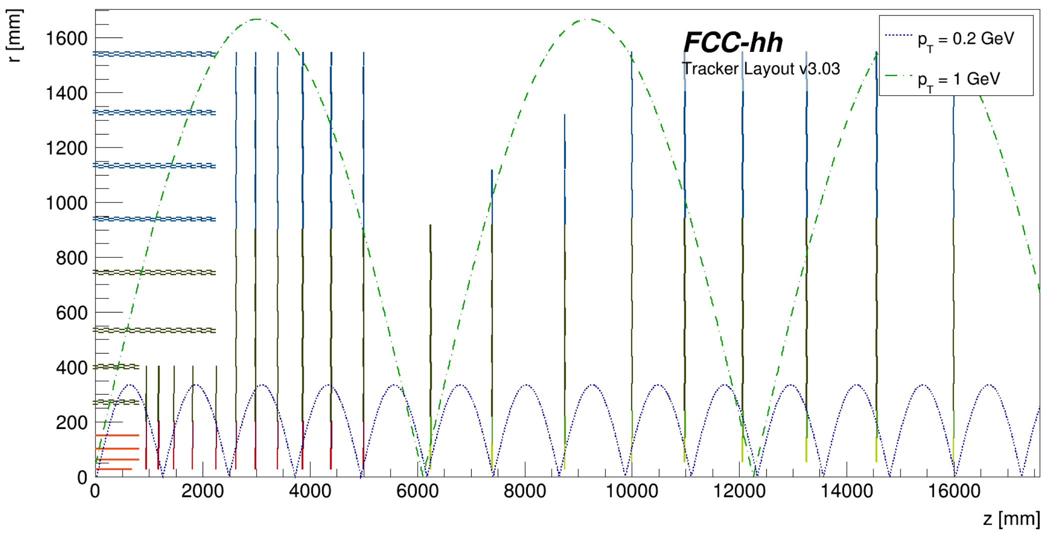

Figure 5.9. Low momentum trajectories in the FCC-hh tracker. Shown are two example trajectories with $\eta = 1$ and $p_T = 1$, 0.2 GeV respectively.

are associated with particles of higher momenta.

Furthermore, the higher channel occupancy negatively impacts track reconstruction efficiency, as the additional hits give rise to spurious track seeds. As shown in Ch. 4, the p_T spectrum in pile-up collisions is soft and has a significant fraction of low-momentum particles, which represents a further challenge pile-up poses to track reconstruction.

5.5. Detector Module Technologies

The performance of a tracking detector is a function of both its geometric configuration and the detector modules used for the position measurements. Solid state particle detectors, as described in the previous chapter, are a rapidly evolving and changing technology. The design of a experiment that will be constructed more than 20 years in the future has to acknowledge and can also benefit from these developments, but must also ensure the consistency of the design. Until the final choice is made in a technical design report, a reasonable baseline informed by current available options must be assumed to study the feasibility of the overall detector concept.

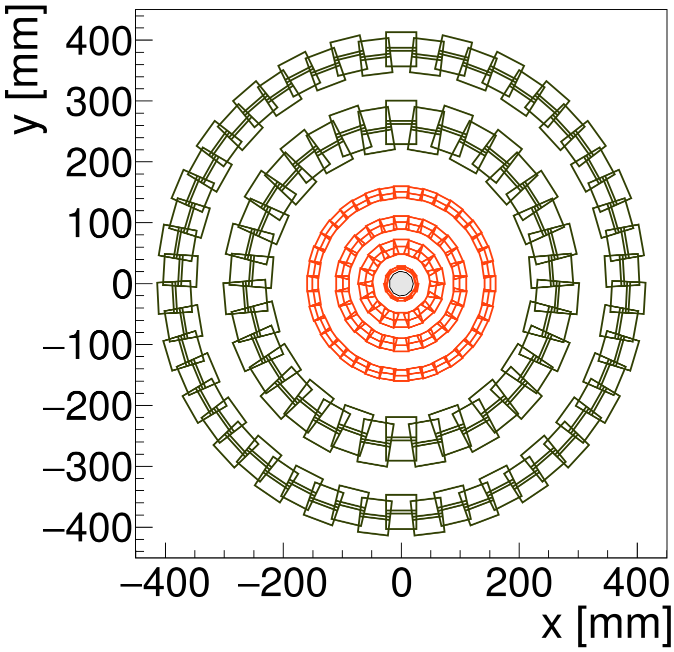

Figure 5.10. Projection of the inner FCC-hh barrel tracker layout v4.01 on the x-y plane.

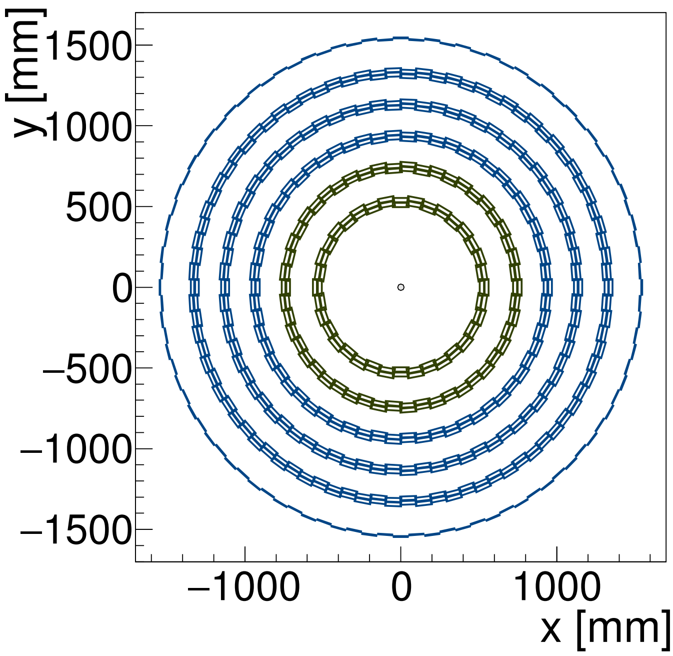

Figure 5.11. Projection of the outer FCC-hh barrel tracker layout v4.01 on the x-y plane.

In the case of the FCC-hh tracker, three types of detector modules are assumed: Pixel, Macro-Pixel and Striplet modules. Striplets effectively give only a one-dimensional position measurement and must be combined with another, rotated, striplet module to give the same information as a module segmented in pixels. Pixel modules are used for the inner barrel, and the inner rings of the endcaps. Macro-Pixels are to be used for the first four layers of the outer barrel and the rings of the endcaps up to the same radius as the fourth layer of the outer barrel. Finally the last four layers of the outer barrel and the outermost rings of the endcaps are composed of either Striplets or Macro-Pixels.

module type	resolution $r - \phi$ [μm]	resolution z [μm]	resolution t [ps]
pixel	7.5	15.0	(- / 30 / 100)
macro-pixel	9.5	115.0	(- / 30 / 100)
striplets	9.5	2887	-

The assumed module dimensions are listed in the following table. Note that there are small variations also for the same module type on different layers, which are not listed here for clarity but can be found in Ref. [58]. The relative material composition for all modules, needed for full simulations, is the same.

module type	length [mm]	width [mm]	thickness [mm]	radiation length %
pixel	68.5	12.5	1.434	1.0
macro-pixel	102.4	102.4	2.867	2.0
striplets	102.4	102.4	3.587	2.5

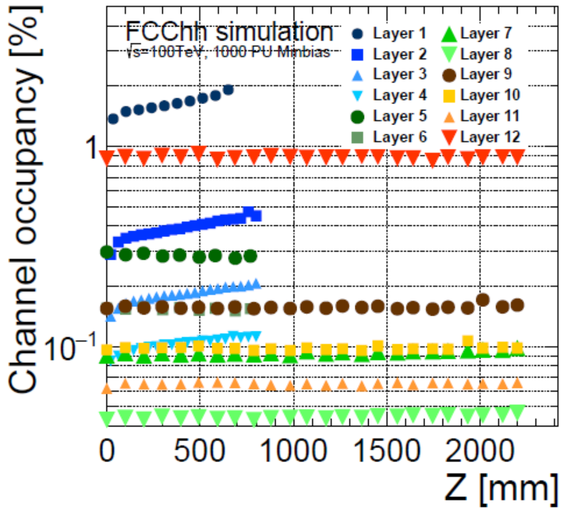

Figure 5.12. Channel occupancy in the barrel layers of the baseline FCC-hh tracker (v3.03). Source: [60].

The following table gives the composition for a pixel module. The respective values for macro-pixel and striplet modules are scaled by factors of 2 and 2.5 respectively. The silicon component includes a 0.1 mm thick layer for the sensor, as well as 0.187 mm for electronics on the module.

material	thickness [mm]
Si	0.287
Cu	0.029
Al	0.086
C	0.602
Polyethylene	0.430

The parameters are chosen to resemble those of detector modules currently under review for other projects [59]. Timing capabilities will be studied in the following chapter.

The channel occupancy of the FCC detector modules under typical high-pile-up conditions is shown in Fig. 5.12.

A more detailed study of the effects of pile-up on track hit digitization and cluster

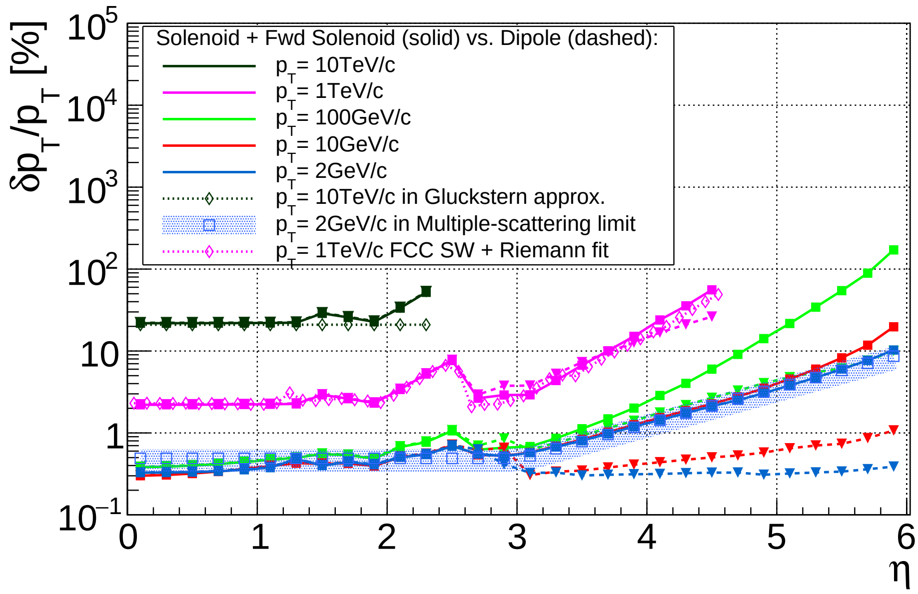

Figure 5.13. Comparison of single particle transverse momenta resolutions obtained by analytical methods and full simulation. The dotted pink line corresponds to the full simulation results. Published in [11]

sizes can be found in [61]

5.6. Momentum Resolution

The performance of the detector configuration as described in the previous chapter can be characterized both analytically and with detailed simulations. Fig. 5.13 shows that both methods agree that the required resolution for the transverse momentum, the most important direct measurement of the track detector, fulfills the physics requirements.

The resolution shows the typical direct dependence on the curvature of the track, at least for high momenta where the effect of multiple scattering is last pronounced. Below 100 GeV the material interactions offset the effect of the increased sagitta of the helix and the curves collapse. The functional dependence on the longitudinal inclination of the particle trajectory has a direct correspondence to the lever arm the tracker provides: the region between $2 < |\eta| < 2.6$ where the intermediate endcaps do not reach the full radius of 1.6 m is clearly noticeable as a deterioration of the

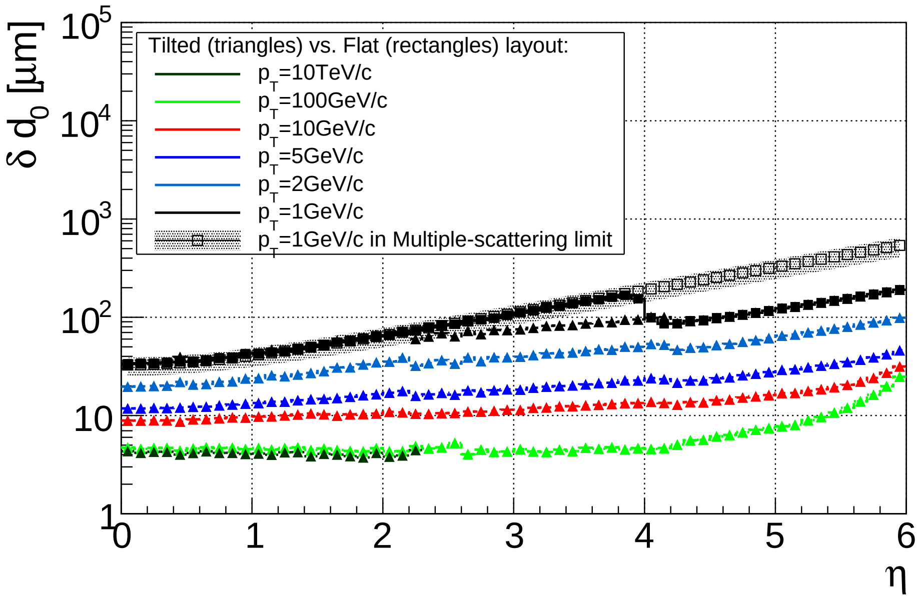

Figure 5.14. Impact parameter resolution performance of the FCC-hh tracker. To be published in [54]

momentum measurement. Trajectories with $3 < |\eta| < 6$ hit all the forward layers, but are already inclined too much to reach the outer rings, resulting in a continuously worsening momentum resolution.

The measurement of the track parameters related to the track vertex are most sensitive to the position and material of the innermost tracking layer. The resolution of the transverse impact parameter d_0 is shown in Fig. 5.14 .

5.7. Effective Pile-up

Pattern recognition capabilities are especially important for tracking detectors at the FCC-hh due to the large amount of pile-up. The requirements for a detector that allows for efficient reconstruction are different than for the most precise momentum measurement.

One way of quantifying the capability of a detector to perform in the FCC-hh environment is the effective pile-up. This measure describes the average number of pile-up vertices within the uncertainty of the reconstructed vertex position, i.e. how unambiguously a track can be assigned to a primary vertex. Fig. 5.15 shows the effective

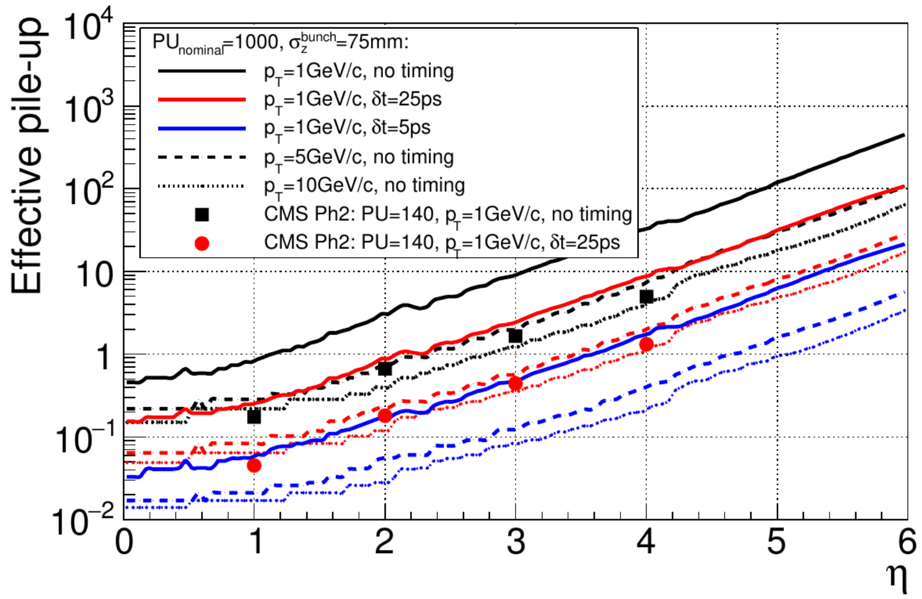

Figure 5.15. Effective pile-up in the FCC-hh tracker v3.03 (solid / dashed lines) as a function of η. For comparison, the effective pile-up in CMS is shown as well (points / squares). To be published in [54]

pile-up as calculated with the `tkLayout` software. For comparison, the performance of the CMS detector and the reduction of the effective pile-up by possible use of timing detectors are shown as well. Timing modules with 25 picoseconds time resolution would give a similar effective pile-up as CMS would experience after the upgrade to HL-LHC.

A more extreme, but technologically far more challenging timing resolution of 5 picoseconds pushes this limit even further.

Chapter 6.

FCC Software

Modern high energy physics experiments depend on software for almost all of their aspects, including detector design, data processing and analysis This chapter gives an overview of FCC software and the developments contributed during the work on this thesis. The technical aspects of the track reconstruction code used in the following chapter are then presented in more detail. A step-by-step description of the HitChainMaker algorithm that was implemented is included.

6.1. Introduction

6.1.1. Design Principles

There are several requirements that software for future colliders should fulfill:

6.1.2. Transparency and Reproducibility

Preservation of the data recorded in an experiment is a strategic goal for high-energy physics [62], as the recorded data is typically still used in studies long after data-taking is complete (p. ex., the measurement of the number of light neutrino species at LEP was updated over 30 years after it was first published [63]).

The lifetime of the software tools used to process the data can be extended by creating versioned experiment software with clearly defined dependencies and run environments.

6.1.3. Computational Efficiency

Computing costs represent a non-negligible fraction of the financial budget for modern high energy physics experiments. The ATLAS experiment uses approximately 4×10^8 CPUs for reconstruction and simulation, and the recorded data requires about 0.5 Exabyte of storage capacity [64]. This makes optimization of experiment software a necessity. However exploiting the full potential of modern CPUs requires concurrent software that can execute on several cores in parallel. Given the technological developments, multi-threading and other parallel execution models thus become especially relevant for future experiment software.

6.1.4. Interoperability

Software development is a time-intensive process that encourages re-use of existing solution in the form of software libraries. A number of high energy physics software libraries already exist, which FCC software should make use of and contribute to. Furthermore, FCC software is common to the hadronic, leptonic, and electron-hadron colliders under study.

6.1.5. Fast and Full Detector Simulation

Different levels of performance and accuracy are called for when simulating larger number detector designs. Both detailed ("full") and parametric ("fast") Monte Carlo detector simulation must therefore be part of the software.

6.2. Overview of FCC Software Components

FCC software is a set of consistent software packages (a "stack") written in C++ and Python, following best practices of high energy physics computing. The use of the LCG software releases [65] to provide the dependencies ensures that the software dependencies are transparent and readily available to users and developers. Like the LCG releases, FCC software is deployed on CVMFS [66] to make it available on all machines that provide access to CVMFS. This includes almost all HEP computing resources like the Worldwide LHC Computing Grid (WLCG) or the HTCondor cluster at CERN.

6.2.1. Software Framework: FCCSW

The central part of FCC software is `FCCSW`, an application framework that allows formulating complex simulation and reconstruction workflows, and is well adapted to be deployed on large-scale computing resources such as the WLCG or batch systems. FCCSW is based on Gaudi [67], a framework developed originally for the LHCb experiment, but which has found more widespread use in other experiments including ATLAS. Recent efforts to adapt Gaudi for concurrent data processing [68] make it a good candidate for use in FCC software.

6.2.2. Event Data Model

The computing model of Gaudi emphasizes the separation between data and "algorithms" (data processing steps within one event that can consume and create data such as event generation, detector simulation and reconstruction). In order to have consistent interfaces between algorithms, FCC software uses a dedicated event data model (FCC-EDM). This event data model is implemented using the PODIO toolkit library [69] and has been used as the format for all data in this work.

6.2.3. Generators

For FCC-hh, Pythia 8 [70] is used to simulate hard scatter events and hadronization. Gaudi components for Pythia 8, conversion to and from HepMC [71] and user-configurable single particle input to simulation have been added to FCCSW. All of these components can make use of additional tools to smear vertex positions with any given spatial and temporal distribution.

6.2.4. Simulation Libraries

In order to address the different needs within the design study, different simulation libraries are integrated as algorithms in FCCSW. Delphes [72] is used for fast, parameterized simulations of the detector response. A Delphes card parametrizing the response of FCC-hh is included with FCC software.

Geant4 is used for detailed studies of the detector response. Full detector simulation is computationally expensive, but the FCC software infrastructure allows mixing of full and fast simulation based on detector regions [73]. Further Gaudi components ("tools") allow to specify user actions, physics lists and outputs for Geant4.

6.2.5. Detector Description

All detector geometries are implemented using the detector description toolkit DD4hep [74, 75]. This allows for runtime configuration of detector parameters and interchange of detector subsystems.

6.2.6. Analysis and RDataFrame

The analysis and n-tuple production of simulated data was initially done using the Heppy framework [76], written in Python. While flexible, the performance of the Python implementation in processing the large volume of data required was problematic. With the `RDataFrame` classes, part of the ROOT library, [77] there is however a strong alternative concept that provides the performance of compiled C++ code with the flexibility of an interpreter. In order to use RDataFrame for FCC analyses, the analyzers and I/O routines of Heppy needed to be ported to C++. This effort yielded considerable speedup, as the following table shows:

Heppy CPU time [s]	RDataframe CPU time [s]	Speedup
287	6	48

6.3. Pile-up Infrastructure

Pile-up in FCC detector simulation is modeled by generating soft non-diffractive events using Pythia 8, and smearing vertex times and position according to a distribution approximating the dimensions of the luminous region.

Thus pile-up and other backgrounds can be generated and simulated as individual events, but must then be overlaid to give the full description of a bunch crossing in the detector as illustrated in Fig. 6.1 . This has the advantage that the cost of detector simulation of the high volume of pile-up events only has to be incurred once.

Similar approaches have been taken in other experiments, for example the `MarlinOverlay` package in use by CLIC/ILC [78].

In principle, the pile-up data may be overlaid after generation or simulation without loss of accuracy. After reconstruction, a parameterized smearing would be necessary to capture non-linear effects, making the program more similar to already existing fast simulation solutions such as Delphes.

The pile-up overlay, implemented in FCCSW as `PileupOverlayAlg`, accepts generated particles and vertices and simulated hits and clusters. Due to the immutable design of FCCSW data collections, new collections of merged data are created. The only complication, which also precluded a more generic implementation that would have overlayed all FCC data regardless of type, is the correct handling of relations between physics objects, e.g. the correct association of a particle to one or two vertices.

The size of minimum bias events – approximately 10^4 tracker hits on average (see Fig. 6.2) – is small enough (less than 1 GB on disk for 1000 events) to make storing a large number of simulated bias event on disk and reading them on demand more efficient than simulating the same events on the fly. Repeatedly overlaying the same minimum bias introduces biases and inaccuracies in the simulation, which can however be avoided with a sufficiently large pool. In FCCSW, the practice of randomizing the order of in which minimum bias events are read further reduces any possible bias. Running experiments have the additional option of using recorded data and overlay them on the simulation [79].

During the simulation step, the program is still linear in runtime with respect to the number of particles to be simulated. However the vertex space and time coordinates can no longer be changed. For FCC-hh, the latest parameters [31] for the machine-detector interface are implemented for use with the appropriate Gaudi component for vertex smearing. The distribution of vertex coordinates is assumed to be uncorrelated, and the number of pile-up events is assumed to follow a Poisson distribution.

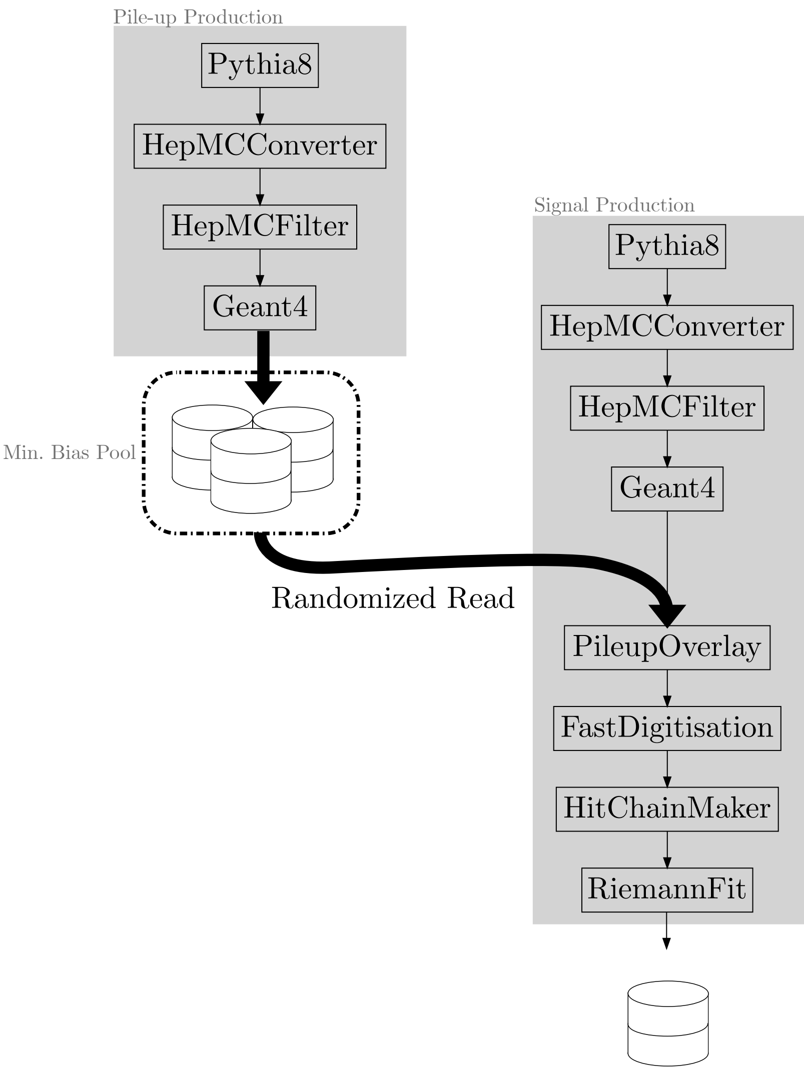

Figure 6.1. Simulation workflow that adds pile-up from a pre-simulated pool of minimum bias events. The names of the nodes refer to the Gaudi algorithms developed for simulations in FCC software.

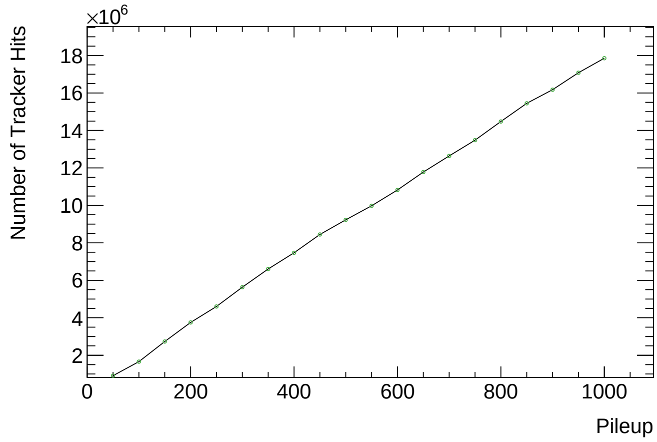

Figure 6.2. Hit collection size after the overlay of n pile-up events. Due to the large statistics even within one event with full pile-up, variations from the ideal linear behavior are small.

6.4. Integration of A Common Tracking Software (ACTS)

Like for many other areas, the FCC-hh can build on extensive tracking expertise gained at the LHC. Several differences with regards to the LHC experiments make a thorough study of the feasibility of current track reconstruction strategies necessary, but they are a natural starting point for the FCC. The application of software developed for the LHC experiments to the FCC experiments not only reflects the trend of more extensive inter-experiment collaboration on software, but is also a necessity in order to create complex software with limited resources.

As a software toolkit for tracking in high-energy physics applications, “A Common Tracking Software” (ACTS) [80] aims to modernize ATLAS tracking code while also making it more accessible to external projects. The FCC design study is the first instance of another experiment adopting ACTS outside of ATLAS. In the computing environment of FCC, a consistent software stack compatible with the dependencies of ACTS is built.

The external tracking routines are wrapped in dedicated Gaudi components. Interfaces between the FCC event data model and ACTS objects needed to be defined. Due to the track reconstruction strategy employing the iterative Kalman filter, tracks

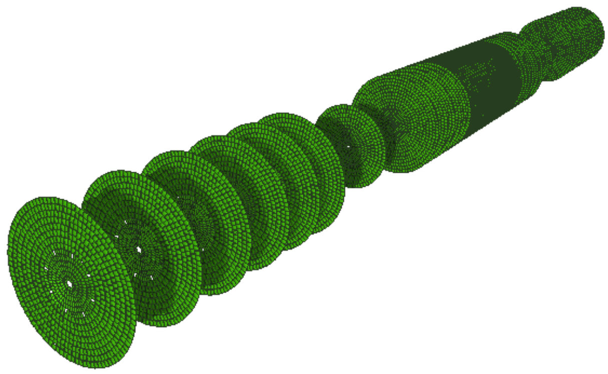

Figure 6.3. 3D visualization of the FCC tracker, as translated into the tracking geometry description of ACTS. Source: [80].

in the FCC framework are comprised of a set of track states, piece-wise continuous helix segments modeled closely on the default parameterization in ACTS. The references to tracking surfaces, which define some surface-local coordinates used in ACTS, were substituted by a space point for greater flexibility in the event data model. Even though large parts of the propagation code would need to be adapted, the internal event data model of ACTS is, in principle, flexible with regards to the number of track parameters.

The detector description toolkit DD4hep is used in FCCSW as a central source of detector information. For faster turnaround in detector design, tkLayout [81], the main tool for tracker design in FCC, was adapted to export central parameters directly to a DD4hep-readable compact file which can be used in simulation, and, via the DD4hep-plugin of ACTS, in reconstruction. Fig. 6.4 shows the agreement of the full and specialised tracking geometry. The latter is visualized in Fig. 6.3. In order to use simulated hits together with track extrapolation, the DD4hep plugin creates a mapping between DD4hep volume IDs and pointers to tracking surfaces.

Track seeding, however, is not as of yet covered by ACTS and provided for FCC by another external library, described in the next section.

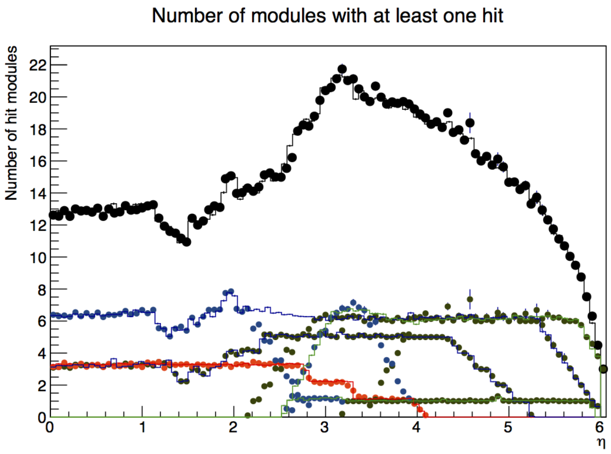

Figure 6.4. Comparison of the total number of detector hits along straight ideal tracks inside the FCC-hh track detector v3.03 as a function of the pseudorapidity of the track, calculated in tkLayout (black circles) from the original design and in ACTS (black line) from the automatically derived tracking geometry. The number of hits per subsystems are drawn in red, blue and green for inner, outer and forward tracker respectively.

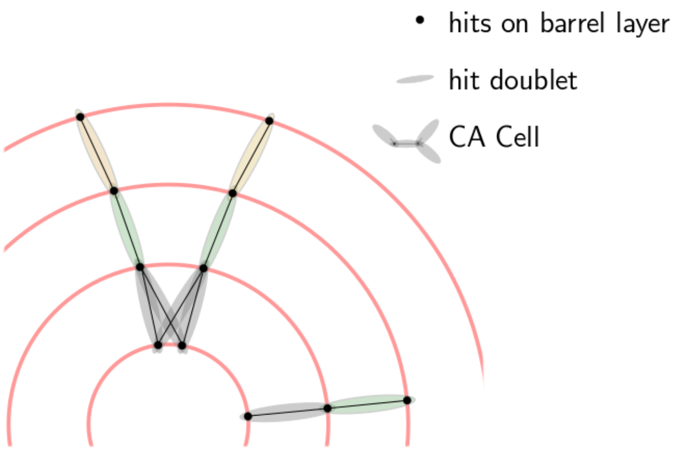

Figure 6.5. Schema of the basic concepts of the HitChainMaker algorithm. Doublets of hits (black points) are created between seeding layers (red lines).

6.5. Track Seeding Using Cellular Automata

The basic concepts of the HitChainMaker algorithm that is at the core of the Trick-Track library [82] are illustrated in Fig. 6.5. Its usage for the CMS experiment is described in detail in reference [83].

6.5.1. Description of the HitChainMaker Algorithm

The HitChainMaker (HCM) algorithm consists of the following steps:

1. [Input and Output]. The input to the algorithm is a set of data points H consisting of measurements from the track detector (Hits), the output is a set of subsets of those points (Track Seeds). The hits in each of these subsets are part of a track candidate.
2. [Group in Layers]. Partition the set H into layers, so that two hits in the same partition are unlikely to belong to the same track. This reflects the physical layout of the tracking detector, which usually has a layered structure.
3. [Layer Graph]. Construct a directed graph with the layers as nodes and the possible paths a track could take as edges. If the layers are hermetic, there should only be nodes between neighboring layers. If there is a possibility that hits are missing on any one layer, there should be edges to the next-neighbors as well.
4. [Doublet Creation]. On every edge of the layer graph, create all pairs of one hit on the inner and one hit on the outer layers that pass the doublet filter.
5. [Cell Creation and Connection]. For each doublet, create a cell. The cell consists of the addresses of the inner and outer hit forming the doublet, a list of addresses of cells that share the inner or the outer hit with this cell (the inner and outer neighbors), and an integer counter representing the state of the cell, initially set to zero. Each cell is also associated to an edge in the layer graph.
6. [Cellular Automaton Update]. Starting from the root node(s) of the graph, increment the state of each cell if its state was equal to the state of one if its inner neighbors, provided it has at least one inner neighbor. Repeat N times.

7. [Collection of Track Seeds]. Create Trackseeds for each connected set of cells with length N.

The detector topology is described by a graph of connected tracking layers. Information on the exact detector geometry only enters via the hit position, eliminating the need for a detailed geometry description for any experiment that measures three dimensional space points. The cells acted on by the algorithm are formed by doublets of hits on neighboring layers and connections between doublets sharing one hit. The number of possible track candidates is limited both in the doublet creation step and while connecting the cells, taking advantage of the geometrical constraints on physical tracks originating from the interaction region. The default geometric filters included in the libraries will be useful for most cylindrical detector geometries. Still, this filtering step is easily extensible and adaptable as any classifier for two and three hits can be used in conjunction with `TrickTrack`. To extract tracklets of length n from the connected cells, the `HitChainMaker` performs n evolutions of a cellular automaton, incrementing the state of each cell with same-state inner neighbors. A depth-first search starting from cells whose state equals n then yields all possible track candidates.

6.6. Computational Performance of the HitChainMaker Algorithm

The performance of reconstruction software is intertwined with the detector designs and requirements. Nevertheless it is possible to reframe some steps of the reconstruction program in terms of simple data structures and geometric quantities.

Relying almost exclusively on local operations on doublets and triplets of hits, the `HitChainMaker` algorithm is parallelizable and adaptable to multi-core computing hardware. However, the computing performance is still dominated by the classifier used to suppress fake tracks, which will be discussed in Ch. 7. As a check of the efficiency of the implementation itself, Fig. 6.6 shows the pure computing performance for varying fake rates at constant input size (or equivalently varying input size at constant fake rate).

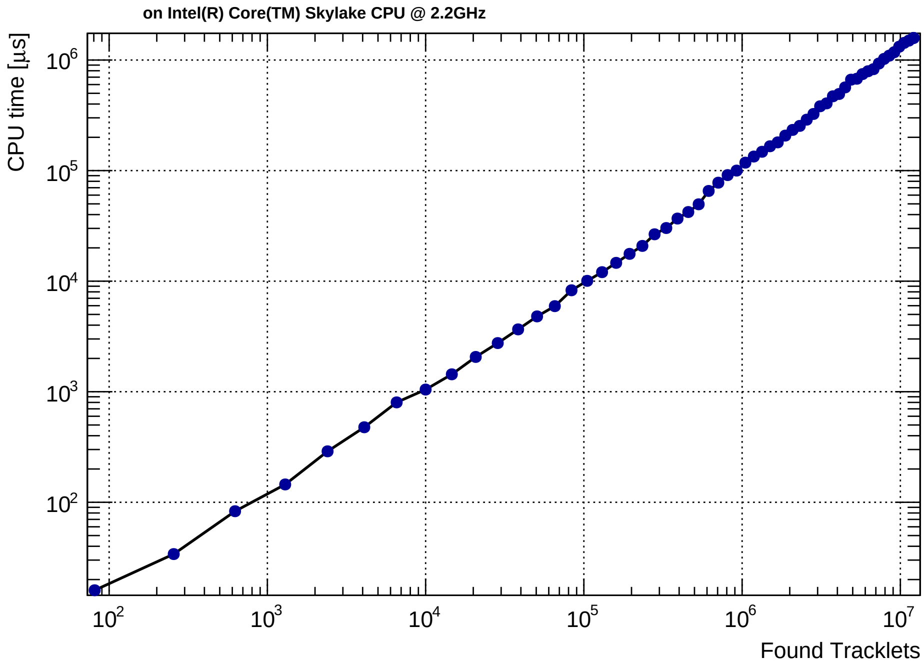

Figure 6.6. CPU time of `HitChainMaker` execution for a generic tracker as a function of the result vector size. The use of the result vector size as variable eliminates the dependency of the runtime on the efficiency filters.

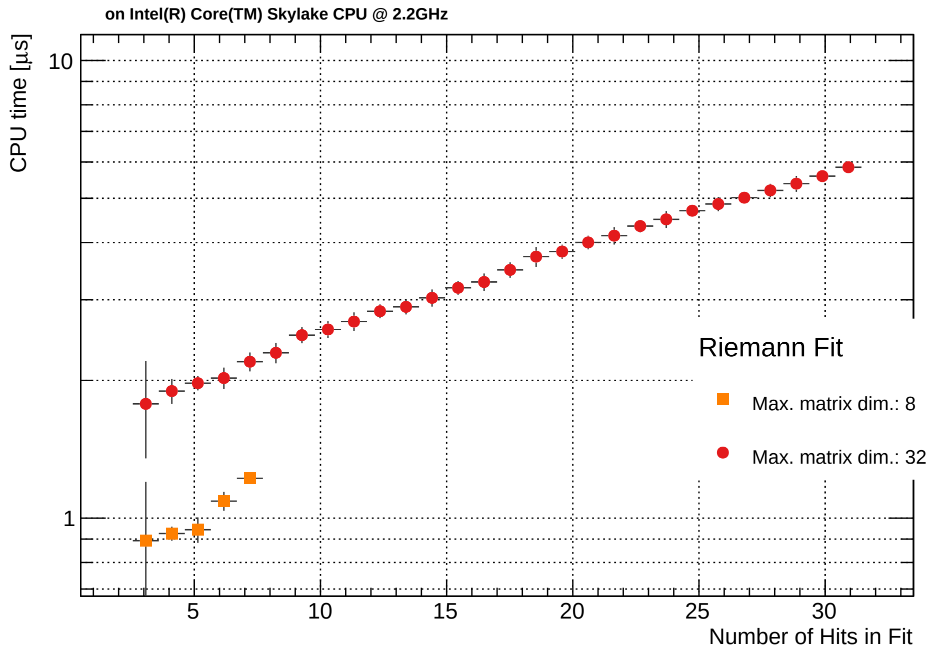

Figure 6.7. CPU time of the Riemann fit routine as a function of matrix size.

Since it relates the runtime to the output size of the program (i.e. the number of found track seeds, as opposed to the input size, which would be the number of track hits), the linear behavior of the performance in Fig. 6.6 does not mean that the complexity of the algorithm is linear. However, it does indicate that there are no undue inefficiencies in the implementations, which would present themselves as non-linearities in the scaling of the runtime with found track seeds.

6.6.1. Riemann Fit on Track Seeds

To fit the five track parameters to track seeds, an implementation of the Riemann fit [84] is employed. This method is fast, but limited to homogeneous fields, which does not subtract from its usefulness for seeding in the inner tracker.

Fig. 6.7 shows the execution time of one fit as a function of the number of points to fit. Due to the use of fixed size matrices of the hit coordinates, limiting the maximum number of points to fit can have a noticeable impact on performance. The Riemann fit can thus be used to fit a large number of track candidates consisting of four hits.

6.6.2. Use of KDTrees for Doublet Creation

The data structure used to store and manipulate hit data can have a significant impact on the overall tracking performance. Especially at large scales such as full pile-up events at FCC-hh the use of data structures that are well adapted to the memory model is a requirement.

In the case of track seeding, one operation that must be optimized is the creation of doublets. This involves the look-up and filtering of hits by coordinates, as they must be compatible with certain geometric constraints. Thus for each hit on the inner layer all hits on the outer layer are examined and checked by the geometric classifier. If it rules them compatible, a doublet is created for these two hits and processing continues with the next hit.

The most straightforward illustration would consider each combination of hits on two layers by means of a nested loop over two hit containers. A more sophisticated alternative is the use of a K-Dimensional Tree (KDTree) with K = 2, 3 or 4 depending on the dimensionality of the available hit information. This classic data structure can be thought of as a binary search tree with multiple levels that partition different dimensions at each level, as illustrated in Fig. 6.8 with the coordinates RPhi, T and Z that are used for seeding in FCC-hh.

The performance profile, measured in term of the CPU time needed to create doublets from a certain number of hits, is shown in Fig. 6.9. Although the speedup is evident, this implementation will yield the same number of doublets and will not decrease the number of fake seeds, which are the bottleneck in the reconstruction. Nevertheless, Fig. 6.9 shows that an efficient implementation of track reconstruction for the FCC-hh can benefit from of the KDTree.

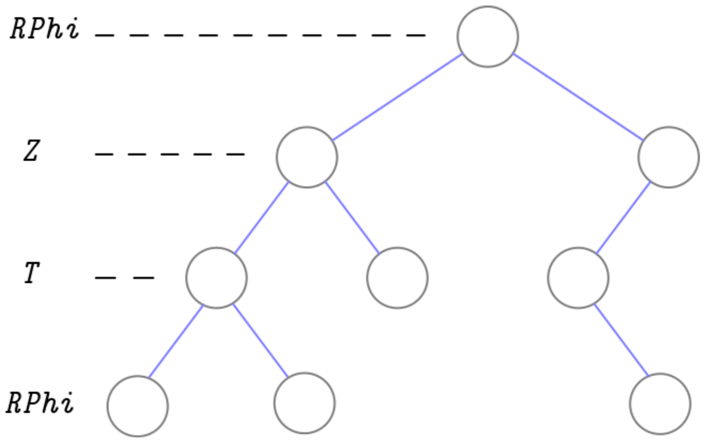

Figure 6.8. Schema of the KDTree data structure as used for FCC-hh. Each hit is stored as a node in the tree, and each plane introduces a splitting in a different variable, so that all hits with an RPhi greater than that of the hit represented by the top node are stored in the right subtree and all hits with a smaller RPhi in the left subtree.

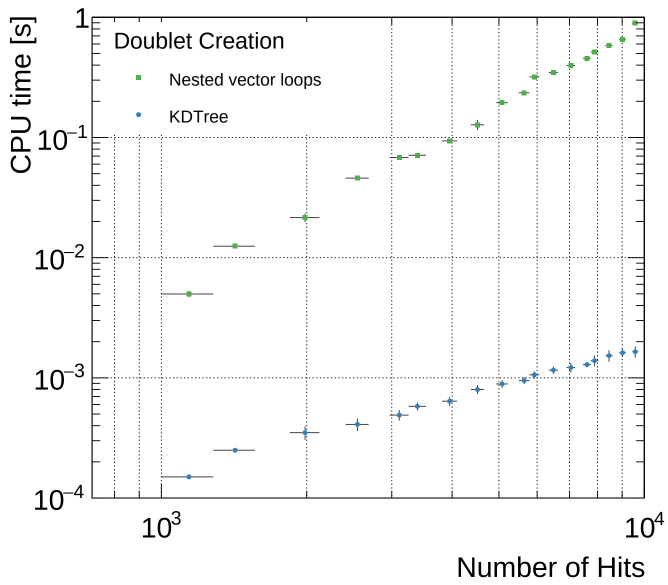

Figure 6.9. Impact of data structures on doublet creation performance. The execution time of the doublet creation routine is plotted versus the number on hits on each of the seeding layers. For this benchmark, an equal number of hits has been distributed randomly on the two seeding layers. Shown in green is the naive implementation of nested loops, blue points represent the identical program implemented using a KDTree data structure to select the second hits.

Chapter 7.

Timed Track Seeding: Performance Results for FCC-hh

The overall momentum resolution and other performance characteristics of the reference tracking detector have been established in Ch. 5. This chapter contains the results of a simulation study of track seeding with timing detectors at FCC-hh.

7.1. Introduction

In collider experiments, the computing performance of the reconstruction software is not typically a design requirement of the detector. Computing hardware and software develop at a rapid pace and capacities can usually be increased as the need arises. For FCC-hh, however, this will no longer be true: The stark increase in pile-up comes with a combinatorial increase in the need for computing resources, which cannot easily be compensated with larger computing infrastructures alone. Furthermore, current trends in computing hardware tend towards more concurrent computing, such as increased number of CPU cores, not increased clock speeds. The full potential of these resources can only be exploited with multithreaded applications, which requires developments of dedicated reconstruction software.

The performance of a detector and the corresponding reconstruction algorithm has several aspects: It has to be efficient, i.e. reconstruct a sufficient fraction of the particles and maintain a low rate of false positives ("fakes"). The measurements of particle momenta and relevant other quantities must be precise and have low uncertainties. A final aspect of performance is the resource utilization of the reconstruction algorithm, including CPU time and memory usage of the program. In off-line reconstruction applications, the throughput, i.e. how many events can be processed per unit of time with given resources, is the most important characteristic. In other applications, for example in reconstruction routines used for triggering, the latency, i.e. the time needed to process one event is the first performance metric. The optimal detector design is an appropriate trade-off between these distinct requirements .

The computational efficiency of the `TrickTrack` implementation of the HitChainMaker algorithm has been investigated in Ch. 6.6. Here, the software is applied to the problem of reconstructing single particles in the high pile-up setting of FCC-hh.

7.2. Methods

Simulated data is used to estimate the performance of the FCC-hh track detector concept. The software for this study is now part of the FCC software framework, for which a more detailed description can be found in Ch. 6. The detector simulation is carried out using the Geant4 toolkit [85] as integrated in the FCC software framework, using the DD4hep [74] model of the tracker geometry with the layout v3.03 [58]. The `FTFP_BERT` physics list of Geant4 is used for the interaction of particles with matter. Minimum bias events were generated with Pythia 8 [33] and overlayed in the FCC software framework to form the pile-up background. The magnetic field is taken to be a homogeneous solenoidal field of 4 T throughout the tracker volume, and the actual seeding is performed using the HitChainMaker algorithm implemented in the TrickTrack library.

7.2.1. Seeding Parameters and Variations

Track seeds are reconstructed from simulated hits on the seeding layers of the tracker, which are formed by the inner barrel and endcap tracker. Here, for simplicity, only the four innermost barrel layers are considered.

The track seeding step of the reconstruction program can limit the number of fake

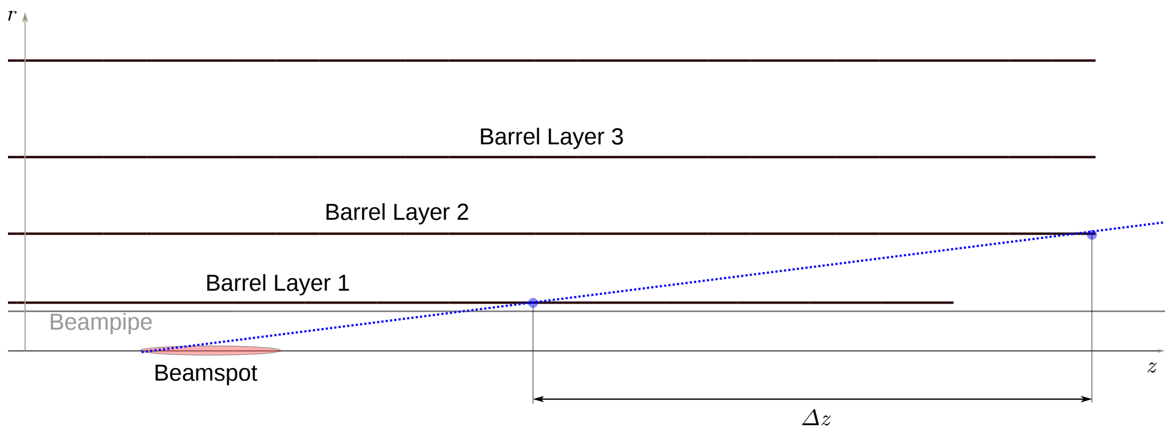

Figure 7.1. Definition of the coordinate Δz of the hit doublet formed from two hits on neighboring layers.

seeds in two stages: During the construction of hit doublets, the coordinates of the hit pairs can be used to reject the given pair. At this step, only the differences $\Delta\phi$ and Δz in azimuthal and longitudinal hit coordinates are used.

The radial coordinate is fixed by the detector geometry (for a barrel layer; in case of an endcap layer the radial coordinate can vary and the longitudinal coordinate is fixed). The difference in hit timing Δt is used here to mitigate pile-up in the FCC-hh tracker. The filter itself is a simple cut-off on the coordinate differences: The difference $\Delta\phi$ in azimuthal angle will tend to zero for high-energy tracks and thus has to be chosen to allow a certain minimum transverse momentum to pass. The difference Δz in the longitudinal hit coordinate depends on the detector geometry and track inclination. Care must be taken not to exclude forward particles.

Once hit doublets between all seeding layers are formed, the HitChainMaker connects doublets on neighboring layers sharing a middle hit, forming hit triplets. Again filters can be applied to immediately reject track seeds. With three hits available to provide information, more complex filters can be used. In this study, two geometric filters were used as in CMS [83]. First, a circle is constructed from the projection of the hits in the transverse plane (see Fig. 7.2). The curvature of the circle and whether it intersects the luminous region are then used as criteria to discriminate fake seeds.

Second, the alignment of the hits in the longitudinal direction is used as a criterion for straight tracks (Fig. 7.3).

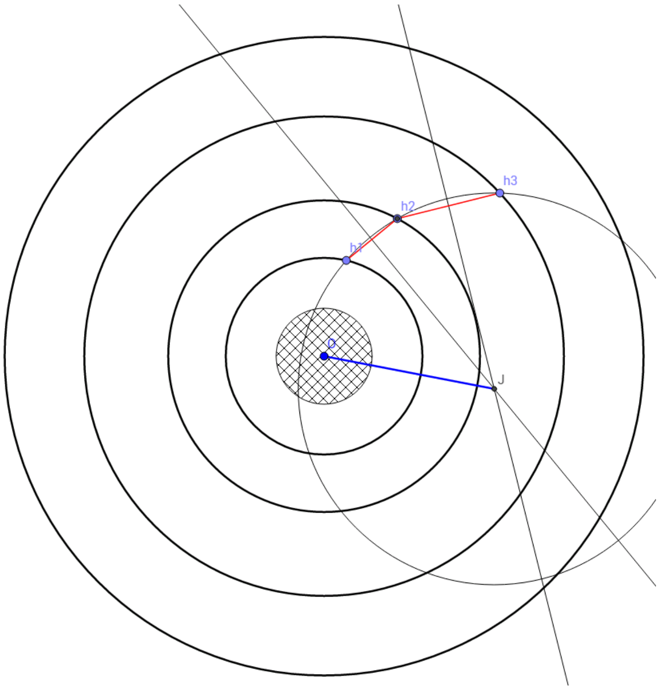

Figure 7.2. Geometry of the triplet curvature and intersection filter. The radius of the circle formed by hits h1, h2 and h3 as well as the intersection with the luminous region (marked as a cross-hatched area) is checked. Source: [83].

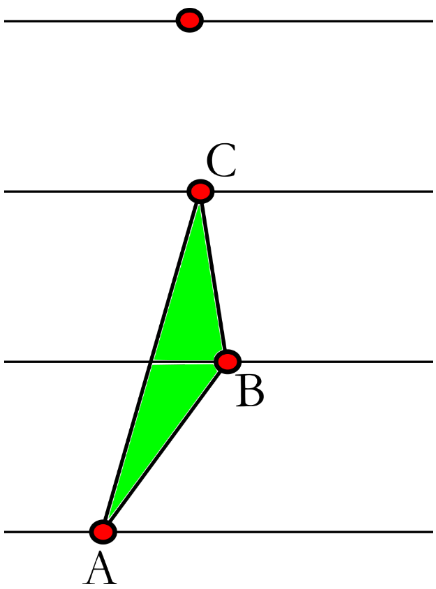

Figure 7.3. Geometry of the triplet alignment filter. The area of the green triangle composed of the hit triplet A, B, C is compared against the parameter `thetaCut`. Source: [83].

Finally, the timing information can be used to select hits that align also in the temporal plane.

The parameters used in the configuration of the seeding are listed in the following table:

Parameter	TRKCFGStrict	TRKCFGBaseline	TRKCFGLoose
`phiCut` [rad]	4.0	2.0	1.0
`ptMin` [GeV]	2.0	1.0	0.5
`region_origin_radius` [mm]	0.004	0.002	0.001
`hardPtCut` [GeV]	12.0	6.0	3.0
`thetaCut` [rad]	0.8	0.4	0.2
`timingCut` [ps]	5	30	100

Apart from the baseline configuration `TRKCFGBaseline`, which is very close to the one used for track reconstruction in CMS, the calculations have been repeated with two variations, `TRKCFGLoose` and `TRKCFGStrict`. This is done in order to gauge the influence of these geometric variables. `TRKCFGLoose` is a variation of the baseline that relaxes all filtering criteria, resulting in an increased acceptance but also an increased fake rate. The parameter `ptMin` has a direct correspondence to the minimum transverse momentum of a particle (in GeV) that would create a track seed.

7.2.2. Time-of-Flight Corrections

The time of flight between layers is of the order of a few nanoseconds, and can thus be large compared with the time differences between pile-up and signal collisions (up to several hundred picoseconds). In order to facilitate the use timing measurements to reduce the fake rate the time of flight between tracking layers is corrected for, so that cuts can be applied directly on the corrected time coordinate. This is done via the position information associated with the hits. The pathlength divided by the speed of light is subtracted from time difference to yield the corrected time difference Δt_{corr}. Barring deviations from the ideal, straight line trajectory this results in a corrected time difference that is close to zero for hits along the same track and can be used for filtering. The distribution of uncorrected and corrected time differences is shown in Fig. 7.4.

7.3. Results

7.3.1. Efficiency of Purely Geometric Track Seeding

The impact on tracking efficiency of filters composed of cuts on the various seeding parameters are shown in Fig. 7.5 and Fig. 7.6. Fig. 7.7 offers more detail on p_t-η correlations of inefficiencies.

It is important to note that the result validates the assumed performance used in the parametrization of the detector performance in the Delphes fast simulation.

7.3.2. Filtering Potential of Doublet Variables

The cellular automaton described in the last chapter operates on doublets, pairs of hits on neighboring detector layers. Fig. 7.8 shows $\Delta\phi$ as well as the difference in longitudinal coordinate Δz and difference in temporal coordinate Δt, further features that can be used in the efficient creation of doublets. The distributions are plotted both for the random combinations of pile-up hit coordinates as well as for physical tracks. These are very broadly defined as the trajectories of any particles that fall within the design acceptance of -6 $< \eta <$ 6, originate in the luminous region and

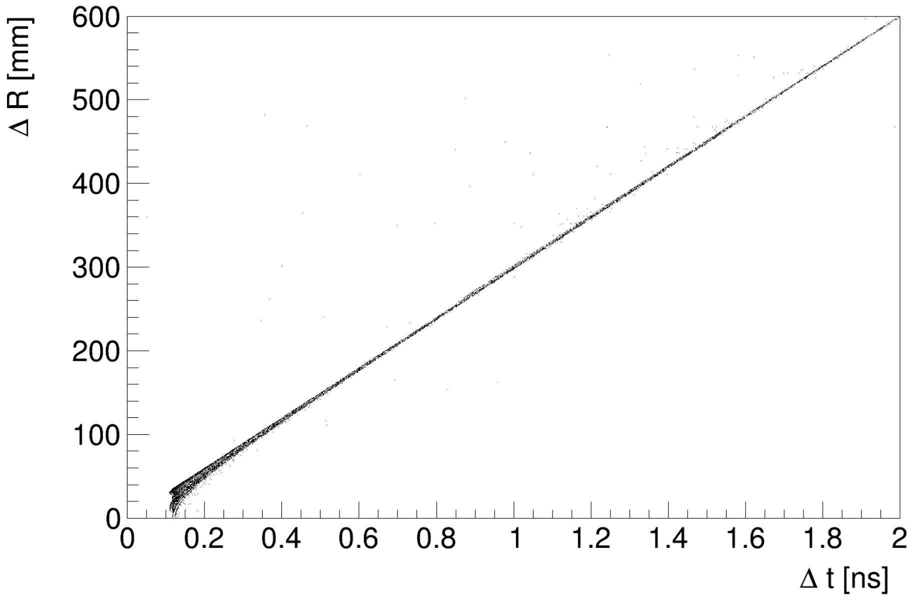

(a)

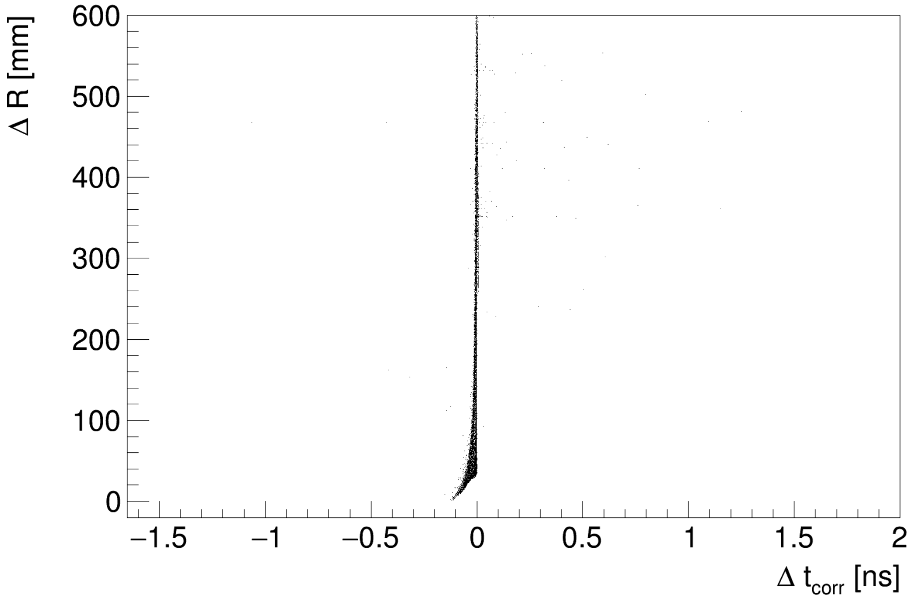

(b)

Figure 7.4. Scatter plots of the difference in path length ΔR of hit doublets versus their difference in time coordinate Δt. Fig. (a) shows the absolute time difference between two hits belonging to single muons, Fig. (b) shows the difference in the time-of-flight corrected coordinate Δt_{corr}, where the influence of the trajectory on the time difference is almost negligible - the time differences reflect ideally only the different collision times.

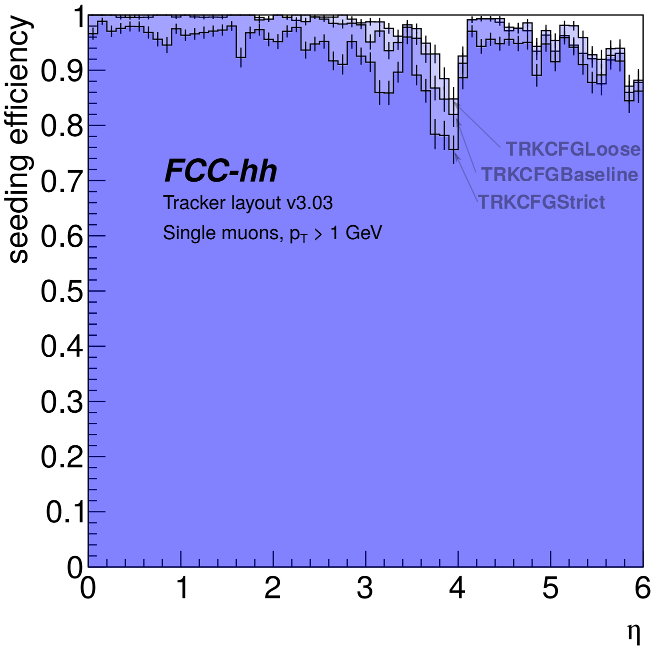

Figure 7.5. Single particle tracking efficiencies as a function of pseudorapidity η. The baseline configuration of the track seeding algorithm is shown along a more exclusive and a more inclusive variant (see text for details).

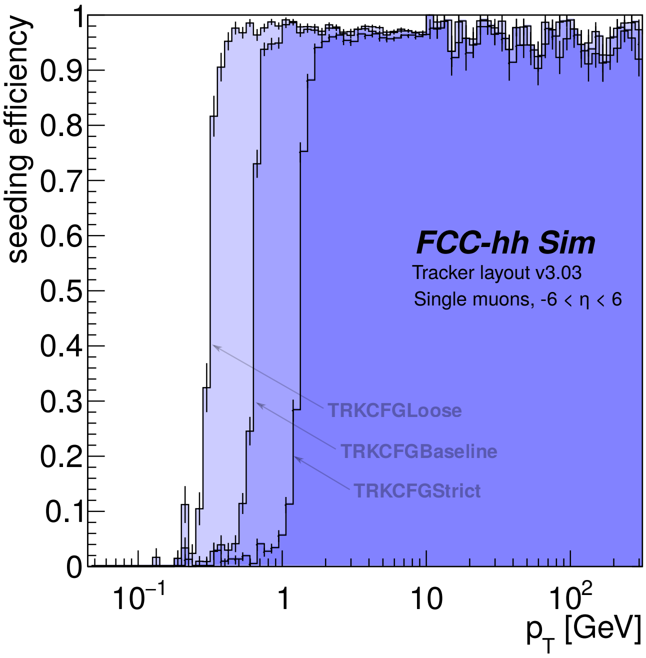

Figure 7.6. Single particle tracking efficiencies as a function of transverse momentum p_t. The baseline configuration of the track seeding algorithm is shown along a more exclusive and a more inclusive variant (see text for details).

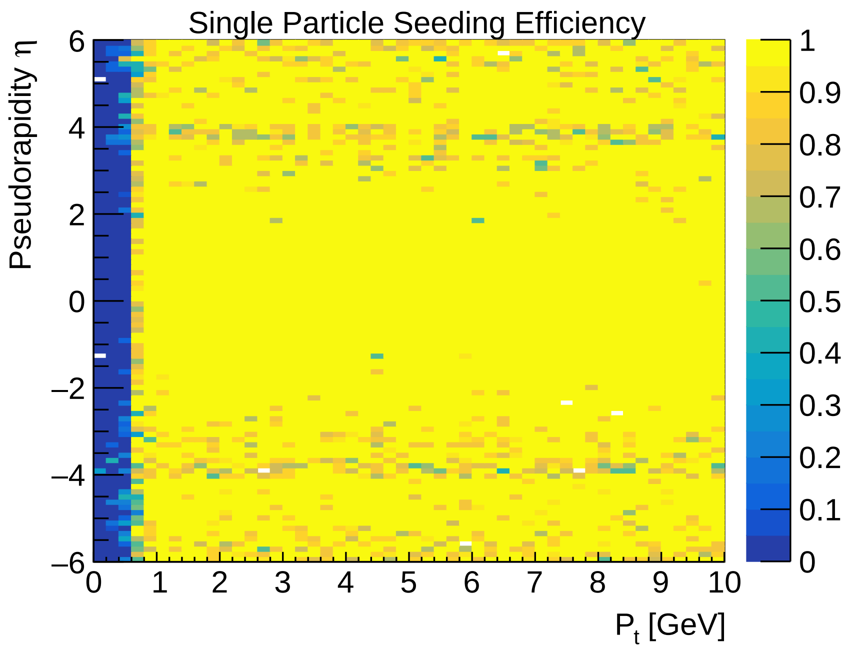

Figure 7.7. 2D Graph of seeding efficiencies as a function of both transverse momentum p_t and pseudorapidity η in the FCC-hh tracker v3.03. A noticeable efficiency drop around $\eta = 4$ is present for all momenta.

possess a transverse momentum $p_t > 0.5$ GeV.

In Fig. 7.11, another parameter is used to filter fake seeds: the curvature of a hit triplet in the transverse plane. It is apparent that the curvature correlates with the transverse momentum, but also that any cut on this parameter will lose some tracks that are strongly curved.

7.3.3. Displaced Vertices

Displaced vertices are of interest to some physics searches, notably searches for long-lived particles [86]. Fig. 7.12 shows the acceptance of displaced vertices and confirms that they can be reconstructed as long as they are within four seeding layers of the tracker.

7.3.4. Comparison of Fake Rate with Timed and Geometric Filters

Fig. 7.13 examines the baseline configuration and shows the scaling of the number of fake doublets with increasing pile-up. Timing capabilities are added here to show a significant reduction in the number of fake doublets. The effect of timing resolution is detailed in Fig. 7.14, which measures the same quantity as a function of the possible cut on T.

7.3.5. Efficiency of Timed Seed Filters

The additional timing cuts should ideally not decrease tracking efficiency. Fig. 7.15 shows that the efficiency is unaffected for timing cuts down to 30 ps. Below this value, the efficiency decreases significantly, as seen in the curve for timing cuts of 10 ps.

7.4. Discussion

Like any classifier, the filters presented in this chapter must balance the rate of false negatives and false positives. In this case, the track seeding package was written with the aim of approximately reproducing the efficiencies used to parameterize the

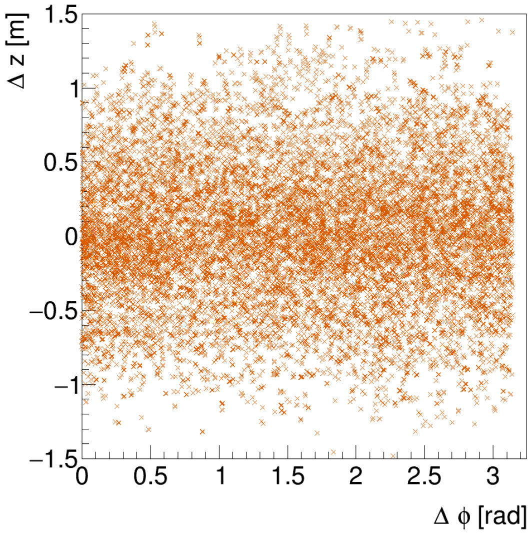

(a)

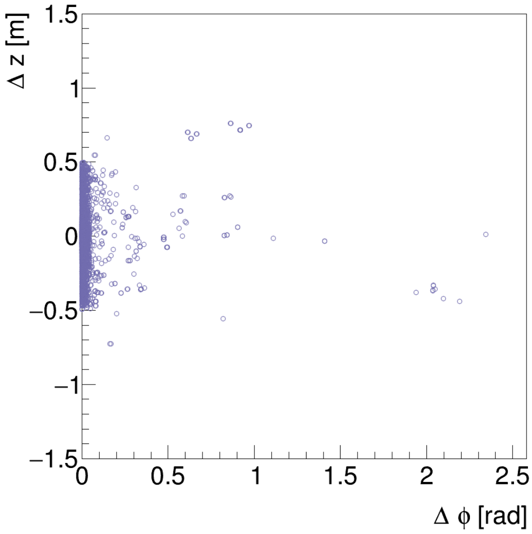

(b)

Figure 7.8. Scatter matrix plot for the doublet coordinates Δz and $\Delta\phi$. These coordinates are essentially uncorrelated, as expected for an isotropic particle source.

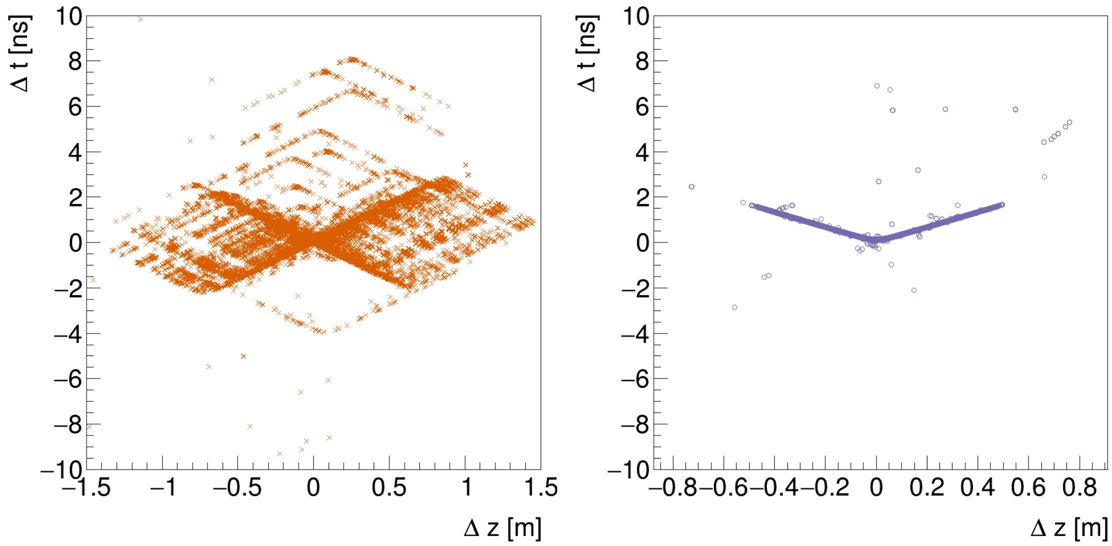

(a) **(b)**

Figure 7.9. Scatter matrix plot for the doublet coordinates Δz and Δt A strong correlation reflects the time-of-flight component of the hit time information. The doublets from the pile-up hit combinations may also feature inner hits with later timing than the outer hit (as they originate from different collisions) thus the slope of the correlation is also seen mirrored and moved.

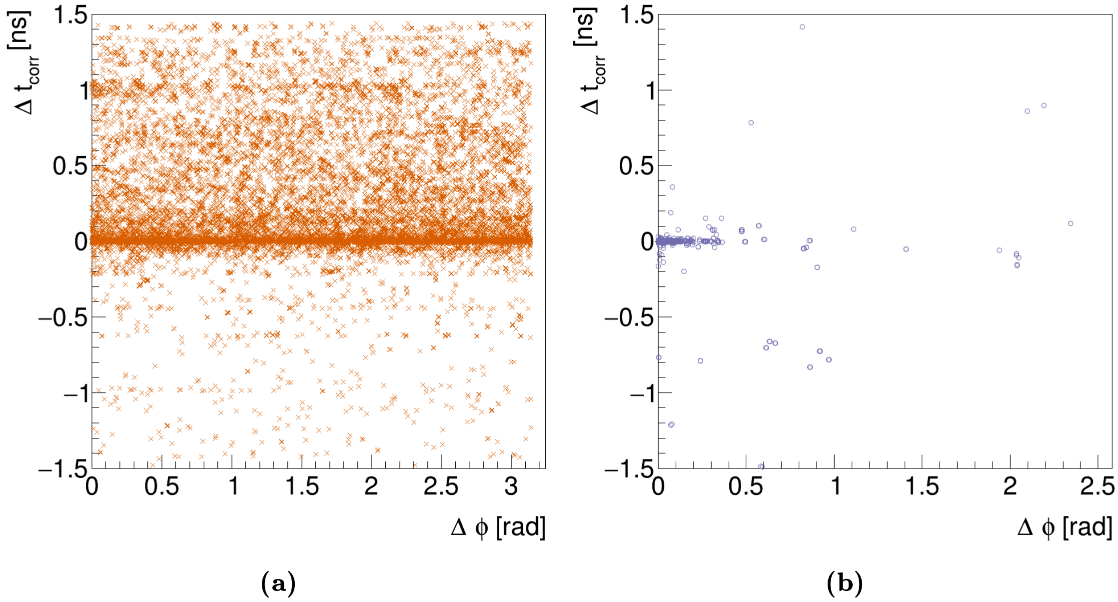

Figure 7.10. Scatter matrix plot for the doublet coordinates Δt_{corr} and $\Delta\phi$. The corrected time difference can be used in cuts.

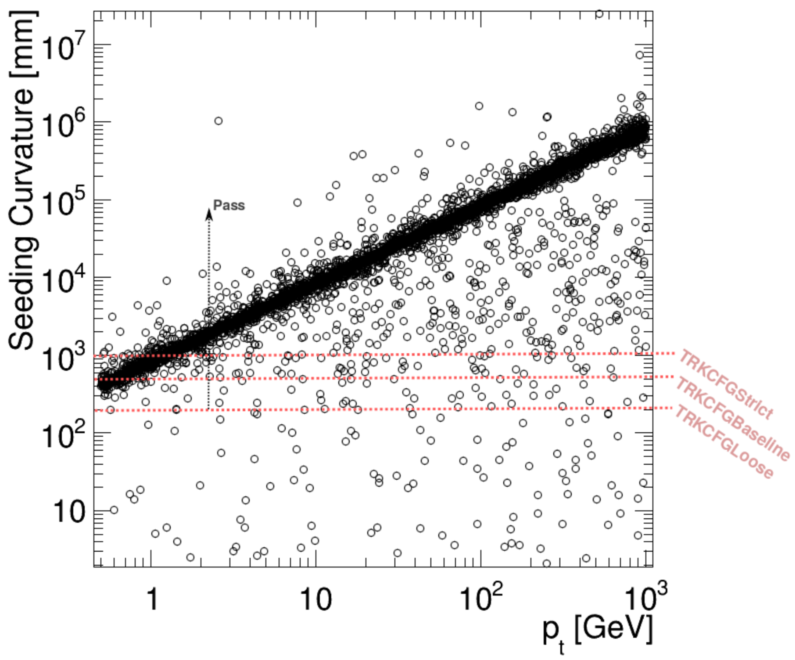

Figure 7.11. Plot of hit triplet curvature versus the particle transverse momentum. The minimum curvature is used as a parameter to filter for fake seeds.

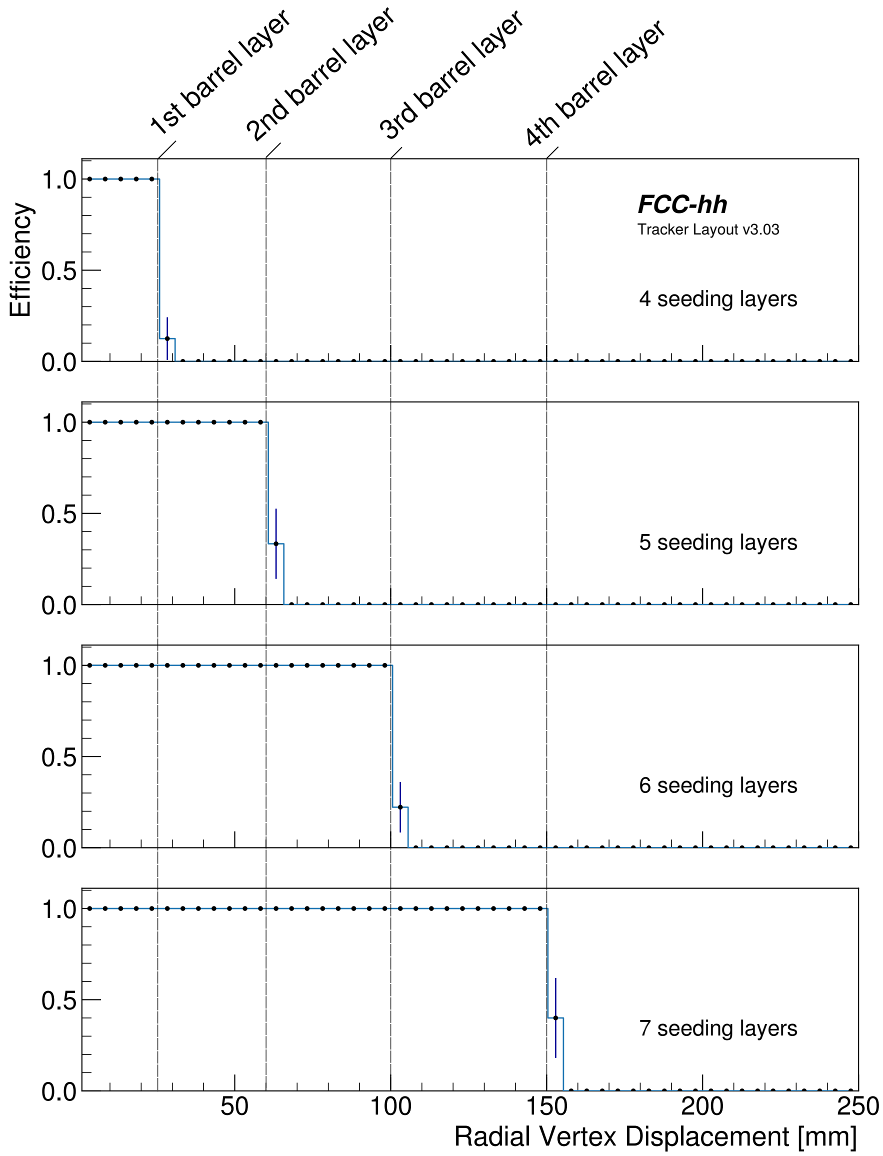

Figure 7.12. Acceptance of the radial track vertex displacement for different seeding layer configurations in FCC-hh. The acceptance is essentially a step function with respect to the vertex being within four seeding layers.

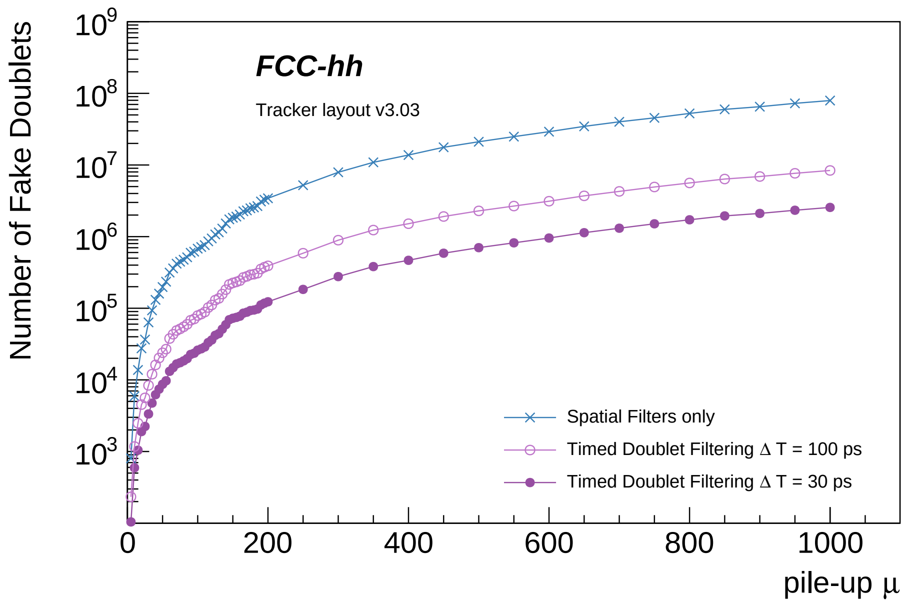

Figure 7.13. Number of fake doublets for different detector timing resolutions, as a function of pile-up μ. The default parametrization TRKCFGBaseline was used for the geometric hit filter.

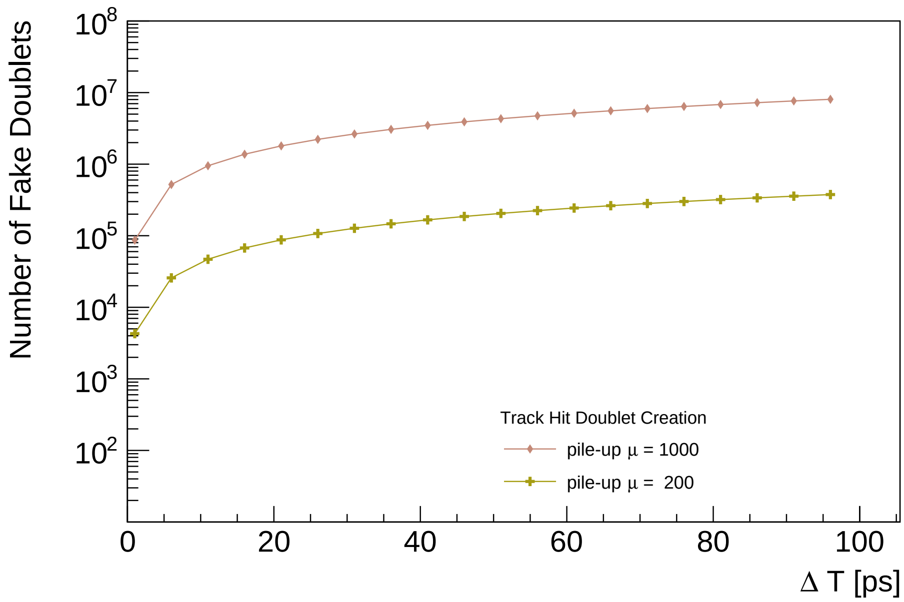

Figure 7.14. Number of fake doublets for different pile-up scenarios, as a function of ΔT.

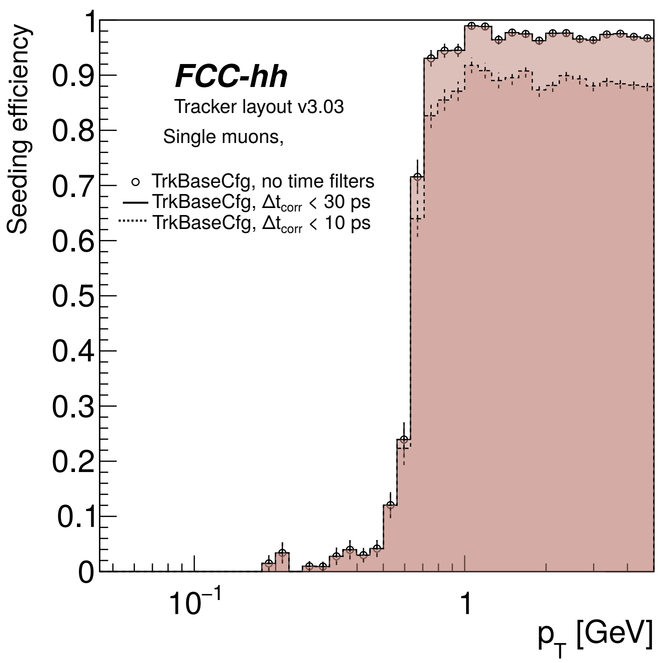

Figure 7.15. Efficiency of timed track seed filters for different timing cuts. With a filter window of 30 picoseconds (solid line), the efficiency curve is almost identical to the efficiency corresponding to geometric filters only (open circles).

Delphes fast simulation (between 0.8 and 0.95 for all particles with $p_T \geq 500$ MeV). It is possible to increase the acceptance by including more layers as root layers for the seeding, as shown in Fig. 7.12. This comes at a modest cost - if the seeding between any three layers is computationally feasible, then adding additional seeding layers requires only linearly more resources.

There is one region in the non-tilted tracker layout, however, that suffers from inefficiencies that cannot easily be rectified with changes to the seeding configuration. This region, immediately apparent in Fig. 7.5, extends from $3 < |\eta| < 4$, which coincides with the furthest extend of the inner barrel layer in the forward region. Due to the shallow crossing angle, particles traverse considerably more material on their trajectory, as is also seen in the material budget presented in Ch. 5. The conclusion is evidently that scattering processes are too intense in this region. Indeed, examining the geometric filters in detail shows that the curvature of seeding hit triplets is the dominant veto, and the tails of the curvature distribution are very wide in this critical region, as detailed in Fig. 7.16.

The tilted layout is here preferable in that reduces the crossing angle and the corresponding scattering rate in this region. To a minor extend, this also concerns the very forward region ($|\eta| > 5$). However, here the beam-pipe already gives rise to scattering. It is thus not possible to mitigate with the tracker design.

The possibility of reduction of the fake rate to practical levels is then investigated. While the complexity of finding pairs between n hits on each layer is only n^2, an efficient classifier is much harder to implement for the limited information that two hits provide. A filter on the angular difference of the azimuth ϕ depends sensitively on the minimum p_t to be reconstructed, but can already reduce the number of possible doublets by at least one order of magnitude. While z alone provides little information to limit the fake rate, the linear relationship between z and t significantly constrains the search space of relevant doublets. The use of Δt naturally requires timing detectors in use in all seeding layers.

Even if the overall scaling of the number of fake seeds is unchanged, of course, the reduction in combinatorics helps to limit the resources needed for reconstruction. Simple cuts on the doublet parameters can give an acceptable result, but a true multi-variate analysis exploiting the correlations between variables has the potential

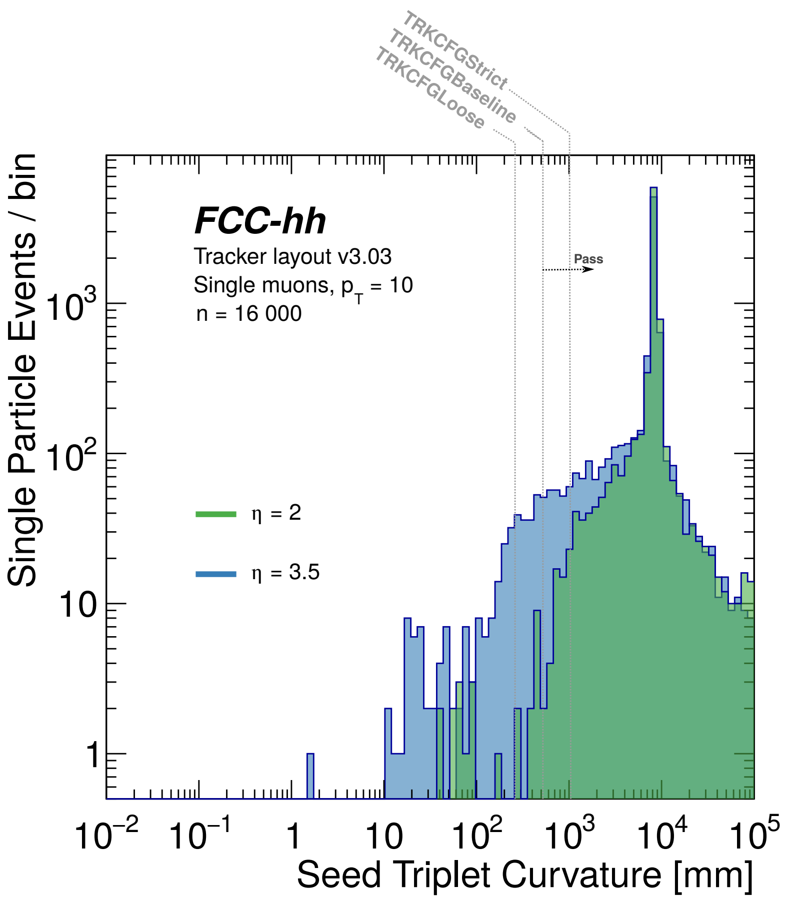

Figure 7.16. Distribution of the seed triplet curvature corresponding to single muons. This variable is used to discriminate fake from correct tracks and correlates with the transverse momentum of particles producing the track. At $\eta = 3.5$, a wide tail in the distribution can be observed.

to further optimize performance. As the FCC track reconstruction software becomes more complete and components such as iterative Kalman Filters are added, the implications of the track seeding performance will become immediately obvious. The effects of inhomogeneities in the magnetic field map should also be investigated in further studies, and while the reconstruction of all detectable charged tracks may be abandoned in the future in favor of more selective solutions that only use tracks in regions of interest, the goal is currently the reconstruction of all tracks.

Chapter 8.

Conclusion

This thesis examines the reliability and efficiency of track reconstruction with the FCC-hh detector concept proposed in the conceptual design report, and the possible impact of timing detectors. Tracking detectors at the FCC-hh must work in an environment of $\mu = 1000$, i.e., on average, they are exposed five times more pile-up collisions than at the HL-LHC. As current approaches to pile-up mitigation scale poorly, the question of computational performance and feasibility of track reconstruction in this extreme pile-up environment arises. While running the complete workflow of full simulation and reconstruction is the optimal test, the development of software capable of doing this was beyond the scope of this work, given the early stage of the overall FCC study, and will be a goal for a future technical design report. Instead, this work uses a more selective approach to identify track seeding as the most critical part of the reconstruction software in a high pile-up application, and develop and study those first.

A necessary requirement to study the reconstruction is to characterize the collisions and machine-detector interfaces. This is done to a quantititative study of the properties of pile-up at FCC-hh in Ch. 3, which shows that the average pile-up collision at FCC-hh is similar to the ones at LHC, although the products are oriented slightly more in the forward direction, and the average transverse momentum is higher. The spatial and temporal distribution of pile-up collisions across the beam-spot, which has implications for pile-up mitigation, is calculated as well.

The track detector design, which constitutes the baseline for the FCC-hh conceptual design report, and analytical studies of its performance are presented in Ch. 5, while

Ch. 4 reviews the fundamental concepts or track reconstruction. The additional value of timing detectors is evaluated using approximate analytical methods that calculate a reduced, effective pile-up in presence of pile-up mitigation using timing information.

In order to refine these approximate calculations new software developments were needed, which were carried out and documented in Ch. 6. In particular, the efficient simulation of pile-up relies on infrastructure to use pre-simulated minimum bias events, which was added to the software framework in the course of this thesis. Part of these developments is *tricktrack*, a track seeding library, which encapsulates code from the CMS experiment. Its performance characteristics are described in order to establish a baseline computing performance for the track seeding stage of the reconstruction.

The flexibility of the newly developed track seeding library finally allowed for a full simulation study of track seeding with timing information. The results in Ch. 7, comparing different levels of pile-up and timing capabilities of the detector, confirm the more approximate analytical results and show that an ambitious but realistic timing resolution of 30 ps can reduce the pile-up to an effective environment similar to the HL-LHC, i.e. $\mu \sim 200$.

Appendix A.

FCC Software Stack

package-name	version	homepage	description
hep-acts-core	0.7.1	http://acts.web.cern.ch	ACTS is a common tracking software for HEP experiments.
hep-clhep	2.4.1.0	https://proj-clhep.web.cern.ch/proj-clhep/	CLHEP is a class library for High Energy Physics.
hep-dag	0.1-0	https://github.com/HEP-FCC/dag	DAG is a C++ library for directed acyclic graphs.
hep-dd4hep	1.08	https://cern.ch/dd4hep	DD4hep is a detector description toolkit for HEP.
hep-delphes	3.4.2.16	https://cp3.irmp.ucl.ac.be/projects/delphes	Delphes, a framework for fast simulation of a generic collider experiment.

package-name	version	homepage	description
hep-fastjet	3.3.0	http://fastjet.fr/	Fastjet, a software package for jet finding in pp and e+e- collisions.
hep-fcc-physics	0.0	https://github.com/HEP-FCC/fcc-physics	Command line tools for physics studies at the FCC.
hep-fccedm	0.5.4	https://github.com/HEP-FCC/fcc-edm	FCC-edm is the common event data model library for the Future Circular Collider.
hep-fccedmlegacy	0.0.1	https://github.com/HEP-FCC/fcc-edm-legacy	FCC-EDM datatypes needed for legacy data.
hep-fcchhanalyses	0.0.1	https://github.com/FCC-hh-framework/FCChhAnalyses	Physics analyses for the FCC-hh and HE-LHC, written in heppy.
hep-fccrepoconfig	0.0	https://cern.ch/fccsw	Metapackage configuring the ubuntu repository for FCC software.
hep-fccsw-crmc	0.0	https://gitlab.cern.ch/vavolkl/fcchh-study-SimCRCM	Geant components for the use of crmc in FCCSW.
hep-fccsw	0.9.1	https://github.com/HEP-FCC/FCCSW	FCCSW is the software framework for the future circular collider.

package-name	version	homepage	description
hep-flattreeanalyzer	0.0.1	https://github.com/FCC-hh-framework/FlatTreeAnalyzer	FlatTreeAnalyzer is a set of scripts for precessing flat trees produced with the Heppy framework.
hep-gaudi	v29r2	https://gitlab.cern.ch/gaudi/gaudi	Gaudi, a event processing framework for HEP experiments.
hep-geant4	10.4.2	https://geant4.web.cern.ch/	Geant4 is a toolkit for the simulation of the passage of particles through matter.
hep-geant4data	0.0	https://geant4.web.cern.ch/	Required data sets needed to run Geant4.
hep-hepmc	2.06.09	https://lcgapp.cern.ch/project/simu/HepMC/	HepMC is a C++ Event Record for Monte Carlo Generators.
hep-heppdt	2.06.01	https://lcgapp.cern.ch/project/simu/HepPDT/	HepPDT is a C++ Particle Data Table.
hep-heppy	2.0.1	https://github.com/HEP-FCC/heppy	Heppy is a python analysis framework for high energy physics

package-name	version	homepage	description
hep-madgraph	2.6.2	https://cp3.irmp.ucl.ac.be/projects/madgraph/	Madgraph is a framework for computations of cross sections, the generation of hard events and their matching with event generators.
hep-podio	0.9.0	https://github.com/HEP-FCC/podio	PODIO is a generator for plain-old-data-based data models.
hep-pythia8	2.4.0	http://home.thep.lu.se/Pythia/	Pythia is a standard tool for the generation of events in high-energy collisions.
hep-root	6.16.0	https://root.cern.ch	ROOT: a modular scientific software toolkit.
hep-tricktrack	1.7.1	https://github.com/HSF/TrickTrack	HEP track seeding library for pattern recognition with Cellular Automata.
hep-vc	1.3.2	https://github.com/VcDevel/Vc	SIMD Vector Classes for C++
hep-veccore	0.4.2	https://gitlab.cern.ch/VecGeom/VecCore	SIMD Vectorization Library for VecGeom and GeantV.

package-name	version	homepage	description
hep-vecgeom	0.05.01	https://gitlab.cern.ch/VecGeom/VecGeom	VecGeom, the vectorized geometry library for particle-detector simulation (toolkits).

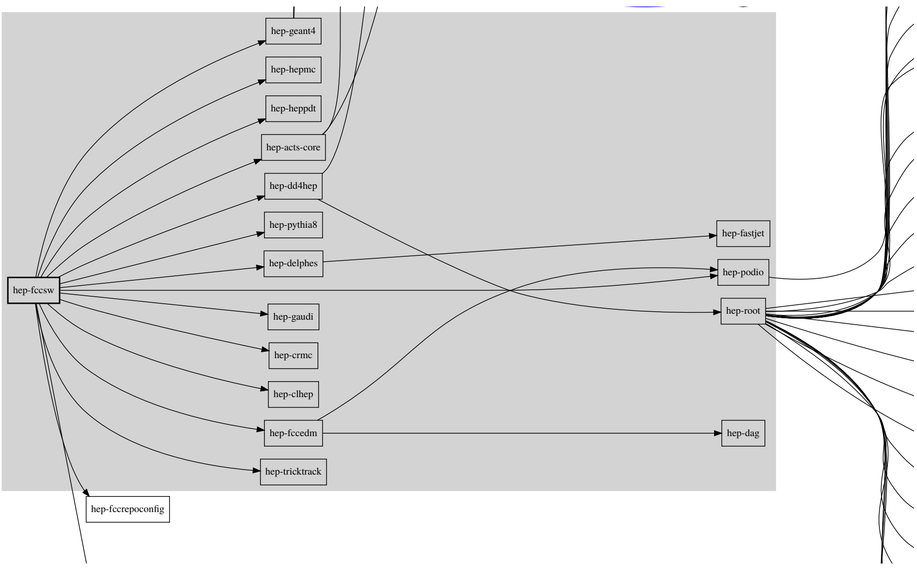

Figure A.1. A simplified diagram showing the interdependencies of HEP/FCC software packages

Appendix B.

Technical Specification of Tracker Layout

The following Tables: B.1, B.2, B.3 (Barrel) and B.4, B.5 (End-cap) provide the detailed documentation of tracker layout parameters [58, 87]. Several types of detector modules are assumed in the layouts – of various shapes, sizes, granularity; their summary is given in Tables[1]: B.6 and B.7.

[1] The parametric description of wedge-shaped pixel regions is only approximative and more realistic design is still expected.

Inner tracker - flat layout:							
BRL Layer:	1	2	3	4	5	6	**Total ⟨-z; +z⟩**
R_{avg} [mm]	25.0	60.0	100.0	150.0	270.0	400.0	
R_{min} [mm]	23.3	58.3	98.3	148.3	261.1	391.1	
R_{max} [mm]	27.5	63.0	102.5	152.3	280.1	409.7	
Z_{min} [mm]	−685.0	−820.0	−820.0	−820.0	−820.0	−820.0	
Z_{max} [mm]	+685.0	+820.0	+820.0	+820.0	+820.0	+820.0	
N_{rods}	14	16	26	38	34	50	
$N_{modules/rod}$	20	40	40	40	17	17	
$N_{modules}$	280	640	1040	1520	578	850	4908
Outer tracker - flat layout:							
BRL Layer:	7	8	9	10	11	12	**Total ⟨-z; +z⟩**
R_{avg} [mm]	530.0	742.4	937.2	1132.0	1326.7	1539.6	
R_{min} [mm]	521.1	733.5	928.0	1122.7	1317.4	1530.3	
R_{max} [mm]	541.4	753.1	947.9	1142.5	1337.0	1549.7	
Z_{min} [mm]	−2250.0	−2250.0	−2250.0	−2250.0	−2250.0	−2250.0	
Z_{max} [mm]	+2250.0	+2250.0	+2250.0	+2250.0	+2250.0	+2250.0	
N_{rods}	34	46	58	70	82	96	
$N_{modules/rod}$	47	47	47	47	47	47	
$N_{modules}$	1598	2162	2726	3290	3854	4512	18142

Inner tracker - tilted layout:							
BRL Layer:	1	2	3	4	5	6	**Total ⟨-z; +z⟩**
R_{avg} [mm]	25.7	60.0	100.0	150.0	260.0	380.0	
R_{min} [mm]	22.9	46.7	86.7	136.8	207.8	328.7	
R_{max} [mm]	29.7	74.4	114.0	163.7	313.2	432.1	
Z_{min} [mm]	−800.0	−800.0	−800.0	−800.0	−728.7	−800.0	
Z_{max} [mm]	+800.0	+800.0	+800.0	+800.0	+728.7	+800.0	
N_{rods}	14	18	28	40	38	54	
$N_{modules/rod}$	29	25	29	35	11	13	
$N_{modules}$	406	450	812	1400	418	702	4188
Outer tracker - tilted layout:							
BRL Layer:	7	8	9	10	11	12	**Total ⟨-z; +z⟩**
R_{avg} [mm]	530.0	742.4	937.3	1132.0	1326.8	1539.9	
R_{min} [mm]	475.0	688.4	884.5	1080.8	1277.0	1530.6	
R_{max} [mm]	587.1	798.0	991.3	1184.4	1377.4	1550.0	
Z_{min} [mm]	−2300.0	−2290.7	−2300.0	−2300.0	−2300.0	−2299.6	
Z_{max} [mm]	+2300.0	+2290.7	+2300.0	+2300.0	+2300.0	+2299.6	
N_{rods}	36	50	62	74	86	96	
$N_{modules/rod}$	25	29	33	35	37	47	
$N_{modules}$	900	1450	2046	2590	3182	4512	14680

Table B.1.: Barrel layers: Inner and Outer Tracker in flat (v3.03) and tilted (v4.01) layouts. Subscripts: *min*, *max* and *avg* correspond to minimum, maximum and average position, respectively. A layer consists of several ladders (rods), a ladder of a set of modules, arranged to rings in tilted layout.

Layer 1 Ring:	1	2	3	4	5	6	7	8	9	10	11	12	13
ϑ_{tilt} [deg]	0.0	0.0	0.0	0.0	0.0	10.0	10.0	10.0	10.0	10.0	10.0	10.0	10.0
R_{inner} [mm]	24.0	24.0	24.0	24.0	24.0	25.4	25.4	25.4	25.4	25.4	25.4	25.4	25.4
R_{outer} [mm]	26.0	26.0	26.0	26.0	26.0	26.4	26.4	26.4	26.4	26.4	26.4	26.4	26.4
$\lvert Z_{\text{avg}}\rvert$ [mm]	0.0	24.4	48.7	73.1	97.4	126.3	163.2	206.8	258.3	319.2	388.5	468.0	559.4
	14	15											
	10.0	10.0											
	25.4	25.4											
	26.4	26.4											
	664.2	787.4											

Layer 2 Ring:	1	2	3	4	5	6	7	8	9	10	11	12	13
ϑ_{tilt} [deg]	0.0	0.0	0.0	0.0	0.0	0.0	70.5	70.5	79.2	79.2	83.9	83.9	83.9
R_{inner} [mm]	59.0	59.0	59.0	59.0	59.0	59.0	59.5	59.5	59.5	59.5	59.5	59.5	59.5
R_{outer} [mm]	61.0	61.0	61.0	61.0	61.0	61.0	60.5	60.5	60.5	60.5	60.5	60.5	60.5
$\lvert Z_{\text{avg}}\rvert$ [mm]	0.0	24.4	48.7	73.1	97.4	121.8	149.1	197.1	267.7	375.2	482.1	619.9	796.9

Layer 3 Ring:	1	2	3	4	5	6	7	8	9	10	11	12	13
ϑ_{tilt} [deg]	0.0	0.0	0.0	0.0	0.0	0.0	58.3	58.3	67.5	67.5	74.8	74.8	80.0
R_{inner} [mm]	99.0	99.0	99.0	99.0	99.0	99.0	99.5	99.5	99.5	99.5	99.5	99.5	99.5
R_{outer} [mm]	101.0	101.0	101.0	101.0	101.0	101.0	100.5	100.5	100.5	100.5	100.5	100.5	100.5
$\lvert Z_{\text{avg}}\rvert$ [mm]	0.0	24.4	48.7	73.1	97.4	121.8	146.8	179.5	219.2	268.9	331.1	410.6	512.0
	14	15											
	80.0	84.0											
	99.5	99.5											
	100.5	100.5											
	642.6	796.9											

Layer 4 Ring:	1	2	3	4	5	6	7	8	9	10	11	12	13
ϑ_{tilt} [deg]	0.0	0.0	0.0	0.0	0.0	0.0	46.8	46.8	56.0	56.0	63.6	63.6	69.9
R_{inner} [mm]	149.0	149.0	149.0	149.0	149.0	149.0	149.5	149.5	149.5	149.5	149.5	149.5	149.5
R_{outer} [mm]	151.0	151.0	151.0	151.0	151.0	151.0	150.5	150.5	150.5	150.5	150.5	150.5	150.5
$\lvert Z_{\text{avg}}\rvert$ [mm]	0.0	24.4	48.7	73.1	97.4	121.8	146.4	174.5	205.6	240.8	281.0	327.4	380.9
	14	15	16	17	18								
	69.9	74.9	74.9	78.6	78.6								
	149.5	149.5	149.5	149.5	149.5								
	150.5	150.5	150.5	150.5	150.5								
	443.7	517.1	603.6	693.4	796.1								

Layer 5 Ring:	1	2	3	4	5	6
ϑ_{tilt} [deg]	0.0	0.0	43.9	43.9	65.5	65.5
R_{inner} [mm]	257.5	252.5	255.0	255.0	255.0	255.0
R_{outer} [mm]	267.5	262.5	265.0	265.0	265.0	265.0
$\lvert Z_{\text{avg}}\rvert$ [mm]	0.0	99.9	195.6	319.1	475.0	700.1

Layer 6 Ring:	1	2	3	4	5	6	7
ϑ_{tilt} [deg]	0.0	0.0	33.5	33.5	53.1	53.1	63.1
R_{inner} [mm]	377.5	372.5	375.0	375.0	375.0	375.0	375.0
R_{outer} [mm]	387.5	382.5	385.0	385.0	385.0	385.0	385.0
$\lvert Z_{\text{avg}}\rvert$ [mm]	0.0	100.7	198.6	310.7	436.1	591.8	770.2

Table B.2.: Barrel layers: detailed parameters of Inner Tracker in tilted (v4.01) layout. R_{inner} and R_{outer} describe the central radial position of inner and outer ladder ring module, respectively; inner/outer correspond to an even/odd or odd/even ladder ring module within the given barrel layer.

Layer 7 Ring:	1	2	3	4	5	6	7	8	9	10	11
$\vartheta_{\mathrm{tilt}}$ [deg]	0.0	0.0	0.0	34.1	34.1	49.2	49.2	60.8	60.8	69.5	69.5
R_{inner} [mm]	522.5	527.5	522.5	525.0	525.0	525.0	525.0	525.0	525.0	525.0	525.0
R_{outer} [mm]	532.5	537.5	532.5	535.0	535.0	535.0	535.0	535.0	535.0	535.0	535.0
$\|Z_{\mathrm{avg}}\|$ [mm]	0.0	101.8	202.0	303.7	419.4	545.2	691.4	857.6	1055.9	1287.6	1567.3
	12	13									
	75.6	75.6									
	525.0	525.0									
	535.0	535.0									
	1890.0	2276.2									

Layer 8 Ring:	1	2	3	4	5	6	7	8	9	10	11
$\vartheta_{\mathrm{tilt}}$ [deg]	0.0	0.0	0.0	0.0	31.9	31.9	43.6	43.6	53.4	53.4	61.4
R_{inner} [mm]	739.9	734.9	739.9	734.9	737.4	737.4	737.4	737.4	737.4	737.4	737.4
R_{outer} [mm]	749.9	744.9	749.9	744.9	747.4	747.4	747.4	747.4	747.4	747.4	747.4
$\|Z_{\mathrm{avg}}\|$ [mm]	0.0	101.2	203.3	302.6	406.3	521.5	643.2	777.7	923.6	1087.5	1268.6
	12	13	14	15							
	61.4	67.9	67.9	71.3							
	737.4	737.4	737.4	737.4							
	747.4	747.4	747.4	747.4							
	1474.3	1704.4	1967.5	2265.1							

Layer 9 Ring:	1	2	3	4	5	6	7	8	9	10	11
$\vartheta_{\mathrm{tilt}}$ [deg]	0.0	0.0	0.0	0.0	0.0	31.0	31.0	40.7	40.7	49.1	49.1
R_{inner} [mm]	929.8	934.8	929.8	934.8	929.8	932.3	932.3	932.3	932.3	932.3	932.3
R_{outer} [mm]	939.8	944.8	939.8	944.8	939.8	942.3	942.3	942.3	942.3	942.3	942.3
$\|Z_{\mathrm{avg}}\|$ [mm]	0.0	101.8	202.0	304.5	402.8	507.6	622.9	743.2	873.0	1010.9	1161.3
	12	13	14	15	16	17					
	56.4	56.4	62.4	62.4	66.7	66.7					
	932.3	932.3	932.3	932.3	932.3	932.3					
	942.3	942.3	942.3	942.3	942.3	942.3					
	1323.1	1501.1	1694.6	1909.0	2083.3	2272.0					

Layer 10 Ring:	1	2	3	4	5	6	7	8	9	10	11
$\vartheta_{\mathrm{tilt}}$ [deg]	0.0	0.0	0.0	0.0	0.0	0.0	30.4	30.4	38.6	38.6	46.0
R_{inner} [mm]	1129.5	1124.5	1129.5	1124.5	1129.5	1124.5	1127.0	1127.0	1127.0	1127.0	1127.0
R_{outer} [mm]	1139.5	1134.5	1139.5	1134.5	1139.5	1134.5	1137.0	1137.0	1137.0	1137.0	1137.0
$\|Z_{\mathrm{avg}}\|$ [mm]	0.0	101.2	203.3	302.6	405.4	502.7	608.2	723.5	842.9	969.8	1102.7
	12	13	14	15	16	17	18				
	46.0	52.5	52.5	58.2	58.2	62.5	62.5				
	1127.0	1127.0	1127.0	1127.0	1127.0	1127.0	1127.0				
	1137.0	1137.0	1137.0	1137.0	1137.0	1137.0	1137.0				
	1245.3	1396.1	1558.9	1732.6	1921.0	2089.2	2269.8				

Layer 11 Ring:	1	2	3	4	5	6	7	8	9	10	11
$\vartheta_{\mathrm{tilt}}$ [deg]	0.0	0.0	0.0	0.0	0.0	0.0	0.0	30.0	30.0	37.1	37.1
R_{inner} [mm]	1319.3	1324.3	1319.3	1324.3	1319.3	1324.3	1319.3	1321.8	1321.8	1321.8	1321.8
R_{outer} [mm]	1329.3	1334.3	1329.3	1334.3	1329.3	1334.3	1329.3	1331.8	1331.8	1331.8	1331.8
$\|Z_{\mathrm{avg}}\|$ [mm]	0.0	101.8	202.0	304.5	402.8	505.9	602.3	708.2	823.5	942.3	1067.2

	12	13	14	15	16	17	18	19
	43.6	43.6	49.5	49.5	54.7	54.7	58.8	58.8
	1321.8	1321.8	1321.8	1321.8	1321.8	1321.8	1321.8	1321.8
	1331.8	1331.8	1331.8	1331.8	1331.8	1331.8	1331.8	1331.8
	1197.1	1334.5	1478.5	1631.7	1793.2	1965.9	2112.5	2267.7

Table B.3.: Barrel layers: detailed parameters of Outer Tracker in tilted (v4.01) layout. The rings positioning of the 12^{th} layer is not displayed as it follows the same layout as of the 12^{th} barrel layer in flat configuration, c.f. Table B.1. R_{inner} and R_{outer} describe the central radial position of inner and outer ladder ring module, respectively.

Inner tracker:									
EC Disc:	1	2	3	4	5				**Total ⟨-z; +z⟩**
R_{min} [mm]	25.0	25.0	25.0	25.0	25.0				
R_{max} [mm]	404.0	404.0	404.0	404.0	404.0				
$\lvert Z_{\mathrm{avg}} \rvert$ [mm]	950.0	1178.5	1462.0	1813.7	2250.0				
$\lvert Z_{\mathrm{min}} \rvert$ [mm]	941.1	1169.6	1453.1	1804.8	2241.1				
$\lvert Z_{\mathrm{max}} \rvert$ [mm]	958.9	1187.5	1471.0	1822.6	2258.9				
N_{rings}	4	4	4	4	4				
$N_{\mathrm{modules/disc}}$	108	108	108	108	108				1080
EC Ring:	1	2	3	4					
R_{min} [mm]	25.0	101.3	198.9	302.6					
R_{max} [mm]	104.7	204.6	303.4	404.0					
$N_{\mathrm{modules/ring}}$	12	20	32	44					
Outer tracker:									
EC Disc:	1	2	3	4	5	6			**Total ⟨-z; +z⟩**
R_{min} [mm]	25.0	25.0	25.0	25.0	25.0	25.0			
R_{max} [mm]	1549.3	1549.3	1549.3	1549.3	1549.3	1549.3			
$\lvert Z_{\mathrm{avg}} \rvert$ [mm]	2625.0	2986.1	3396.8	3864.0	4395.4	5000.0			
$\lvert Z_{\mathrm{min}} \rvert$ [mm]	2615.7	2976.8	3387.5	3854.7	4386.1	4990.7			
$\lvert Z_{\mathrm{max}} \rvert$ [mm]	2634.3	2995.3	3406.1	3873.3	4404.7	5009.3			
N_{rings}	16	16	16	16	16	16			
$N_{\mathrm{modules/disc}}$	948	948	948	948	948	948			11376
EC Ring:	1	2	3	4	5	6	7	8	
R_{min} [mm]	25.0	99.9	198.8	301.4	398.7	503.5	599.0	701.6	
R_{max} [mm]	104.2	203.1	303.1	402.6	504.4	603.6	703.2	805.6	
$N_{\mathrm{modules/ring}}$	12	20	32	44	52	64	44	52	
	9	10	11	12	13	14	15	16	
	798.9	901.7	997.9	1100.9	1195.9	1299.1	1393.0	1496.4	
	902.7	1005.4	1101.5	1204.4	1299.3	1402.4	1496.3	1549.3	
	56	64	68	76	84	88	96	96	

Table B.4.: End-cap discs/rings of Inner and Outer Tracker: with the same layout for flat and tilted geometry.

Forward tracker:									
EC Disc:	1	2	3						**Total ⟨-z; +z⟩**
R_{min} [mm]	25.0	25.0	25.0						
R_{max} [mm]	918.6	1120.2	1321.5						
$\lvert Z_{\text{avg}} \rvert$ [mm]	6250.0	7395.1	8750.0						
$\lvert Z_{\text{min}} \rvert$ [mm]	6241.1	7385.8	8740.7						
$\lvert Z_{\text{max}} \rvert$ [mm]	6258.9	7404.4	8759.3						
N_{rings}	9	11	13						
$N_{\text{modules/disc}}$	388	524	684						3192
EC Ring:	1	2	3	4	5	6	7	8	9
R_{min} [mm]	25.0	115.8	215.5	315.6	414.4	514.4	612.5	714.8	814.7
R_{max} [mm]	120.6	219.3	317.5	417.0	515.4	615.2	716.7	818.8	918.6
$N_{\text{modules/ring}}$	12	20	32	44	56	64	48	52	60
	10	11	12	13					
	917.2	1016.6	1119.2	1218.1					
	1020.9	1120.2	1222.6	1321.5					
	64	72	76	84					
EC Disc:	4	5	6	7	8	9			**Total ⟨-z; +z⟩**
R_{min} [mm]	49.5	49.5	49.5	49.5	49.5	49.5			
R_{max} [mm]	1550.2	1550.2	1550.2	1550.2	1550.2	1550.2			
$\lvert Z_{\text{avg}} \rvert$ [mm]	10000.0	10985.6	12068.4	13257.8	14564.5	16000.0			
$\lvert Z_{\text{min}} \rvert$ [mm]	9990.7	10976.3	12059.1	13248.5	14555.2	15990.7			
$\lvert Z_{\text{max}} \rvert$ [mm]	10009.3	10994.9	12077.6	13267.1	14573.8	16009.3			
N_{rings}	15	15	15	15	15	15			
$N_{\text{modules/disc}}$	868	868	868	868	868	868			10416
EC Ring:	1	2	3	4	5	6	7	8	9
R_{min} [mm]	49.5	139.1	238.2	337.8	436.7	536.3	637.3	739.4	840.0
R_{max} [mm]	144.6	241.2	339.6	438.8	537.5	640.8	741.4	843.4	943.8
$N_{\text{modules/ring}}$	12	24	36	48	56	40	48	52	60
	10	11	12	13	14	15			
	942.2	1042.6	1144.8	1244.9	1347.2	1446.9			
	1045.9	1146.1	1248.3	1348.2	1450.5	1550.2			
	68	72	80	84	92	96			

Table B.5.: End-cap discs/rings of Forward Tracker: with the same layout for flat and tilted geometry.

Detector modules - tilted:					
BRL Layers:	r-$\varphi \times z$ dims [mm^2]	X/X_0 [%]	$N_{\text{chips}} \times N_{\text{ch}} \times r$-$\varphi$ pitch [μm]	$N_{\text{chips}} \times N_{\text{ch}} \times z$ pitch [μm]	N_{modules}
1	12.8×25.6	1.0	$1 \times 512 \times 25$	$1 \times 512 \times 50$	406
2-4	25.6×25.6	1.0	$2 \times 512 \times 25$	$1 \times 512 \times 50$	2662
5-6	51.2×102.4	2.0	$3 \times 512 \times 33.3$	$1 \times 256 \times 400$	1120
7-8	102.4×102.4	2.0	$6 \times 512 \times 33.3$	$1 \times 256 \times 400$	2350
9-11	102.4×102.4	2.5	$6 \times 512 \times 33.3$	$1 \times 58 \times 1750$	7818
12	102.4×102.4	2.5	$6 \times 512 \times 33.3$	$1 \times 2 \times 50000$	4512

Table B.6.: Detector module parameters in barrel region – tilted layout.

Detector modules - tilted:					
EC Rings – Inner:	$d_{\mathbf{wafer}}$ [mm]	X/X_0 [%]	$N_{\mathbf{chips}} \times N_{\mathbf{ch}} \times r$-$\varphi$ pitch [μm]	$N_{\mathbf{chips}} \times N_{\mathbf{ch}} \times z$ pitch [μm]	$N_{\mathbf{modules}}$
1 (w)	86.2	1.5	$(2 \times 512 + 328) \times 25$	$(2 \times 512 + 498) \times 50$	120
2 (w)	113.0	1.5	$(2 \times 512 + 418) \times 33.3$	$(1 \times 512 + 495) \times 100$	200
3 (w)	114.8	2.0	$(2 \times 512 + 456) \times 33.3$	258×400	320
4 (w)	112.6	2.0	$(2 \times 512 + 490) \times 33.3$	251×400	440
EC Rings – Outer:	$d_{\mathbf{wafer}}$ [mm]	X/X_0 [%]	$N_{\mathbf{chips}} \times N_{\mathbf{ch}} \times r$-$\varphi$ pitch [μm]	$N_{\mathbf{chips}} \times N_{\mathbf{ch}} \times z$ pitch [μm]	$N_{\mathbf{modules}}$
1 (w)	86.2	1.5	$(2 \times 512 + 373) \times 25$	$(2 \times 512 + 483) \times 50$	144
2 (w)	113.0	1.5	$(2 \times 512 + 427) \times 33.3$	$(1 \times 512 + 493) \times 100$	240
3 (w)	114.8	2.0	$(2 \times 512 + 474) \times 33.3$	257×400	384
4 (w)	112.6	2.0	$(2 \times 512 + 502) \times 33.3$	250×400	528
5 (w)	118.6	2.0	$(3 \times 512 + 118) \times 33.3$	262×400	624
6 (w)	113.7	2.0	$(3 \times 512 + 111) \times 33.3$	249×400	768
	r-$\varphi \times z$ dims [mm^2]	X/X_0 [%]	$N_{\mathbf{chips}} \times N_{\mathbf{ch}} \times r$-$\varphi$ pitch [μm]	$N_{\mathbf{chips}} \times N_{\mathbf{ch}} \times z$ pitch [μm]	$N_{\mathbf{modules}}$
7-9	102.4×102.4	2.0	$6 \times 512 \times 33.3$	$1 \times 256 \times 400$	1824
10-15	102.4×102.4	2.5	$6 \times 512 \times 33.3$	$1 \times 58 \times 1750$	5712
16	102.4×52.0	2.5	$6 \times 512 \times 33.3$	$1 \times 29 \times 1750$	1152
EC Rings – iForward:	$d_{\mathbf{wafer}}$ [mm]	X/X_0 [%]	$N_{\mathbf{chips}} \times N_{\mathbf{ch}} \times r$-$\varphi$ pitch [μm]	$N_{\mathbf{chips}} \times N_{\mathbf{ch}} \times z$ pitch [μm]	$N_{\mathbf{modules}}$
1 (w)	103.1	1.5	$(3 \times 512 + 146) \times 25$	$(3 \times 512 + 265) \times 50$	72
2 (w)	115.5	1.5	$(3 \times 512 + 107) \times 33.3$	$(1 \times 512 + 488) \times 100$	120
3 (w)	114.1	2.0	$(3 \times 512 + 76) \times 33.3$	250×400	192
4 (w)	113.7	2.0	$(3 \times 512 + 66) \times 33.3$	250×400	264
5 (w)	113.4	2.0	$(3 \times 512 + 57) \times 33.3$	250×400	336
6 (w)	114.8	2.0	$(3 \times 512 + 153) \times 33.3$	250×400	384
	r-$\varphi \times z$ dims [mm^2]	X/X_0 [%]	$N_{\mathbf{chips}} \times N_{\mathbf{ch}} \times r$-$\varphi$ pitch [μm]	$N_{\mathbf{chips}} \times N_{\mathbf{ch}} \times z$ pitch [μm]	$N_{\mathbf{modules}}$
7-9	102.4×102.4	2.0	$6 \times 512 \times 33.3$	$1 \times 256 \times 400$	960
10-13	102.4×102.4	2.5	$6 \times 512 \times 33.3$	$1 \times 58 \times 1750$	864
EC Rings – Forward:	$d_{\mathbf{wafer}}$ [mm]	X/X_0 [%]	$N_{\mathbf{chips}} \times N_{\mathbf{ch}} \times r$-$\varphi$ pitch [μm]	$N_{\mathbf{chips}} \times N_{\mathbf{ch}} \times z$ pitch [μm]	$N_{\mathbf{modules}}$
1 (w)	107.6	1.5	$(2 \times 512 + 373) \times 25$	$(2 \times 512 + 483) \times 50$	144
2 (w)	113.1	1.5	$(2 \times 512 + 427) \times 33.3$	$(1 \times 512 + 493) \times 100$	288
3 (w)	112.7	2.0	$(2 \times 512 + 474) \times 33.3$	257×400	432
4 (w)	112.7	2.0	$(2 \times 512 + 502) \times 33.3$	250×400	576
5 (w)	114.4	2.0	$(3 \times 512 + 118) \times 33.3$	262×400	672
	r-$\varphi \times z$ dims [mm^2]	X/X_0 [%]	$N_{\mathbf{chips}} \times N_{\mathbf{ch}} \times r$-$\varphi$ pitch [μm]	$N_{\mathbf{chips}} \times N_{\mathbf{ch}} \times z$ pitch [μm]	$N_{\mathbf{modules}}$
6-9	102.4×102.4	2.0	$6 \times 512 \times 33.3$	$1 \times 256 \times 400$	1824
10-15	102.4×102.4	2.5	$6 \times 512 \times 33.3$	$1 \times 58 \times 1750$	5712

Table B.7.: Detector module parameters in end-cap region – tilted layout. Different ring(s) layouts are used in the inner, outer and forward regions due to conical beam-pipe; two types of sensors are used: rectangular and wedge-shaped (denoted as w); the d_{wafer} is an assumed wafer diameter, necessary to form the wedge-shaped sensors at average z-position of respective end-cap and of required radial length, for further details refer to [81, 88].

Bibliography

[1] P.A. Zyla et al. *Review of Particle Physics.* PTEP, 2020(8):083C01, 2020. doi: 10.1093/ptep/ptaa104.

[2] Peter W. Higgs. *Broken Symmetries and the Masses of Gauge Bosons.* Phys. Rev. Lett., 13:508–509, 1964. doi: 10.1103/PhysRevLett.13.508. [,160(1964)].

[3] Andrew Purcell. *Go on a particle quest at the first CERN webfest. Le premier webfest du CERN se lance à la conquête des particules.* (BUL-NA-2012-269. 35/2012):10, Aug 2012. URL https://cds.cern.ch/record/1473657.

[4] Gordon Kane and Scott Watson. *Dark Matter and LHC: What is the Connection?* Mod. Phys. Lett., A23:2103–2123, 2008. doi: 10.1142/S0217732308028314.

[5] James M. Cline. *Is electroweak baryogenesis dead?. Is electroweak baryogenesis dead?* Philos. Trans. R. Soc. Lond., 376(CERN-TH-2017-096. 2114):20170116. 10 p, Apr 2017. doi: 10.1098/rsta.2017.0116. URL https://cds.cern.ch/record/2261858. 10 pages, 7 figures. Talk presented at Moriond Electroweak (24 Mar. 2017) and Higgs Cosmology workshop, Kavli Royal Society Centre, Chichley Hall, UK (28 Mar. 2017); v2: added discussion of bubble wall shape and velocity and references; published version.

[6] Nathaniel Craig, Andrey Katz, Matt Strassler, and Raman Sundrum. *Naturalness in the Dark at the LHC.* JHEP, 07:105, 2015. doi: 10.1007/JHEP07(2015)105.

[7] Bruno Benedetto Rossi. *High-energy particles.* Prentice-Hall physics. Prentice-Hall, New York, NY, 1952. URL https://cds.cern.ch/record/99081.

[8] *The European Strategy for Particle Physics Update 2013. La stratégie européenne*

pour la physique des particules Mise à jour 2013. 16th Session of European Strategy Council. May 2013. URL https://cds.cern.ch/record/1567258.

[9] Michelangelo Mangano and others (FCC Collaboration). *Future Circular Collider Conceptual Design Report, Vol. 1 : Physics opportunities*. Technical Report CERN-ACC-2018-0056, CERN, Geneva, Dec 2018. URL http://cds.cern.ch/record/2651294. Submitted for publication to Eur. Phys. J. C.

[10] Michael Benedikt and others (FCC Collaboration). *Future Circular Collider Conceptual Design Report, Vol. 2: The Lepton Collider (FCC-ee)*. Technical Report CERN-ACC-2018-0057, CERN, Geneva, Dec 2018. URL http://cds.cern.ch/record/2651299. Submitted for publication to Eur. Phys. J. ST.

[11] Michael Benedikt and others (FCC Collaboration). *Future Circular Collider Conceptual Design Report, Vol. 3 : The Hadron Collider (FCC-hh)*. Technical Report CERN-ACC-2018-0058, CERN, Geneva, Dec 2018. URL http://cds.cern.ch/record/2651300. Submitted for publication to Eur. Phys. J. ST.

[12] Frank Zimmermann and others (FCC Collaboration). *Future Circular Collider Conceptual Design Report, Vol. 4: The High-Energy LHC (HE-LHC)*. Technical Report CERN-ACC-2018-0059, CERN, Geneva, Dec 2018. URL http://cds.cern.ch/record/2651305. Submitted for publication to Eur. Phys. J. ST.

[13] N. Alipour Tehrani et al. *FCC-ee: Your Questions Answered*. In A. Blondel and P. Janot, editors, *CERN Council Open Symposium on the Update of European Strategy for Particle Physics (EPPSU) Granada, Spain, May 13-16, 2019*, 2019.

[14] Linda Stoel, Michael Barnes, Wolfgang Bartmann, Florian Burkart, Brennan Goddard, Werner Herr, Thomas Kramer, Attilio Milanese, Giovanni Rumolo, and Elena Shaposhnikova. *High Energy Booster Options for a Future Circular Collider at CERN*. (CERN-ACC-2016-291):MOPOY007. 4 p, 2016. doi: 10.18429/JACoW-IPAC2016-MOPOY007. URL http://cds.cern.ch/record/2207334.

[15] Alexander Chao, Ronald Davidson, Alexander Dragt, Gerald Dugan, Norbert Holtkamp, Chan Joshi, Thomas Roser, Ronald Ruth, John Seeman, and Jim

Strait. *2001 Snowmass Accelerator R & D Report*. Technical report, Fermi National Accelerator Lab.(FNAL), Batavia, IL (United States), 2001.

[16] Mogens Dam. *Tau-lepton Physics at the FCC-ee circular e^+e^- Collider*. SciPost Phys. Proc., 1:041, 2019. doi: 10.21468/SciPostPhysProc.1.041.

[17] Niloufar Alipour Tehrani. *Simulation and tracking studies for a drift chamber at the FCC-ee experiment*. Technical Report CERN-ACC-2019-0043, CERN, Geneva, Apr 2019. URL http://cds.cern.ch/record/2670936.

[18] Oleksandr Viazlo. *Fine-grained calorimeters for experiments at CLIC and FCC-ee*. Technical Report CLICdp-Conf-2018-005, CERN, Geneva, Aug 2018. URL https://cds.cern.ch/record/2634087.

[19] Abelleira Fernandez et al. *A Large Hadron Electron Collider at CERN: Report on the Physics and Design Concepts for Machine and Detector*. J. Phys. G, 39(SLAC-R-999. CERN-OPEN-2012-015. CERN-LHeC-Note-2012-002-GEN):075001. 633 p, Jun 2012. URL http://cds.cern.ch/record/1456019.

[20] Max Klein. *Physics at HERA and Beyond*. AIP Conference Proceedings, 792(1): 1065–1076, 2005. doi: 10.1063/1.2122221. URL https://aip.scitation.org/doi/abs/10.1063/1.2122221.

[21] M. Aicheler, P.N. Burrows, N. Catalan, R. Corsini, M. Draper, J. Osborne, D. Schulte, S. Stapnes, and M.J. Stuart. *The Compact Linear Collider (CLIC) – Project Implementation Plan*. CERN Yellow Reports: Monographs. CERN, Geneva, Dec 2018. URL http://cds.cern.ch/record/2652600.

[22] Compact Linear Collider Project CLIC. *CLIC accelerator footprint*. Dec 2017. URL https://cds.cern.ch/record/2297076. General Photo.

[23] Thomas Schrorner-Sadenius. *The International Linear Collider: Physics Case and Status*. PoS, CORFU2018:019, 2019. doi: 10.22323/1.347.0019.

[24] Xin Shi. *Overview of the Cepc Project*. In *Proceedings, 18th Lomonosov Conference on Elementary Particle Physics: Moscow, Russia, August 24-30, 2017*, pages 189–192, 2019. doi: 10.1142/9789811202339_0038.

[25] S Heinemeyer et al. *Handbook of LHC Higgs Cross Sections: 3. Higgs Properties: Report of the LHC Higgs Cross Section Working Group*. CERN Yellow Reports: Monographs. Jul 2013. URL https://cds.cern.ch/record/1559921. Comments: 404 pages, 139 figures, to be submitted to CERN Report. Working Group web page: https://twiki.cern.ch/twiki/bin/view/LHCPhysics/CrossSections.

[26] Michelangelo Mangano et al. *Physics at the FCC-hh, a 100 TeV pp collider*, volume 3 of *CERN Yellow Reports: Monographs*. Oct 2017. URL http://cds.cern.ch/record/2270978.

[27] Estel Perez Codina and Philipp Gerhard Roloff. *Tracking and Flavour Tagging at FCC-hh*. Technical Report CERN-ACC-2018-0027, CERN, Geneva, Aug 2018. URL http://cds.cern.ch/record/2635893.

[28] T. Carli, C. Helsens, A. Henriques Correia, and C. Solans Sánchez. *Containment and resolution of hadronic showers at the FCC*. Journal of Instrumentation, 11 (09):P09012–P09012, sep 2016. doi: 10.1088/1748-0221/11/09/p09012. URL https://doi.org/10.1088%2F1748-0221%2F11%2F09%2Fp09012.

[29] ATLAS Collaboration. *Expected pileup values at the HL-LHC*. Technical Report ATL-UPGRADE-PUB-2013-014, CERN, Geneva, Sep 2013. URL https://cds.cern.ch/record/1604492.

[30] CMS Collaboration. *CMS luminosity measurement for the 2018 data-taking period at* $\sqrt{s} = 13$ TeV. Technical Report CMS-PAS-LUM-18-002, CERN, Geneva, 2019. URL https://cds.cern.ch/record/2676164.

[31] Stéphane Fartoukh. *Pile up management at the high-luminosity LHC and introduction to the crab-kissing concept*. Phys. Rev. ST Accel. Beams, 17(11):111001, 2014. URL doi.org/10.1103/PhysRevSTAB.17.111001.

[32] Michael Benedikt, Daniel Schulte, and Frank Zimmermann. *Optimizing integrated luminosity of future hadron colliders*. Phys. Rev. Spec. Top. Accel. Beams, 18 (CERN-ACC-2015-0166. 10):101002. 19 p, Oct 2015. URL https://cds.cern.ch/record/2112115.

[33] Torbjorn Sjostrand, Stephen Mrenna, and Peter Z. Skands. *A Brief Introduction to PYTHIA 8.1*. Comput. Phys. Commun., 178:852–867, 2008. doi: 10.1016/j.cpc.2008.01.036.

[34] *Standard Model Summary Plots Summer 2019*. Technical Report ATL-PHYS-PUB-2019-024, CERN, Geneva, Jul 2019. URL http://cds.cern.ch/record/2682186.

[35] Michelangelo Mangano. *Physics at the FCC-hh, a 100 TeV pp collider*. CERN Yellow Rep. Monogr., 3, 2017. doi: 10.23731/CYRM-2017-003.

[36] Rick Field. *Min-Bias and the Underlying Event at the LHC*. Acta Phys. Polon., B42:2631–2656, 2011. doi: 10.5506/APhysPolB.42.2631.

[37] Jaroslav Adam et al. *Centrality dependence of the charged-particle multiplicity density at midrapidity in Pb-Pb collisions at* $\sqrt{s_{NN}} = 5.02$ *TeV*. Phys. Rev. Lett., 116(22):222302, 2016. doi: 10.1103/PhysRevLett.116.222302.

[38] Thomas Mc Cauley. *Collision events recorded by CMS in 2016*. CMS Collection., Jan 2017. URL https://cds.cern.ch/record/2241144.

[39] T. Isenberg. *Abstraction in scientific data visualization: application to brain connectivity and structural biology*, 2017. URL https://indico.cern.ch/event/577003/contributions/2476445/. Connecting The Dots / Intelligent Trackers.

[40] M. H. Everts, H. Bekker, J. B. T. M. Roerdink, and T. Isenberg. *Depth-Dependent Halos: Illustrative Rendering of Dense Line Data*. IEEE Transactions on Visualization and Computer Graphics, 15(6):1299–1306, Nov 2009. ISSN 2160-9306. doi: 10.1109/TVCG.2009.138.

[41] Lindsey Gray. *First Steps Towards Four-Dimensional Tracking: Timing Layers at the HL-LHC*. Connecting The Dots, 2018. URL https://indico.cern.ch/event/658267/contributions/2870293/.

[42] Corentin Allaire. *A High-Granularity Timing Detector in ATLAS: Performance at the HL-LHC*. Nucl. Instrum. Meth., A924:355–359, 2019. doi: 10.1016/j.nima.2018.05.028.

[43] Anna Zaborowska. *Calorimetry for the Future Circular Collider experiments*, Nov 2017. URL http://cds.cern.ch/record/2622168. Presented 2018.

[44] A Salzburger and D Kuhn. *A Parametrization for Fast Simulation of Muon Tracks in the ATLAS Inner Detector and Muon System*, 2003. URL http://cds.cern.ch/record/813003. Presented on 14 Jun 2003.

[45] Gerhard Lutz. *Semiconductor radiation detectors: device physics*. Springer, Berlin, 1999. URL http://cds.cern.ch/record/411172.

[46] Werner Riegler and Gianluca Aglieri Rinella. *Time resolution of silicon pixel sensors*. JINST, 12(11):P11017, 2017. doi: 10.1088/1748-0221/12/11/P11017.

[47] Hartmut F.-W. Sadrozinski, Abraham Seiden, and Nicolò Cartiglia. *4-Dimensional Tracking with Ultra-Fast Silicon Detectors*. Reports on Progress in Physics, (AIDA-2020-PUB-2017-010), Apr 2017. URL http://cds.cern.ch/record/2667268.

[48] E. Currás et al. *Inverse Low Gain Avalanche Detectors (iLGADs) for precise tracking and timing applications*. In *15th Vienna Conference on Instrumentation (VCI2019) Vienna, Austria, February 18-22, 2019*, 2019.

[49] V. Sola. *Low-Gain Avalanche Diodes for Precision Timing in the CMS Endcap*. May 2018. URL http://cds.cern.ch/record/2667257.

[50] Stefan Guindon. *ATLAS: High Granularity Timing Detector, Focus on sensor performance*. Mar 2019. URL http://cds.cern.ch/record/2665790.

[51] R. Fruhwirth and R. K. Bock. *Data analysis techniques for high-energy physics experiments*. Camb. Monogr. Part. Phys. Nucl. Phys. Cosmol., 11:1–434, 2000.

[52] Betty Bezverkhny Abelev et al. *Performance of the ALICE Experiment at the CERN LHC*. Int. J. Mod. Phys. A, 29(CERN-PH-EP-2014-031. CERN-PH-EP-2014-031):1430044. 120 p, Feb 2014. URL http://cds.cern.ch/record/1648854. Comments: 109 pages, 88 captioned figures, 12 tables, authors from page 104, published version, figures at this http URL http://aliceinfo.cern.ch/ArtSubmission/node/716.

[53] Walter Blum, Werner Riegler, and Luigi Rolandi. *Particle detection with drift chambers; 2nd ed.* Springer, Berlin, 2008. URL http://cds.cern.ch/record/1105920.

[54] Michael Benedikt and others (FCC Collaboration). *Comprehensive Design Report: Tracker Chapter.* in preparation, 9 2019.

[55] Zbynek Drasal and Werner Riegler. *An extension of the Gluckstern formulae for multiple scattering: Analytic expressions for track parameter resolution using optimum weights.* Nucl. Instrum. Meth., A910:127–132, 2018. doi: 10.1016/j.nima.2018.08.078.

[56] R. L. Gluckstern. *Uncertainties in track momentum and direction, due to multiple scattering and measurement errors.* Nucl. Instrum. Meth., 24:381–389, 1963. doi: 10.1016/0029-554X(63)90347-1.

[57] Giovanni Bianchi. *tkLayout: a Design Tool for Innovative Silicon Tracking Detectors.* Technical Report CMS-CR-2013-438, CERN, Geneva, Nov 2013. URL http://cds.cern.ch/record/1640926.

[58] Z. Drasal et al. *Official FCC-hh tracker layout repository: Tracker in flat configuration - v3.03*, 2017. URL http://fcc-tklayout.web.cern.ch/fcc-tklayout/FCChh_v3.03/index.html.

[59] D. Dannheim et al. *Detector Technologies for CLIC.* CERN Yellow Reports: Monographs. May 2019. doi: 10.23731/CYRM-2019-001. URL http://cds.cern.ch/record/2673779.

[60] Julia Hrdinka. *The FCC pp, ep and ee tracking detector concepts and their projected performance.* Connecting The Dots, 2019. URL https://indico.cern.ch/event/742793/contributions/3295120/.

[61] Julia Hrdinka. *Tracker performance studies at the 100 TeV future circular hadron collider at extreme pile-up conditions*, 2019. URL http://cds.cern.ch/record/2690632. Presented 20 Sep 2019.

[62] Jamie Shiers, Frank Olaf Berghaus, Jakob Blomer, Gerardo Ganis, Sunje Dallmeier-Tiessen, Tibor Simko, and German Cancio Melia. *CERN Services for Long Term Data Preservation.* Technical Report CERN-IT-Note-2016-004, CERN, Geneva, Jul 2016. URL http://cds.cern.ch/record/2195937.

[63] Patrick Janot and Stanisław Jadach. *Improved Bhabha cross section at LEP and the number of light neutrino species.* Physics Letters B, 803:135319, Apr 2020. ISSN 0370-2693. doi: 10.1016/j.physletb.2020.135319. URL http://dx.doi.org/10.1016/j.physletb.2020.135319.

[64] Michal Svatos, Jiri Chudoba, and Petrri Vokac. *ATLAS utilisation of the Czech national HPC center.* EPJ Web Conf., 214:03005, 2019. doi: 10.1051/epjconf/201921403005.

[65] Stefan Roiser, Ana Gaspar, Yves Perrin, and Karol Kruzelecki. *Servicing HEP experiments with a complete set of ready integrated and configured common software components.* J. Phys. Conf. Ser., 219:042022, 2010. doi: 10.1088/1742-6596/219/4/042022.

[66] Jakob Blomer, Carlos Aguado Sanchez, Predrag Buncic, and Artem Harutyunyan. *Distributing LHC application software and conditions databases using the CernVM file system.* J. Phys. Conf. Ser., 331:042003, 2011. doi: 10.1088/1742-6596/331/4/042003.

[67] G. Barrand et al. *GAUDI - A software architecture and framework for building HEP data processing applications.* Comput. Phys. Commun., 140:45–55, 2001. doi: 10.1016/S0010-4655(01)00254-5.

[68] M. Clemencic, B. Hegner, and C. Leggett. *Gaudi evolution for future challenges.* J. Phys. Conf. Ser., 898(4):042044, 2017. doi: 10.1088/1742-6596/898/4/042044.

[69] F. Gaede, B. Hegner, and P. Mato. *PODIO: An Event-Data-Model Toolkit for High Energy Physics Experiments.* J. Phys. Conf. Ser., 898(7):072039, 2017. doi: 10.1088/1742-6596/898/7/072039.

[70] Torbjorn Sjostrand, Stefan Ask, Jesper R. Christiansen, Richard Corke, Nishita Desai, Philip Ilten, Stephen Mrenna, Stefan Prestel, Christine O. Rasmussen, and Peter Z. Skands. *An Introduction to PYTHIA 8.2*. Comput. Phys. Commun., 191:159–177, 2015. doi: 10.1016/j.cpc.2015.01.024.

[71] Matt Dobbs and Jorgen Beck Hansen. *The HepMC C++ Monte Carlo event record for High Energy Physics*. Comput. Phys. Commun., 134:41–46, 2001. doi: 10.1016/S0010-4655(00)00189-2.

[72] Michele Selvaggi. *DELPHES 3: A modular framework for fast-simulation of generic collider experiments*. J. Phys. Conf. Ser., 523:012033, 2014. doi: 10.1088/1742-6596/523/1/012033.

[73] A Zaborowska. *Geant4 fast and full simulation for Future Circular Collider studies*. J. Phys. : Conf. Ser., 898(4):042053. 8 p, 2017. URL https://cds.cern.ch/record/2298621.

[74] Markus Frank, F. Gaede, C. Grefe, and P. Mato. *DD4hep: A Detector Description Toolkit for High Energy Physics Experiments*. J. Phys. Conf. Ser., 513: 022010, 2014. doi: 10.1088/1742-6596/513/2/022010.

[75] Marko Petrič, Markus Frank, Frank Gaede, and André Sailer. *New developments in DD4hep*. EPJ Web Conf., 214:02037, 2019. doi: 10.1051/epjconf/201921402037.

[76] Colin Bernet. *Heppy: A lightweight event processing framework for high energy physics written in python*. Technical Report 1st DAWG Technology and Innovation Survey, CERN, Geneva, Feb 2019. URL https://indico.cern.ch/event/789007/contributions/3317130.

[77] Enrico Guiraud. *RDataFrame: easy parallel ROOT analysis at 100 threads*. Technical Report CHEP 2018, CERN, Geneva, Aug 2018. URL https://indico.cern.ch/event/587955/contributions/2937534.

[78] P Schade and A Lucaci-Timoce. *Description of the signal and background event*

mixing as implemented in the Marlin processor OverlayTiming. Jul 2011. URL http://cds.cern.ch/record/1443537.

[79] Zachary Marshall. *Simulation of Pile-up in the ATLAS Experiment*. J. Phys. Conf. Ser., 513:022024, 2014. doi: 10.1088/1742-6596/513/2/022024.

[80] Christian Gumpert, Andreas Salzburger, Moritz Kiehn, Julia Hrdinka, and Noemi Calace. *ACTS: from ATLAS software towards a common track reconstruction software*. Technical Report ATL-SOFT-PROC-2017-030. 4, CERN, Geneva, 01 2017. URL https://cds.cern.ch/record/2243297.

[81] G. Bianchi. *tkLayout: a design tool for innovative silicon tracking detectors*. JINST, 9:C03054, 2014. doi: 10.1088/1748-0221/9/03/C03054.

[82] Valentin Volkl. *TrickTrack: An experiment-independent, cellular-automaton based track seeding library*. in preparation, 9 2018.

[83] Felice Pantaleo, Alexander Schmidt, Vincenzo Innocente, Benedikt Hegner, Andreas Pfeiffer, and Andreas Meyer. *New Track Seeding Techniques for the CMS Experiment*. 2017. URL http://cds.cern.ch/record/2293435.

[84] R Frühwirth and A Strandlie. *A new Riemann fit for circular tracks*. Journal of Physics: Conference Series, 762(1):012032, 2016. URL http://stacks.iop.org/1742-6596/762/i=1/a=012032.

[85] S. Agostinelli and others (Geant4 collaboration). *Geant4 - a simulation toolkit*. Nuclear Instruments and Methods in Physics Research Section A: Accelerators, Spectrometers, Detectors and Associated Equipment, 506(3):250 – 303, 2003. ISSN 0168-9002. doi: https://doi.org/10.1016/S0168-9002(03)01368-8. URL http://www.sciencedirect.com/science/article/pii/S0168900203013688.

[86] Koji Terashi, Ryu Sawada, Masahiko Saito, and Shoji Asai. *Search for WIMPs with disappearing track signatures at the FCC-hh*. Technical Report CERN-ACC-2018-0044, CERN, Geneva, Oct 2018. URL https://cds.cern.ch/record/2642474.

[87] Z. Drasal et al. *Official FCC-hh tracker layout repository: Tracker in tilted configuration - v4.01*, 2017. URL http://fcc-tklayout.web.cern.ch/fcc-tklayout/FCChh_v4.01/index.html.

[88] G. Bianchi et al. *tkLayout-lite SW: Github repository of a tkLayout version adapted for FCC-hh needs*. URL https://github.com/tkLayout/tkLayout/tree/masterLite.

Acknowledgements

First and foremost, I want to thank my supervisors Emmerich Kneringer and Benedikt Hegner, who made this work possible in the first place. My closest colleagues Anna and Joschka and the complete SFT group always ensured that the work was not only interesting, but a pleasure as well.

The climbing adventures with Oliver (the inofficial president of the CERN climbing club), Brant, Rebecca, Megan, Irene, Luca, Liz, Elena, Katharina and the rest of the inofficial CERN climbing club have given me a much needed respite from work. Despite the brief time I knew her, Masha has truly recalibrated my perspective on life, work, death and climbing, and I will keep her in memory for that.

When asked where is the best place to search for new physics, La Praille, home to Geneve Velo Polo is probably a close second for me – at least the feats the players there perform still seem impossible to me. Many thanks to all of GVP for their community, humour and dedication to this absurd but fantastic sport.

Thanks Gabi, for all the hugs.

Finally thanks to my family for everything.

Eidesstattliche Erklärung

Ich erkläre hiermit an Eides statt durch meine eigenhändige Unterschrift, dass ich die vorliegende Arbeit selbständig verfasst und keine anderen als die angegebenen Quellen und Hilfsmittel verwendet habe. Alle Stellen, die wörtlich oder inhaltlich den angegebenen Quellen entnommen wurden, sind als solche kenntlich gemacht. Die vorliegende Arbeit wurde bisher in gleicher oder ähnlicher Form noch nicht als Magister-/Master-/Diplomarbeit/Dissertation eingereicht.

Datum	Unterschrift